High pressure CO_2 reactivity of Highveld coal from various mines

DP Bothma

cid.org/ 0000-0000-0002-2463-1750

Dissertation accepted in fulfilment of the requirements for the degree *Master of Engineering in Chemical Engineering* at the North-West University

Supervisor:	Prof HWJP Neomagus
Co-supervisor:	Prof JR Bunt
Assistant-supervisor:	Prof RLJ Coetzer

Graduation: June 2025

Acknowledgements

The following individuals, laboratories and institutions are acknowledged for their contribution, during this study; special appreciation and words of gratitude go to the following:

- Sasol for funding this project
- Prof Hein Neomagus and Prof John Bunt for providing their wisdom and guidance throughout this project.
- Prof Roelof Coetzer for his guidance in the statistical analysis.
- Clement Mgano for his assistance throughout the experimental studies conducted as well as his assistance with equipment troubleshooting.
- Dr Gregory Okolo for conducting the surface area analysis.
- Bureau Veritas Testing and Inspections laboratory for conducting the conventional characterization and XRF analysis.
- Prof Nicola Wagner at the University of Johannesburg for conducting the microlithotype, maceral and char form analysis.

The work presented in this study is based on research supported by the South African Research Chairs Initiative of the Department of Science and Innovation and National Research Foundation of South Africa (Coal Research Chair Grant No. 86880). Any opinion, finding, or conclusion or recommendation expressed in this material is that of the author(s) and the NRF does not accept any liability in this regard.

Executive summary

Coal gasification is a process that converts coal into a clean-burning synthesis gas (syngas), which can be used for various applications, including electricity generation, chemical production, and as a feedstock for the production of liquid fuels like synthetic natural gas or transportation fuels. Coal gasification, which is the initial stage of the coal to liquid (CTL) process, is carried out at high pressure in a fixed-bed dry bottom (FBDB) gasifier. While there has been a lot of research in the past about the gasification reactivity of Highveld coal chars, little is known about the correlation between coal properties and intrinsic coal reactivities. However, the relationship between coal characteristics and intrinsic coal reactivities remains a relatively unexplored area of study.

The aim of this study is to correlate the intrinsic coal reactivity of seven different single source coal samples to their respective coal and coal char characteristics. The coal samples used in this study were sourced from various seams within the Highveld coalfield. The coal chars were produced by undergoing mechanical size reduction to a particle size range of -150 to +75 µm. Subsequently, the chars were subjected to charring conditions of 900 °C and 30 bar pressure in an environment consisting of nitrogen gas (N_2). The specific reaction rates were significantly higher with the use of pure CO_2 compared to other studies where lower concentrations of CO_2 was used. Because of the higher specific reaction rates, the gasification experiments were conducted at a temperature range of 730 to 750 °C.

From the correlations of intrinsic coal reactivity of the seven different single source coal samples and their respective coal characteristics it was observed that the best model for prediction is reactivity as a function of the temperature and ultimate analysis of the coal, which has the highest R^2 value and smallest standard error of the model. The chemical and mineralogical properties were considered in the correlations, which included proximate and ultimate analysis, ash composition, gross calorific values, alkali index, Si/Al ratio, CaO content, internal surface area of the coal chars, petrographic and char morphology.

A correlation between intrinsic coal properties and coal reactivity revealed that the regression model of reactivity as a function of temperature and proximate analysis can be used to accurately predict gasification reactivities of Highveld coal samples. It is however pertinent that the predictions of other coal samples are compared to the measured values to determine the

repeatability of the correlation results when investigating coal samples from different geographical locations.

Keywords: High pressure CO_2 gasification reactivity, intrinsic reaction rates, Highveld coal char, coal characteristics.

Table of contents

List of tables

List of figures

Nomenclature

Table 1: List of symbols

Symbol	Description	Units
C (CO)	Carbon-CO surface complex	-
C (O)	Carbon-oxygen surface complex	-
C (H)	Carbon-hydrogen surface complex	-
C_f	Free carbon sites	*1/g*
$[C_t]$	Total number of sites	*1/g*
$[C_t]k_i$	LH rate type parameter	*1/bar.s*
c	Intrinsic $[C_t]k_i$ term	$g/m^2.s.bar$
E_a	Apparent activation energy	*kJ/mol*
E	Activation energy	*kJ/mol*
K_0	Pre-exponential factor	$g.bar^n/g/s$
k_i	Rate constant	*1/s*
k_p	RPM rate constant	*1/s*
k_s	Specific rate constant	*1/s*
L_0	Pore length per unit volume	m/m^3
m	Reaction order	*g*
$m_{c,0}$	Initial mass of carbon	*g*
$m_{c,t}$	Instantaneous mass of carbon	*g*
$m_{char,0}$	Initial mass of coal char	*g*
m_t	Instantaneous mass of coal char	*g*
MW_c	Molecular weight of carbon	*g/mol*
n	Apparent reaction order	-
n_i	Moles of species i	*mol*
$\dot{n}$	Molar flow rate	*Mol/s*
$\dot{n}_T$	Total molar flow rate	*mol/s*
p_i	Partial pressure of species i	*bar*
P_{STP}	Standard pressure	*bar*
R	Universal gas constant	*J/mol.K*
r_s	Specific reaction rate	*g/g/s*
$r_{s,0}$	Initial specific reaction rate	*g/g/s*

S	Surface area	m^2/g
S_0	Initial surface area	m^2/g
S_m	Micropore surface area	m^2/g
T	Temperature	*K or °C*
T_a	Actual/ observed temperature	*K or °C*
T_{STP}	Standard temperature	*K or °C*
t	time	*s or min*
$\dot{V}_a$	Actial/ observed flow rate	*L/min*
$\dot{V}_{STP}$	Flow rate at standard conditions	*NL/min*
X	Char or carbon conversion	-
X_c	Carbon conversion	-
x_i	Mass fraction of species i	-
y_i	Mole fraction of species i	-

Greek symbols

ψ	Structural parameter	-
ε_0	Initial porosity	-

Table 2: List of abbreviations

Abbreviation	Definition
adb	Air-dried basis
AFT	Ash fusion temperature
BET	Brunauer-Emmet-Teller
CTL	Coal-to-Liquid
D-A	Dubinin-Astakhov
daf	Dry-ash free basis
db	Dry basis
EPC	Electronic pressure controller
HPFBR	High pressure fixed-bed reactor
ISO	International standards organisation
LH	Langmuir-Hinshelwood
MFC	Mass flow controller
mmf	Mineral matter-free
MW	Molecular weight
PSD	Particle size distribution
RPM	Random-Pore Model
SANS	South African National Standard
STP	Standard temperature and pressure
TGA	Thermo-gravimetric analyser
XRF	X-ray fluorescence
wt %	Weight percentage

Chapter 1: Introduction

1.1 Background and motivation

1.1.1 Significance of coal

As the global energy consumption rises, a greater emphasis has been placed on alternative fuel sources [1]. However, the demand for coal is still significantly high, specifically in developing countries [2]. Coal is not only cheaper than most alternatives, but it is also readily available in certain developing countries. Currently, around 7,700 metric tons of coal is used annually worldwide by a variety of sectors [2]. Coal is utilised on a global scale for power generation as well as industries such as iron and steel manufacture, and cement manufacturing, among others [2]. Figure 1 provides an overview of the coal recoverable resources under the current technological and economic conditions [3]. The provided figure illustrates the coal recoverable resources in various countries, measured in million tons of oil equivalent.

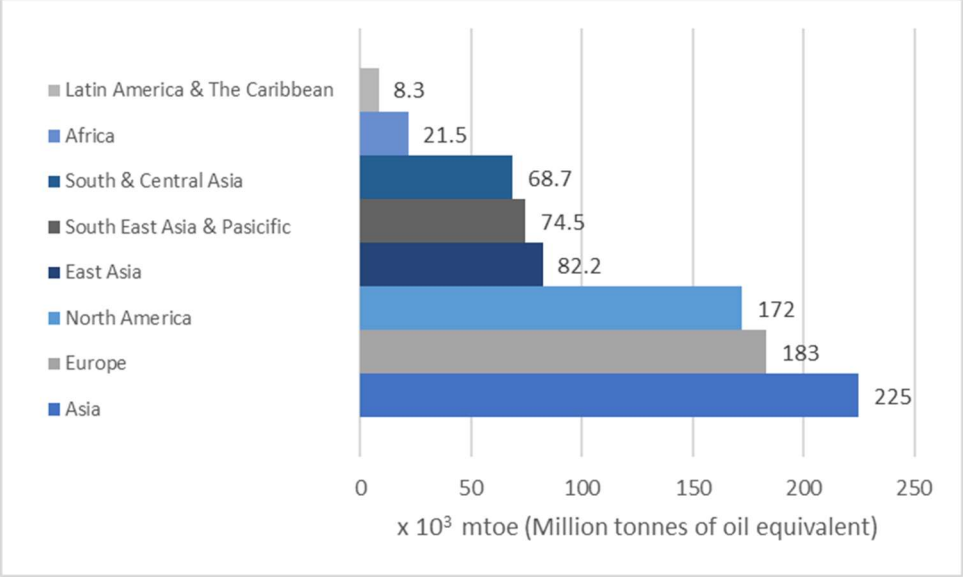

Figure 1: Coal recoverable resources by region [2]

Asia is the largest consumer of coal worldwide, constituting around 66 % of the global coal consumption [4]. Following a period of consecutive decreases, there was a notable increase in coal consumption by 1 %, equivalent to 25 million tonnes of oil (mtoe) from 2013 to 2017 [4]. Notably, India showed the highest growth rate, with a 4.8 % increase amounting to 18 mtoe in 2017 [4]. China had a notable upturn in coal consumption (0.5 %, 4 mtoe) following three

consecutive years of decrease, despite significant transitions from coal to gas in both industrial and residential sectors [4]. This increase in coal usage can be attributed to the growing power demand in these countries, which necessitated the utilisation of additional coal as a supplementary fuel for balancing purposes [5]. Developing countries like South Africa, China, and India rely heavily on coal for energy generation [1], [6]. These countries still experience significant economic growth through the utilization and export of fossil fuels [7]. Table 3 gives the top ten coal producing countries in the world [8].

Table 3: Top coal producing countries [8]

Number	Country	Coal Produced (million tons)
1	China	3874
2	United States	906.0
3	Australia	644.0
4	India	537.6
5	Indonesia	461.0
6	Russia	357.6
7	South Africa	260.5
8	Germany	185.8
9	Poland	137.1
10	Kazakhstan	108.7

Table 4 presents a list of the top ten countries globally in terms of coal exports, measured in million tons [9]. Australia stands at the forefront of this list, exporting a staggering amount of coal in 2014, closely trailed by Indonesia [9]. Russia follows at a considerable distance, exporting 239.1 million tons less than Australia, followed by the United States [9].

Colombia and South Africa nearly tie in their export quantities, both around double the exports reported by Canada [9]. Canada and Kazakhstan exhibit moderate exports in 2013 [9]. Mongolia and Korea complete the top ten, with half the exports reported by Canada, showcasing their participation in the global coal export market [9]. These figures underscore the dominance of Indonesia and Australia in coal exports, while also highlighting the significant contributions of other nations in this industry [8].

Table 4: Top coal exporting countries (2013) [9]

Number	Country	Coal Exported (million tons)
1	Australia	394.7
2	Indonesia	389.6
3	Russia	155.6
4	United States	122.7
5	Columbia	82.40
6	South Africa	82.20
7	Canada	40.40
8	Kazakhstan	36.00
9	Mongolia	19.30
10	Korea	18.40

South Africa is among the top ten countries listed in both Table 3 and Table 4. In South Africa, coal mining is an important economic contributor, historically fuelling electricity generation, job creation, and export revenue. In a study conducted by Worship [10], it was found that electricity generated from coal boosts economic growth in the short and long run. As of 2015, South Africa was mining an estimated 182 million tons of marketable coal in 2022 [11]. The country will remain dependent on coal for electricity generation and chemical production for the foreseeable future due to the large supply available and the lack of other natural reserves, like oil and gas [12].

However, coal's use has environmental repercussions, prompting the country to explore cleaner energy alternatives [10]. Coal is the most carbon-intensive fossil fuel and coal-fired power plants produce 75% of global CO_2 emissions [13]. Clean coal technologies have gained renewed interest, primarily due to the climate-altering effects of the increase in atmospheric CO_2 [14]. After a decade of relative silence surrounding coal gasification, which began around the year 2000, four broad trends have rekindled interest in the technology [15]:

- Substitution of crude oil with other energy carriers, such as biomass or coal, with the objective of ensuring supply security and stabilizing local energy prices (e.g., China).
- Increasing interest in the utilization of low-grade coals with high ash or moisture content in developing countries (e.g., India, Indonesia). Japan [16], India [17], South Africa [18],

and even China [19] have all reported using coal with a high mineral content. If a coal has an ash yield of 20 wt% or more, it is referred to as "high ash" coal [20].

- Stabilization potential of polygeneration plants for high fluctuations in electricity generation caused by the rising proportion of renewable energy sources (e.g., in Europe).

With rising CO_2 emissions posing a problem in light of the global awareness, the need to transition to renewable energy has become of urgent concern [7]. South Africa among others, must discover means of minimizing environmental pollution in order to achieve sustainable growth [7]. Oladipupo *et al*. [7] used historical data from 1970 to 2018 to determine a dependency structure between globalization, CO_2 emissions, and the use of renewable energy as opposed to non-renewable energy [7]. This study examined the effects of South Africa's energy consumption, economic growth, and globalization on its CO_2 emissions.

Renewable energy sources are insufficient to meet environmental and energy demands [21], [7], establishing coal's importance in the near future [22]. According to the data reported by Ritchie *et al.* [23], coal and gas consumption showed the biggest increases throughout the years, peaking around 2018. These findings emphasize a critical challenge faced by South Africa and similar nations. While renewable energy is advocated as a solution to mitigate CO_2 emissions [24], [25], [26], the current infrastructure and capacity fall short of meeting the escalating energy demands [10]. The reliance on coal and gas remains prominent, reflecting the need for a comprehensive strategy to balance immediate energy needs with the imperative to transition to sustainable alternatives [8]. Therefore, South Africa is faced with a critical dilemma in mitigating emissions while guaranteeing reliable energy supply, which calls for inventive strategies and substantial investments in both renewable energy and fossil fuel advancement [27].

1.1.2 Coal to liquid technology (CTL)

South Africa has produced coal-derived fuels since 1955, and coal gasification will continue to play a vital role in the South African CTL process [28]. Coal gasification is the first and most crucial step in coal-to-liquid technology when indirect coal liquefaction (ICL) is used. Coal and a mixture of oxygen and steam, are fed into fixed-bed gasifier reactors operating at high pressures to produce synthesis gas [15], [29], [30]. There are several sub-processes occurring during coal gasification, including drying, devolatilization, partial oxidation, and gasification [15], [31]. The char gasification reaction has a substantial effect on the coal conversion and gasification unit size [15], [29], [32]. This is a result of the slow, heterogeneous chemical reactions that occur during

the gasification of coal char in conjunction with co-fed steam [15], [33]. Numerous studies on the kinetics and thermodynamics of the accompanying reactions have focused on the rate-limiting step (coal char gasification), which controls the overall gasification process [15], [31].

In 2017, approximately 23 % of the nation's coal was utilized in Coal-to-Liquid (CTL) technology to produce a variety of resources, including but not limited to liquid fuels, solvents, and acids [27], [34]. A significant portion of the country's demand is met by liquid fuels produced from coal via gasification [34]. South Africa met roughly 3.2 % of its fuel needs with gas (GTL), 54.4 % with crude oil, and 42.3 % with coal (CTL) [35]. The CTL sector developed significantly due to the high fuel demand from the transportation sector. The petrochemical industry is responsible for 23% of South Africa's coal consumption and daily production of 150,000 barrels of fuel and petrochemicals (2007) [27].

1.1.3 Coal char gasification kinetics

The thermodynamic and kinetic behaviour of char gasification play a large role in optimizing and understanding the gasification process. Kinetic studies are constantly used to improve the gasification process through laboratory experiments using CO_2 as a reference for fundamental studies [36]. The coal char gasification kinetics and the extent of conversions obtained at a laboratory scale provide kinetic data allowing for the prediction of coal char behaviour during gasification through modelling attempts. The gasification rate is dependent on the reaction conditions, chemical properties, and physical char structure [37]. Numerous studies have been conducted with and without inhibitors to determine coal char gasification kinetics using steam, CO_2, or mixtures of the two [12], [38], [39]. Significant changes in the char structure and reactivity of single-source coals have been observed in literature [40], [41].

Research into the reactivity of single-source coals is therefore important in understanding whether the differences observed are intrinsic (within the carbon matrix) to the coal or not. Several studies have investigated single-source CO_2 coal gasification kinetics and modelling at high temperatures and low pressures [12], [40], [42]. Although the kinetic studies at low pressures and high temperatures have significantly contributed to gasification modelling, there is a need for gasification studies at high pressures [15], [12], [43], [44]. By investigating the coal char reactivity of various South African coals and examining their relationship with coal and char characteristics at elevated temperatures and pressures, valuable insights can be gained.

1.2 Problem statement

Numerous studies have been conducted on coal char gasification at low and high pressures, using steam, CO_2, and mixtures of the two, with the intent of quantifying the gasification reaction kinetics [18], [45], [46], [47], [48], [49]. With the current pressure targeted on the coal industry, a lot of focus has been placed on optimizing and understanding the properties of coal and coal char [7]. The CO_2 and steam gasification studies contributed significantly to the knowledge and understanding of gasification kinetics and the use of kinetic models [43], [50], but there is however limited information on the use of models to estimate reaction rates with the use of coal/char properties.

With the limited number of studies that has been focused on some form of correlation for South African coals, conducting research in this particular domain can yield substantial insights that facilitate enhanced optimisation and precise modelling of the coal char gasification process. Additionally, it enables the prediction of gasification reactivity of a coal char samples by using its inherent characteristics.

1.3 Research aim and objectives

This study will focus on coal reactivity, coal char characterization, and the resultant char morphology of single source coals at elevated temperatures and pressures in a pure CO_2 atmosphere. The coal reactivity and kinetics are influenced by the regime under which the gasification reactions take place [12], [43], [51]. [52]The chemically controlled regime has been chosen for this study to allow for the focus to be placed on the intrinsic reactivity of the coal samples (excluding mass transfer limitations) [37].

The coal and coal char properties will be used to generate regression models. The regression models are used to determine the correlation between these properties and intrinsic coal reactivity. The objective of the statistical regression analysis is to quantify the difference in reactivity between the different coal sources, and the relationship between reactivity, temperature and coal/ char properties.

In order to achieve this aim, the following objectives are set:

- Source and characterize 7 single source parent coals

- Perform high pressure devolatilization of these coals and characterize the obtained coal chars
- Determine high-pressure gasification reactivity in the chemical controlled regime.
- Statistical correlation of char reactivity with coal and coal char properties.

1.4 Research methodology and scope

The scope of this investigation is to conduct coal char gasification experiments using a laboratory scale high pressure fixed-bed reactor (HPFBR). This allows for the analysis of the main carbon-containing gasification product (CO) in order to determine the char reactivity. For obtaining the objectives listed in Section 1.3, the scope is subdivided into the following sections:

1.4.1 Coal preparation

The seven coarse Highveld coal samples obtained for this study will go through several crushing and sieving steps to achieve a desired particle size distribution (PSD) of -150 +75 µm. This PSD will be achieved through the use of a hammer mill, jaw crusher, ball mill and sieves. The coal samples have to be prepared for pyrolysis and coal characterization analysis. After pyrolysis, the coal char samples are prepared for gasification and char characterization analysis.

1.4.2 Coal charring

The seven Highveld coal samples obtained for this study are charred in a high-pressure tube furnace in an inert environment. The pyrolysis process will ensure that most of the volatiles and moisture content are released from the samples. The operating pressure is determined based on industrial operating conditions.

1.4.3 Coal and char characterization

Several analyses are conducted on the coal samples: proximate and ultimate analysis, calorific value, porosity, ash elemental composition analysis, petrography analysis, and char morphology analysis. The relevant coal/char analysis is selected in order to better correlate reactivity with coal/ char properties.

1.4.4 CO_2 char gasification

The gasification experiments are conducted in a high pressure fixed-bed reactor at temperatures ranging from 730, 740 and 750 °C as well as a pressure of 30 bar. The experiments are conducted in a chemically controlled regime, and this will be determined beforehand for each of the coal char samples as explained in Appendix A: Evaluation of operating regime. In this study, the experiments are conducted at a constant CO_2 pressure and three different temperatures to measure the reactivities at around 8 % conversion.

1.4.5 Correlate char reactivity with coal properties

After the reactivities of the seven coal chars have been determined and the analysis has been completed, the intrinsic reactivities of the coal chars are then correlated with the coal and char properties. A statistical model has been constructed for coal reactivity as a function of temperature, coal and coal char properties of the different sources. This model has been used to quantify the difference in reactivity between the samples using the data obtained from the previous sections. Tukey Honest Significant Differences (HSD) tests have also be conducted to assess the difference in reactivity between the sources at a set temperature.

Chapter 2: Literature Review

Introduction

In this chapter, literature on coal char gasification will be discussed as well as the results obtained in previous studies reviewed. The structure and main headings of the literature review is shown in Figure 2. Coal gasification is a complex process, consisting of coal pyrolysis and char gasification [53]. The literature review is subdivided into three categories, namely coal char gasification, factors affecting char reactivity and char structural development during gasification.

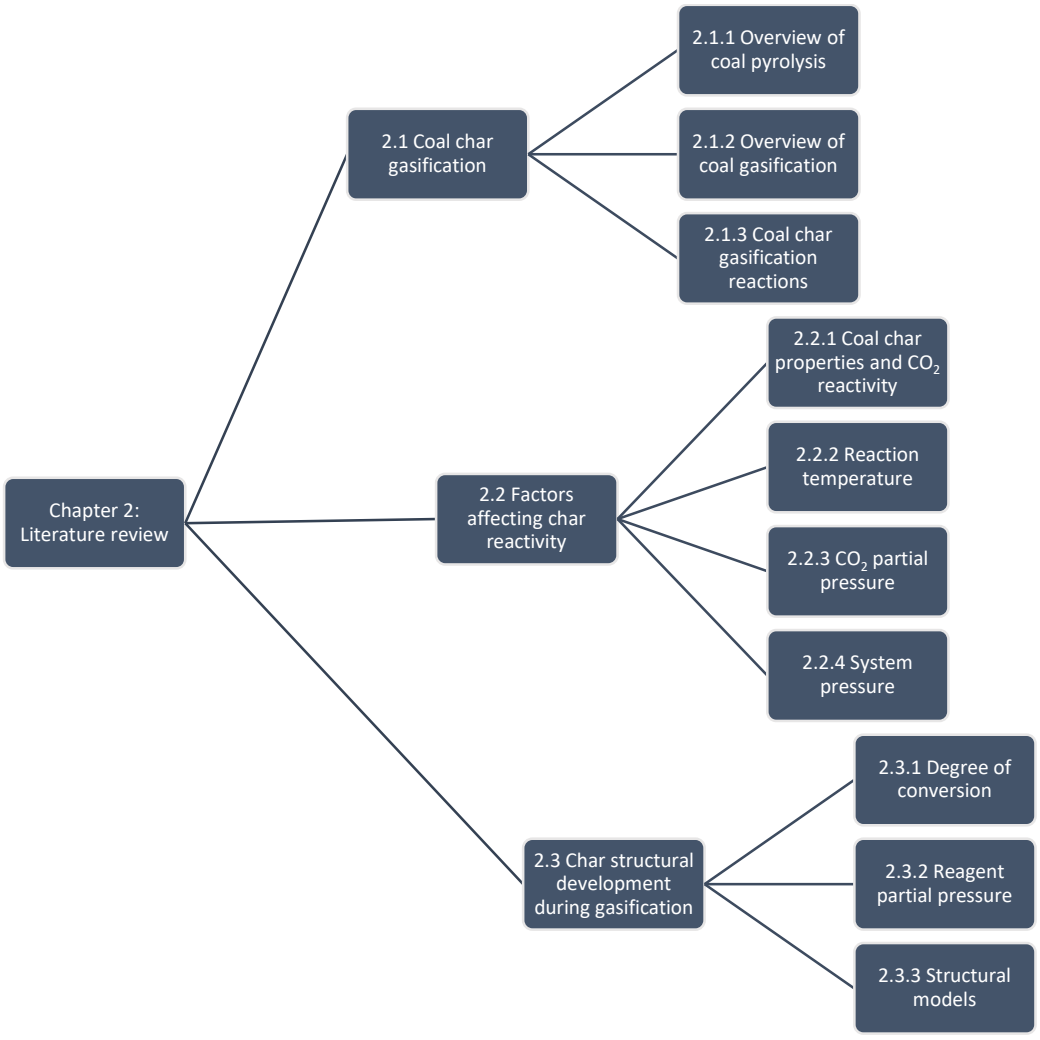

Figure 2: Introduction to literature review

Section 2.1 will contain literature on the coal pyrolysis process, followed by literature on the coal gasification process. Section 2.1.3 contains a more in-depth discussion of the coal char gasification reactions. Section 2.2 contains further information on the factors affecting the gasification reactions. This includes, but is not limited to, coal char properties, temperature, partial pressure, and system pressure. The structural development of the char particles during gasification is discussed in Section 2.3, with a specific focus on the degree of conversion, reagent partial pressures, and structural models.

2.1 Coal char gasification

The coal pyrolysis process will be discussed in Section 2.1.1 as well as the reaction steps taking place. Section 2.1.2 will expand on the coal gasification process followed by the coal char gasification reactions in Section 2.1.3.

2.1.1 Overview of coal pyrolysis

Pyrolysis is the initial reaction step for coal combustion, gasification, and hydrogenation [54]. Coal pyrolysis cannot be classified as a single step reaction due to the changing extent of the reaction, followed by a change in activation energy [54]. Char particles are formed when volatiles are released during the pyrolysis process. The mineral content, coal rank, temperature, and particle size can influence the type of char formed [43], [50], [53], [55].

Coal pyrolysis is a complex process involving the thermal decomposition of coal in the absence of oxygen. Coal consists of complex organic structures with aromatic ring systems interconnected by various types of chemical bonds, often referred to as "bridges". Upon heating, cracking of the bridges between ring systems take place, forming smaller fragments and radical groups (atoms or molecules with unpaired electrons, making them highly reactive).

The radicals formed in the first step react with available hydrogen. This reaction leads to the formation of small molecules such as methane (CH_4), other aliphatic hydrocarbons (straight or branched chain hydrocarbons), and water (H_2O). These small molecules diffuse out of the coal particles into the surrounding environment. Larger radical molecules that form during pyrolysis also undergo reactions with hydrogen. This leads to the formation of tar, which consists of medium molecular weight compounds [56]. The tar products then diffuse out of the coal particles. Some of the larger molecules undergo further reactions, condensing to form coke, a carbon-rich solid

material [57]. During this condensation process, hydrogen is eliminated from the molecules. The hydrogen released is expelled as gas from the coal particles [57].

The intrinsic rate parameters reported in the literature are often based on chars generated at atmospheric pressure [40], [58], and low heating rates [59], [60]. These conditions are not representative of commercial gasifier conditions. Most of these studies have been conducted on coal pyrolysis, focusing mainly on the coal rank or element composition. The studies that considered the effects of macerals on the pyrolysis process had inconclusive results, mainly due to the relatively low purity of macerals and the difficulty experienced when quantifying the interactions between different macerals [18], [61]. The catalytic effect of the minerals within the macerals needs to be considered due to the catalytic effect of mineral matter and macerals [55].

The pyrolysis temperature of coal depends on coal rank, mainly due to the various functional groups within the coal [54]. The chemical and physical properties, such as functional groups and pore structure, of the pyrolyzed coal will change at different temperatures [62]. During pyrolysis reactions, several changes in parameters such as aromaticity and density of aliphatic groups take place, including chemical reactions such as bond breaking and cross-linking [62].

These changes in parameters and chemical reactions result in the formation of different products during pyrolysis. The temperature at which pyrolysis occurs also affects the yield and composition of these products [62]. Higher temperatures typically lead to higher yields of gaseous products, while lower temperatures favour the formation of solid and liquid products [37]. Additionally, the composition of the gaseous products can vary depending on the temperature, with higher temperatures promoting the production of lighter hydrocarbons such as methane and ethylene [63]. Overall, the pyrolysis temperature plays a crucial role in determining the outcome of the process and the properties of the resulting products. In addition to temperature, the reaction time also influences the yield and composition of the products [64].

Longer reaction times generally lead to higher yields, as more time allows for a greater extent of decomposition [64]. However, it is important to strike a balance, as excessively long reaction times can result in unwanted side effects and decreased product quality. The feedstock used in pyrolysis also impacts the final product composition [12], [65]. Different feedstocks, such as biomass or plastics, have varying chemical compositions, which can affect the types and amounts of products obtained [66]. Furthermore, the presence of catalysts during pyrolysis can significantly alter the product distribution [67], [68], [69]. Catalysts can enhance certain reactions and

selectively promote the formation of desired products [70]. Overall, optimizing pyrolysis conditions, including temperature, reaction time, feedstock choice, and catalyst selection, is crucial for achieving desired product yields and compositions in this versatile process.

[62]The charred sample particle size is considered as it can influence the operating regime. Large particles can result in mass transfer limitations, and small particles tend not to be representative of the parent coal samples [55]. Additionally, the particle size distribution affects the overall efficiency of the coal conversion process [71]. Smaller particles have a larger surface area, allowing for faster reactions and increased conversion rates [72]. However, they also tend to agglomerate and form clumps, leading to potential blockages in the system [72]. On the other hand, larger particles may not fully react due to mass transfer limitations, resulting in incomplete conversion and lower yields of desired products [43], [50], [59]. Therefore, finding an optimal particle size range is crucial for achieving maximum efficiency and desired product yields in coal conversion processes. By carefully controlling the particle size, operators can ensure better process control and improve overall performance in coal conversion systems.

2.1.2 Overview of coal gasification

Gasification is the thermal decomposition process of any carbonaceous feedstock, whether solid, liquid, or gaseous, in the presence of an externally supplied oxidizing agent (pure oxygen, air, or steam) [73], [15]. The feedstock undergoes partial oxidation, and heat is released. After the oxidation step, heat is released in a high temperature environment, allowing for the formation of other gases, such as carbon dioxide or steam, to react with the feedstock. The resulting autothermal breakdown produces carbon monoxide, hydrogen, and occasionally methane [74].

These product gases, also known as synthesis gases or syngas, are the smallest stable chemical units that still convey some energy. The composition of the syngas is linked to the operating conditions of the gasification process as well as the quality of the feedstock [33].

Coal gasification is therefore the process of converting coal to synthesis gas through a series of chemical reactions. The coal is mainly converted to H_2 and CO during gasification through heterogeneous chemical reactions [15], [33], [34]. Commercially, the gasification process is carried out in gasifiers such as the fixed-bed dry bottom (FBDB) gasifier [30]. The gasifier is operated at relatively high pressures (20–100 bar) and temperatures greater than 700°C. The

coal is fed together with a mixture of steam and oxygen (O_2) or air and allowed to react, forming synthesis gas [15], [33], [34].

The various gasification technologies have different feedstock requirements because not all coals are equally suitable for gasification. The most significant differences are observed in the moisture content, ash yield, ash melting temperature, and available grain size [75]. Low rank coals (lignite or bituminous) with high ash yield, moisture, or sulphur content are principal candidates for gasification [15]. These coals are frequently not suitable for any other applications, such as coking and combustion [33].

2.1.3 Coal char gasification reactions

The main reactions taking place during the gasification process are shown in Table 5 [33], [76]. The standard enthalpy of carbon formation has been taken as ΔH_0 = 12.5 kJ/mol, and all enthalpies have been given for standard conditions (1.013 bar and 298 K) [76].

Table 5: Summery of char gasification reactions

Carbon dioxide gasification reaction		
$C(s) + CO_2(g) \rightarrow 2CO(g)$	ΔH_0 = 172.7 kJ/mol	[2.1]
Steam gasification reaction		
$C(s) + H_2O(g) \rightarrow CO(g) + H_2(g)$	ΔH_0 = 131.5 kJ/mol	[2.2]
Methanation reaction		
$CO(g) + 3H_2(g) \rightarrow CH_4(g) + H_2O(g)$	ΔH_0 = -206.2 kJ/mol	[2.3]
Water-gas shift		
$CO(g) + H_2O(g) \rightleftarrows CO_2(g) + H_2(g)$	ΔH_0 = -41.2 kJ/mol	[2.4]
Reaction with hydrogen		
$C(s) + 2H_2(g) \rightarrow CH_4(g)$	ΔH_0 = -74.9 kJ/mol	[2.5]

The heterogeneous primary reactions (Reaction 2.1 and 2.2) are slower than the gas phase reactions and are usually regarded as the most important gasification reactions due to their significant influence on the gasification rate [52], [77], [78]. These endothermic reactions take place between the carbon (C) within the char and the gasifying agent (CO_2 and Steam) [51], [52]. The CO_2 gasification reaction (Reaction 2.1), also known as the Boudouard reaction, is slower

than the reaction with steam (Reaction 2.2) and serves as a reference for fundamental gasification studies [33], [36], [40].

From the above equations, it can be seen that CO and H_2 are the main product gases, but the formation of methane can also occur and is strongly dependent on the H_2 partial pressure [79], [80]. The methanation reaction (Reaction 2.3) is strongly dependent on the H_2 partial pressure and plays a significant role at elevated pressures, while the water-gas shift reaction (Reaction 2.4) mainly proceeds at high steam concentrations [81]. The water-gas shift reaction (Reaction 2.4) influences the formation of CO as shown in Table 5, resulting in the formation of CO_2.

2.2 Factors affecting char reactivity

There are several factors to consider during coal char gasification. This section discusses and provides literature to support the most crucial factors. Section 2.2.1 illustrates the significance of coal char properties on the gasification rate and carbon conversion. Temperature is one of the most influential factors to consider and is discussed in Section 2.2.2. The influence of reactant (CO_2) partial pressure and concentration on carbon conversion is discussed in Section 2.2.3. Finally, the effects of total system pressure are discussed in Section 2.2.4.

2.2.1 Coal char properties and CO_2 reactivity

Coal char reactivity is affected by several factors, such as reaction conditions, sample preparation, physical char structure, and parent coal properties [82], [83], [84], [85].

Coal rank has a momentous influence on char gasification reactivity and kinetics due to the different coals exhibiting different extents of coal conversion and thermal behaviour during gasification [43]. Coal char reactivity is largely dependent on the maturity and type of parent coal, whereby reactivity increases with a decrease in coal rank [63], [86]. There is, however, no general trend for predicting gasification reactivity based on coal rank [87]. Engelbrecht (2008) and Miura *et al*. (1989) observed a decrease in coal reactivity with increasing coal rank, but Miura *et al*. (1989) observed scattered reactivity data for low-rank coals. There is thus no accurate and reliable model for the prediction of coal reactivity based on coal rank.

The coal char pore volume and porosity also decrease with an increase in coal rank, resulting in lowered gasification reactivity [43]. This is due to the larger concentration of active sites within the

coal matrix of low-rank coals compared to that of high-rank coals. Low-rank coals also consist of a higher volatile matter content, which plays a large role when released by increasing the pore structure and resulting in increased gasification reactivity [88].

Coal mineral matter is also known to affect gasification reactivity, especially at lower temperatures, due to the presence of catalytically active components [89], [90]. The mineral matter constituents catalyse the gasification reactions, resulting in an increase in gasification reactivity [89]. The mineral matter can also decrease coal char reactivity at high temperatures as a result of a decrease in the micropore surface area [89]. Koekemoer [91] observed that during the CO_2 gasification reactions of Highveld coals, K, Mg, and Ca act as catalysts. Hatting [92] and Zhang *et al*. [93] observed similar trends in that an increase in alkali index resulted in increased coal char reactivities. The alkali index has been used to describe the overall influence of catalytic components [94].

Everson *et al*. [95] reported pore volumes of 3.4 and 5.3 mm^2/g and surface areas of 1.39 and 3.46 m^2/g. These values can be seen as very low, which can be attributed to the high concentration of dense minerals present [18]. Mgano *et al*. [43] reported a higher micropore surface area of 249 m^2/g (daf basis) for a South African Highveld coal. Higher pore volumes result in higher adsorption capacity and increased reactivity [12], [43]. Higher adsorption capacity could be attributed to increased devolatilization of the reactive macerals at high temperatures [18].

The micropore surface areas play an important role in coal char gasification. According to Liu *et al*. (2000) and Siauw *et al*. (1984), the micropores can take up approximately 95% of the total surface area. Higher pressures resulted in increased surface areas [12], due to the larger amounts of smaller pores present at higher pressures, resulting in a higher surface area [12]. Tremel and Spliethoff [96] confirmed that the initial surface area after devolatilization is dependent on pressure and the micro to mesopore ratio is to be expected.

Many studies have been conducted on the maceral content of coal and its effect on coal pyrolysis [97], [98], [99]. Given that macerals are the basic components of coal, investigation of the pyrolysis behaviour of macerals can provide more information on the structural characteristics of the coal samples [100], [101]. The three main maceral groups considered are liptinites, vitrinites, and inertinites [76]. It is commonly expected that inertinite would be less reactive during combustion, but not all vitrinites are reactive, and not all inertinites are inert [102]. It has been found that vitrinite-rich coals from the northern hemisphere burn at a lower efficiency compared to the

Australian coals with a lower vitrinite content [103]. This is due to the high reflectance of inertinite macerals in the European coals compared to that of Australian coals [103]. Gondwana coals, on the other hand, can also be burned satisfactorily, even though they consist of a high inertinite content [103].

It is thus clear that not all inertinites are the same and must be regarded as different entities with different degrees of reactivity [102], [103], [104]. It has been observed that oxidized vitrinite behaves differently from most other vitrinites [103], [105]. During the petrographic analysis, the formation of particular morphotypes and changes in vitrinite reflectance were observed [105]. The changes observed in vitrinite reflectance during oxidation relate to the spontaneous combustion potential [105]. The extent of these changes is dependent on the operating regime, porosity, and the characteristic physical changes of the coal [105].

Depending on the rank and speciation, vitrinite combustion can vary from ‘very poor’ to ‘good’, influencing the reactivities [104]. Some vitrinites can be less reactive than some inertinites, and it is thus acceptable to assume that a certain fraction of inertinites can be reactive [55], [104], [105]. The inertinite component was found to be more reactive after the demineralization of the maceral concentrates to rule out any catalytic effects of the metallic impurities [104]. In some studies, the increase in inertinite content resulted in an increase in reactivity with seven coal samples of different ranks [94], [106]. Inertinite chars have reported higher aromaticity, higher carbon content, and lower hydrogen content compared to vitrinite chars [97]. Roberts [98] reported similar chemical structures for inertinite rich and vitrinite rich coals at 700 to 1000 °C, but the physical structures were different. Xu *et al*. [100] reported that inertinite rich chars are denser, contain larger crystallite averages, and a lower isotropy than vitrinite-rich chars.

The inertinite components showed higher reactivities than the vitrinite components, even after taking the catalytic effect of alkali compounds into consideration. Micrinite can be found within the inertinite group but can also be considered reactive during combustion [103]. This is due to the small surface area of macrinite, which is usually enclosed within vitrinite particles. Because of its possible connection with liptinite fragments, micrinite has been shown to yield more volatile matter than other inertinite species. As the vitrinite vesiculates, the enclosed micrinite will either be incorporated into the char walls and burned with the vitrinitic char or exposed and burned.

For macerals to be classified as reactive, some form of thermoplasticity must be exhibited during pyrolysis and char formation. Hence, if inerts are to be considered reactive, some degree of structural alteration must be visible.

2.2.2 Temperature

2.2.2.1 Ash fusion temperature

Studies have shown that the coal ash fusion temperatures are related to the ash composition [107]. The ash fusion temperatures generally decrease with alkaline composition and increase with acid oxides (TiO_2, SiO_2, Al_2O_3, etc.) [108], [109], [110]. The Si/Al ratio has a significant effect on the fluidity of the coal at high temperatures since Al_2O_3 and SiO_2 are the main components [111]. Al_2O_3 has a high melting point due to its ionic crystal structures, while quartz is mainly in the amorphous form [112]. Consequently, there is a general decrease in ash fusion temperature with an increase in the Si/Al ratio [112].

Liu et al. [113] investigated the relations between ash fusion temperatures and ash composition by using synthetic ashes consisting of CaO, Al_2O_3, Fe_2O_3, K_2O, and SiO_2, finding that increased Fe_2O_3 and higher Si/Al ratios resulted in lower ash fusion temperatures [112]. Chakravarty *et al*. [114] confirmed that Fe_2O_3 resulted in a decreased ash fusion temperature and quartz contributed to a higher ash fusion temperature. The influence of ash composition on fusion behaviour is, however, very complicated as the various components interact with one another, resulting in low melting eutectics and the formation of refractory minerals (mullite, quartz, kaolinite, and rutile) [110], [115].

2.2.2.2 Reaction temperature

According to several authors [51], [116], temperature has a significant influence on the rate-limiting step during gasification. At low temperatures, fewer active sites are available for gasification due to the smaller amount of microporous surface area available, resulting in lower carbon conversions [46]. Higher temperatures allow for the reactant gas to diffuse into the char particles at a significantly higher rate, thereby increasing the carbon conversion [46]. It has been proposed that heterogeneous gas-solid reactions occur in three temperature zones (Regimes) [117]. The coal kinetics and reactivities are influenced by the regime under which the gasification reactions take place. The Arrhenius plot in Figure 3 demonstrates the influence of temperature (inverse) on the overall reaction rate (logarithmic) [51].

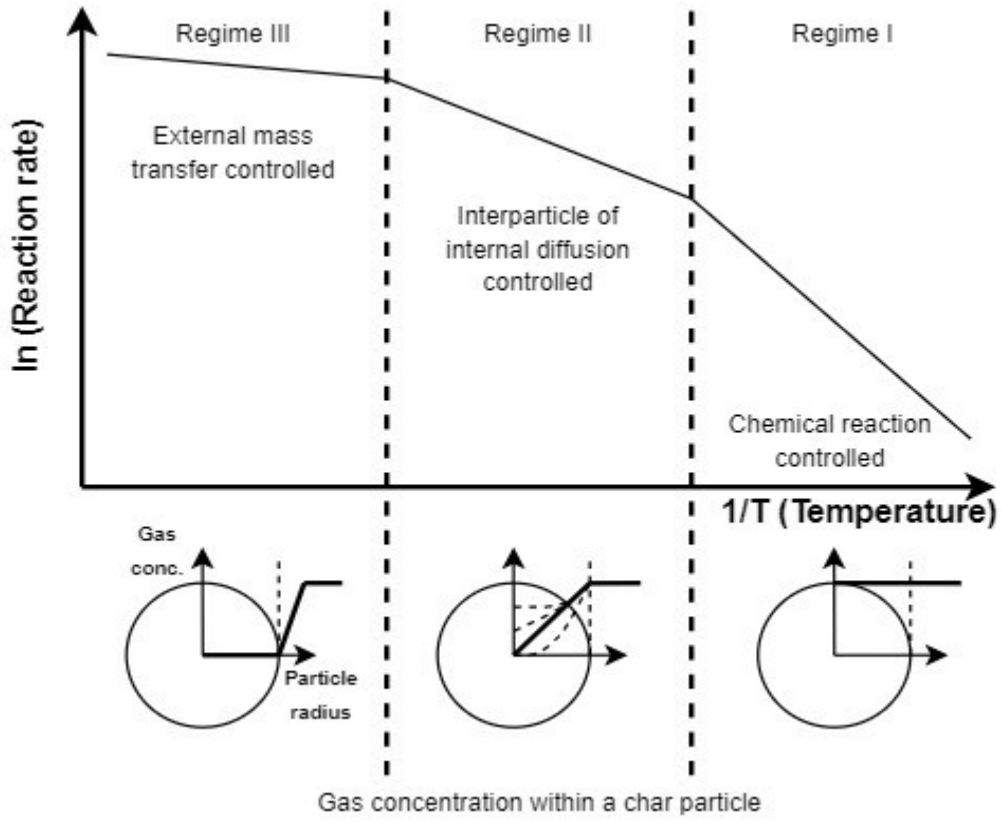

Figure 3: Effect of temperature on rate-limiting regimes (Adapted from [15], [51], [77]*)*

With an increase in temperature, the reaction rate shifts from chemical reaction controlled, to pore diffusion or external mass transfer controlled. The gasification rate increases exponentially with an increase in temperature during chemical reaction and internal diffusion-controlled regimes. The steeper gradient in Regime 1 (Figure 3) indicates a gasification rate increase that is more significant compared to that of Regime 2. Regime 1 conditions are usually achieved at temperatures below 1000 °C but can, however, differ depending on char properties [59], [96].

Entrained flow gasifiers are typically operated at temperatures around 1200-1600 °C (Regime 2), and the rate of diffusion of reagent gases through the pores of the char begins to influence the overall rate of conversion [117]. The conversion rate is limited by pore diffusion within the char particle [1] because the chemical reactions are predominately faster [15], [51], [59], [118].

The transition to Regime 3 typically occurs at temperatures in excess of 1500 °C, where the diffusion of the reagent gas through the boundary layer surrounding the char particle is the limiting factor [59]. Any change in flow rate and total pressure has a large influence on the gasification rate due to the difference in reagent gas concentration between the boundary layer and the

surface of the char particle [96]. These influences are more significant when larger coal char particles are used during gasification [119].

Mass transfer limitations have to be decoupled from the chemical or surface reactions commonly taking place in the internal surface area of the particle [40], [59]. The char kinetic parameters and intrinsic reaction rate experiments have to be conducted in the absence of mass transfer limitations in order to obtain suitable kinetic parameters for the development of gasification models [40]. Using smaller particles and conducting the gasification experiments at lower temperatures with high reagent gas flow rates allows for the elimination of mass transfer limitations [77], [118].

2.2.3 CO_2 partial pressure

Various authors have investigated the effect of CO_2 partial pressure on gasification reactivity by changing the system pressure at a constant CO_2 concentration [46], [52], or by changing the CO_2 concentration at a constant pressure [116]. A summary of the CO_2 gasification reaction orders determined in different high-pressure gasification studies is shown in Table 6. Usually, the CO_2 gasification reaction follows the CO_2 partial pressure reaction order, which is usually lower than one [1].

The effect of temperature on the gasification rate has been investigated in numerous studies, but with little focus on the effects of changes in reactant concentration. Shahabuddin *et al*. [46] investigated the influence of different CO_2 concentrations at different temperatures on carbon conversion, as depicted in Figure 4. The increase in temperature and CO_2 concentration resulted in higher carbon conversion [46]. These results are consistent with studies done by Sripada *et al*. [71] and Tanner *et al*. [59]. A 23% increase in carbon conversion was observed by increasing the CO_2 concentration from 10 to 20% [46]. The carbon conversion was, however, improved by 64% when increasing the temperature from 1000 °C to 1200 °C with a constant reactant concentration [46].

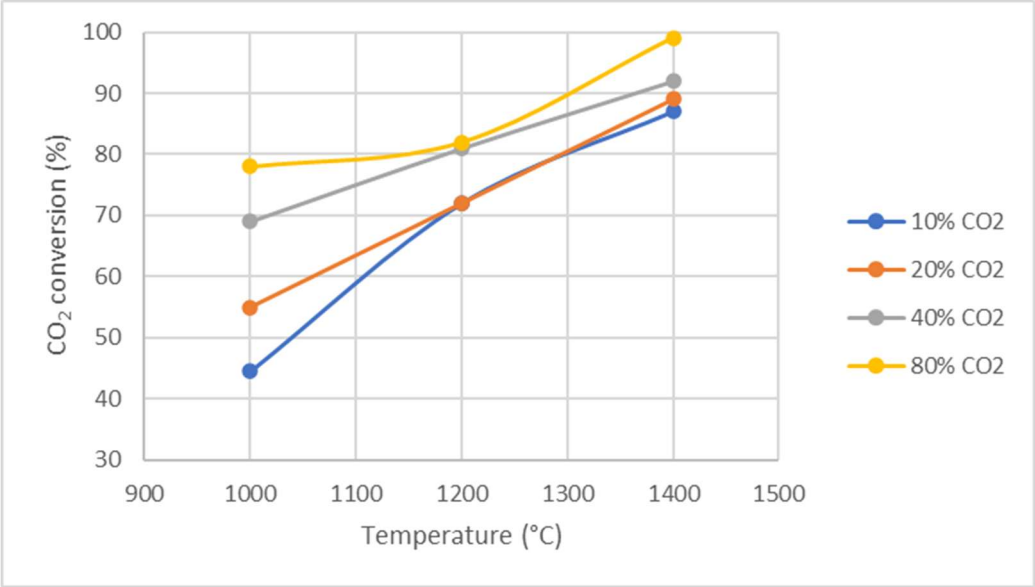

Figure 4: Effect of temperature and CO_2 concentration on carbon conversion (Shahabuddin et al. (2021))

The effect of CO_2 partial pressure on the degree of pore development in the mesopore and micropore surface areas were investigated by Gouws *et al*. [12]. It was determined that the mesopore surface areas of the chars were significantly higher at higher CO_2 partial pressures. The mesopore surface area and pore volume at 9 bar was observed to be more than double compared to those of the chars reacted at 0.1 bar. For the micropores, a maximum increase in surface area of 30 % was observed when the partial pressure was increased from 0.1 to 9 bar [12]. From this it is clear that the CO_2 partial pressure significantly influences the char gasification reactivity through pore development.

2.2.4 System pressure

The system pressure of the gasification rig has a large impact on the gasification reactions. Section 2.2.4.1 will contain literature on low-pressure gasification studies done as well as the main results obtained in these studies. Section 2.2.4.2 contains the high-pressure gasification studies done, and the results of these studies can be used as a basis for what to expect.

2.2.4.1 Low pressure CO_2 gasification

The low-pressure gasification studies are discussed in this section and summarized in Table 6. Xu *et al*. (2021) investigated the kinetic modelling of CO_2 gasification of Victorian brown coal using an entrained flow gasifier. The gasification reactions were conducted at atmospheric pressure

and temperatures ranging from 900 to 1000 °C. The rate of conversion increased with an increase in temperature, CO_2 concentration, and decreasing particle size [45], [46]. The outcome of the study showed that raising the CO_2 concentration, particularly at low CO_2 concentrations, had a favourable impact on the gasification rate of the two chars [45]. The CO_2 reaction orders for the TGA chars were determined to be 0.27 and 0.32 for the Maddingley and Yallourn chars, respectively [45].

Everson *et al*. [95] increased the pressure from 1 to 3 bar and observed an increase in the reaction time. Full conversion time increased by 25 hours with a pressure increase from 1 to 3 bar [95]. Veca and Adrover [47] attributed this to studies done by Everson *et al*. [95], confirming that the reaction rate is strongly dependent on temperature and pressure. This phenomenon was linked to chemical reaction-controlled conditions by Du Toit [48]. The carbon conversion of coal char significantly increases with an increase in temperature within the same residence time [45]. The main chemical reaction taking place is the Boudouard reaction, and this confirms the observed increase in conversion as a function of temperature [36]. CO_2 gasification is thermodynamically favoured, and the Boudouard reaction is endothermic [33], [36], [40].

Other parameters known to affect the gasification rate include mineral matter content, coal rank, particle size, and char structure. A wide range of activation energies have been observed by Koekemoer [91] at 0.875 bar due to the large difference in mineral matter content of the coal. The increase in coal rank resulted in a decrease in reactivity, as observed by Engelbrecht at an absolute pressure of 0.9 bar ([120]). The particle size has a significant influence on the carbon conversion, and reaction rate. The decrease in particle size resulted in an increased carbon conversion and this is mainly due to the effect of mass transfer limitations [12].

Table 6: Summery of low-pressure CO_2 gasification studies

Reference	Coal	Particle size (µm)	Temperature (°C)	Pressure (bar)	Model	E (kJ/mol)	Reaction order
Xu *et al*. (2021)	Victorian brown coal	20 - 38 90 - 106	900 - 1000	1.01	MVM, RPM	220, 198 - 208	0.27 and 0.32
Du Toit *et al*. (2013)	South African Highveld coal	1000	775 - 900	0.87	WM, LH	243	0.56
Everson *et al*. (2008)	Inertinite-rich coal	1000	850 - 900	1 - 3	RPM, PL	192 - 247	0.46 – 0.54
Engelbrecht (2008)	South African coal	850 - 1200	875 - 950	0.875	GM	184	-

MVM – Modified volumetric model, RPM – Random pore model, SCM – Shrinking core model, LH – Langmuir Hinshelwood, HM – Homogeneous model, PL – Power law, GM – Grain model

2.2.4.2 High pressure CO_2 gasification

Several studies on the effects of reactant partial pressures on gasification rate at reactant partial pressures of up to 50 bar are summarized in Table 7. The effect of CO_2 partial pressure on gasification reactivity has been studied by changing the system pressure while keeping the CO_2 concentration the same [52], [121], or by changing the CO_2 concentration while keeping the system pressure the same [116], [122].

Mgano *et al*. [43] evaluated and compared the reaction kinetics of steam and CO_2 gasification for selected Highveld coal at elevated pressures. The observed reaction order attributed to the effect of CO_2 partial pressure from 1 to 25 bar ranged from 0.46 to 0.50 [43]. It was found that coal char reactivity was dependent on reactant partial pressure [12], [52], [121], [122]. Park and Ahn [122] investigated the effect of CO_2 partial pressure at a constant temperature of 900 °C and 10 bar total pressure. A reaction order of 0.4 to 0.7 was observed for the five chars by varying the partial pressure from 1.8 to 4.95 bar.

The increase in reaction rate with partial pressure has been found to occur at reaction partial pressures of up to 15–20 bar [12], [40], [43]. The increase in reaction rate is attributed to the increase in surface complex concentrations. The reaction orders observed for CO_2 gasification were between 0.4 and 0.5 [52], and globally, the reaction follows a reaction order based on the CO_2 partial pressure, which is usually below one [1].

Roberts and Harris [40] investigated Australian bituminous and semi-anthracite chars and observed a reaction rate level off at high partial pressures using a pressurized thermo-gravimetric analyzer (PTGA). This phenomenon was confirmed by Park and Ahn [122] and Ahn et al. [123]. Ahn et al. [123] investigated an Indonesian sub-bituminous coal char at total system pressures up to 10 bar and 1300 °C using a pressure drop tube furnace (PDTF). The apparent reaction rate was proportional to the CO_2 partial pressure, estimated at 0.4 [123]. Some authors did, however, observe an increase in reaction rate with partial pressures of up to 40 bar [96], [124], possibly due to the effects of differences in coal ranks [37], [81], [125].

On the other hand, some authors found that a further increase in partial pressure did not affect the reaction rate as the increase resulted in the saturation of active sites [126]. The degree of saturation describes the desorption of the intermediate surface complexes, which several studies have found to control the apparent reaction rate [52], [127]. Roberts and Harris [52] determined

the concentration of the intermediate surface complex C(O) by performing temperature-programmed desorption (TPD) experimental work. The concentration of the intermediate surface complex C(O) refers to the complex of the CO_2 molecule adsorbed on an active site [12], [43], [52]. Based on these studies on Australian coal chars, the degree of saturation increased with an increase in reaction partial pressure from 1 to 30 bar.

The TPD analysis confirmed that the reason for the decrease in reaction order at high pressures was due to the saturation of active sites [52], [12]. The desorption peaks were similar for gasification at 20 bar and gasification at 30 bar [52]. So, the CO desorption concentration shows how much C(O) is on the surface of the intermediate complex at the end of the reaction [12]. This implies that the increase in reactant partial pressure past a certain point will not significantly influence the reaction rate due to the reactive surface becoming saturated with surface complexes [52].

Table 7: Summery of high-pressure CO_2 gasification studies

Reference	Coal	Particle size (µm)	Temperature (°C)	Pressure (bar)	Model	E (kJ/mol)	Reaction order
Mgano (2020)	South African Highveld coal	75 - 150	740, 780	20, 30	PL, LH, RPM	190	0.46 – 0.50
Gouws (2018)	South African Highveld coal	425 - 500	780 - 855	1 - 30	PL, LH, RPM	227, 211, 331	0.41 – 0.56
Tremel and Spliethoff (2013)	-	-	1200 - 1600	1 - 10	LH	200	0.41
Kim *et al*. (2014)	Berau coal (sub-bituminous)	75 - 800	750 - 1450	1 - 30	RPM, PL	149 - 152	0.85 – 0.98
Roberts & Harris (2011)		600 - 1000	900 - 950	0.4 - 20	LH	-	-
Park and Ahn (2007)	Alaska, Cyprus, Drayton, CNCIEC and Denisovsky coal	45 - 63	850 - 1000	5 - 20	SCM, PL	149 - 223	0.4 – 0.7
Roberts & Harris (2006)	Australian coal	600 - 1000	900 - 940	1 - 30	LH	-	-
Zang *et al*. (2006)		< 100	920 - 1050	2 - 10	SCM, PL	146 - 202	0.4 – 0.7

MVM – Modified volumetric model, RPM – Random pore model, SCM – Shrinking core model, LH – Langmuir Hinshelwood, HM – Homogeneous model, PL – Power law, GM – Grain model

2.3 Char structural development during gasification

Many studies have indicated that the gasification rate is not only dependent on reaction conditions but also on the physical char structure. The reactivity and structure of the chars are mainly determined by the rank of the parent coal and pyrolysis conditions [125]. These pyrolysis conditions include final temperature, heating rate, and soak time at final temperature [128]. Section 2.3.1 will elaborate on the observed changes in physical char properties. The effects of reaction partial pressure on gasification reactivity and supporting literature is discussed in Section 2.3.2. Finally, Section 2.3.3 will discuss the structural models.

2.3.1 Degree of conversion

The physical char properties can have a significant effect on the high-pressure CO_2 gasification kinetics [40], [116]. The char structure consists of different pores, of which the micropores (pore width < 2 nm) serve as the gas-solid reaction platform, the mesopores (2 nm < pore width < 50 nm), and macropores (pore width > 50 nm) serve as transport channels for reactant gases [129], [130]. The internal pore structure of coal chars has been measured using different methods such as SAXS (Small angle X-ray and neutron scattering), WXRD (Wide angle X-ray diffraction), SEM (Scanning electron microscopy), and TEM (Transmission electron microscopy).

Komarova *et al*. [130] determined the micropore, mesopore, and total surface areas in a range of carbon conversion extents ranging from around 10 to 80 %. The surface area development was determined for several temperatures ranging from 800 to 950 °C [130]. It was noted that the higher temperatures resulted in smaller surface areas [130]. The surface area development with carbon conversion at 800 °C is shown in Figure 5. The trend shown here differed slightly from the trend observed at higher temperatures. The total surface area increased in the early stages of char conversion, while the micropore surface area slightly decreased. After 10 % char conversion, the surface areas decreased; some more than others. Around 50 % char conversion, a low point was reached, followed by an increase in surface area up to the point of 81 % conversion.

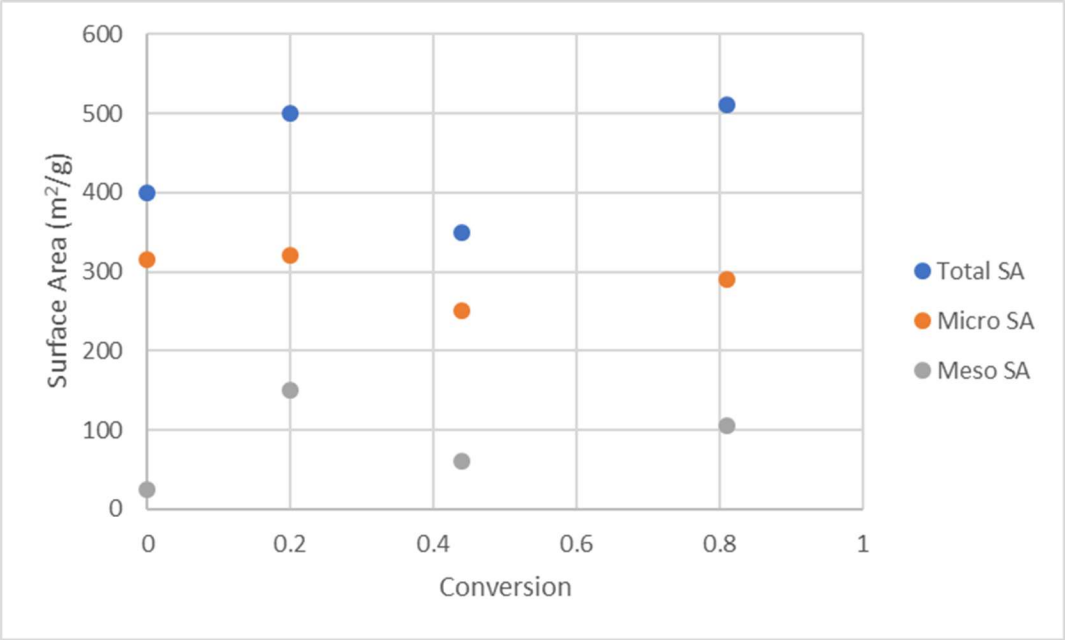

Figure 5: Surface area development during carbon conversion (Komarova et al. [95])

The physical structural development of the coal char involves the process of micropore development to mesopores, opening of closed pores, formation of micropores and overlapping of micropores [41], [129]. This is due to the continuous consumption of carbon during gasification [131], [132]. Gouws *et al.* [12] investigated the development of pores during gasification and found that the pore development is affected by the CO_2 partial pressure. The influence of partial pressure on the pore development of coal chars is further discussed in Section 2.3.2.

Several authors have observed physical changes in the char structure during gasification at high pressure [40], [41], resulting in the further investigation of different process conditions on the char structure development [12].

2.3.2 Reagent partial pressure

Moilanen and Mühlen [126] investigated the inhibitory effects of CO and H_2 on the gasification of peat char at high pressures. They also reported on the effects of reactant pressure on the gasification rate, and it was found that increasing the reactant partial pressure led to a decrease in reaction rate [126]. Roberts and Harris [42] believed that these unusual results could be attributed to the close physique-based fuzzy granular (PBFG) simulation conditions as well as the

deviation from regime 1 operating conditions [42]. Ultimately, the instrument-specific effects together with pore diffusion may have contributed to these unusual results [42].

Roberts and Harris [42] also investigated the coal char surface area development at different CO_2 partial pressures. The surface area development generally increased with an increase in CO_2 partial pressure at 900 and 950 °C. The influence of the CO_2 partial pressure did, however, decrease with an increase in pressure. The influence of the CO partial pressure between 1 and 3 bar resulted in the surface area development increasing with an increase in pressure, but any further increase in P_{CO} resulted in the development of smaller surface areas [42].

Lee et al. [128] investigated the char CO_2 surface area as a function of pyrolysis pressure and weight loss at pressures up to 36.5 bar and temperatures between 800 and 1325 °C. It was found that the surface area of the Illinois No. 6 bituminous coal char is generally lower when pyrolyzed at higher pressures [128]. When the partial pressures of H_2O and CO_2 went up, the reactivities of coal char went up, but the effect of reactant partial pressure is much less when the data is reported in terms of the intrinsic rate[42]. The effect of reactant partial pressure also depends on the coal char type and properties.

The thermoplastic properties of a coal are for example, influenced by the relevant surface area development during heating [125]. Thermoplasticity inhibits the development of micropores, while a small weight loss induces a significant increase in the micropore structure during secondary devolatilization [128]. The increase in CO_2 surface area is accompanied by decreased reactivity and residual volatiles.

2.3.3 Structural models.

Structural changes in the char particles are known to occur during gasification [12]. Structural changes are an important factor to consider when modelling the reaction as a function of conversion [133]. Several structural models, such as the Random-Pore Model (RPM), Grain Model (GM), Shrinking-Core Model (SCM), Langmuir Hinshelwood (LH), Volumetric Model (VM), and the Modified Volumetric Model (MVM), have been used to model char reactivity data. The RPM has proven to be the ideal model for describing char reactivity due to its incorporation of structural changes [60], [63], [116]. The changes observed in char surface areas are associated with coalescence and pore development during char conversion [60], [116].

Bhatia and Perlmutter [134] came up with an expression for the RPM that accurately describes the experimental data at isothermal conditions in the chemically controlled regime [38], [60], [81], [116], [127].

$$\frac{dX}{dt} = k_p(1-X)\sqrt{1-\ \psi(1-X)} \tag{2.1}$$

Where X is the conversion, k is the rate constant and ψ is the structural parameter determined from regression with experimental data and can be determined from the initial char properties and defined as:

$$\psi = \frac{4\pi L_0(1-\ \varepsilon_0)}{S_0^2} \tag{2.2}$$

Where L_0 is the pore length per unit volume. The RPM can also be written to include the initial porosity ε_0 as shown in Equation 2.3.

$$\frac{dX}{dt} = \frac{k_s(1-X)\sqrt{1-\ \psi(1-X)}}{(1-\ \varepsilon_0)} \tag{2.3}$$

The RPM can be expressed in terms of the specific reaction rate r_s as depicted by Equation 2.4.

$$r_s = \left.\frac{dX}{dt}\right/_{(1-X)} = r_{s,0}\sqrt{1-\ \psi In(1-X)} \tag{2.4}$$

Where $r_{S,0}$ (initial reaction rate) is defined by Equation 2.5.

$$r_{S,0} = \frac{k_s S_0}{1-\ \varepsilon_0} \tag{2.5}$$

Where S quantifies the changes in the char surface area. With knowledge of the initial surface characteristics as described by Bhatia and Perlmutter [134], the degree of conversion is quantified by the RPM.

$$S = S_0\sqrt{1 - \psi In(1 - X)} \tag{2.6}$$

The structural parameter (Ψ) is indicative of the amount of pore growth that will take place during the reaction [134]. The structural parameter can be obtained through the measurement of pore structural properties, but it has been used as a fitting parameter [60], [116], [127], [129]. Several authors observed structural parameters from the measured conversion-time profiles ranging from 0.7 to 6.3 [18], [60]. Everson et al. [18] found that these parameters were less dependent on temperature and more on the reagent gas [116]. Structural parameters ranging from 3 to 130 have also been reported from the fitting of reaction rate data [116]. The larger structural parameters indicate that char pore development is more significant during gasification [116].

It has been proven that the RPM is superior to the GM model when predicting the surface area and CO_2 gasification rate of chars [116]. Even though the RPM is a good model for char reactivity, Kajitani *et al*. [116] found that the surface area (Equation 2.6) and the structural parameter obtained from the initial pore properties (Equation 2.2) are not very good at describing the reaction rate. The RPM can however not define the surface areas and reaction rates at the same time, suggesting that major structural changes remain unaccounted for if Ψ is assumed to be constant [50]. For this reason, there was a need to improve the RPM developed by Bhatia and Perlmutter [134].

2.4 Summary

Gasification is the process of converting coal, char, coke, or natural gas into synthesis gas, for the production of chemicals or use as liquid fuels [101]. Coal char gasification is a vital process in the fuel production industry. The gasification process is typically operated at high temperatures and pressures using oxygen and steam as gasifying reagents [43]. Numerous coal gasification studies have been conducted at low and high pressures using CO_2 and/or steam. It is clear from

the literature that the reactant partial pressure can have a significant influence on the gasification rate and surface area development.

Temperature is an important factor to consider, as the influence of temperature and its kinetic parameters have been rigorously reported in the literature. Large increases in reaction rates have been reported with increases in reactant partial pressures up to 20 bar. A further increase in reactant partial pressure resulted in the saturation of available active sites and ultimately a smaller influence on the reaction rates.

Due to the influence of coal and char properties, characterization is an important factor to consider when conducting experimental studies [135]. A significant portion of authors have investigated the coal and char properties, but there is still limited literature wherein the intrinsic coal properties are related to coal reactivity. Further investigation into the influence of coal and char properties on the reaction rates can aid in the optimization and future blending strategies.

Coals consist of a variety of organic compounds, elements, mineral matter, gases, moisture, and hydrocarbons, such that no two coals are alike [101]. From the literature, all these coal properties have been investigated at different temperatures and pressures [136], [137], [138], [139], [140]. The composition of coals can greatly affect their behaviour under various conditions, leading to differences in combustion efficiency, heat output, and emissions [140], [141],[142].

Due to the influence of coal and char properties, characterization is an important factor to consider when conducting experimental studies [135]. A significant portion of authors have investigated the coal and char properties, but there is still limited literature wherein the intrinsic coal properties are related to coal reactivity. This gap in research presents an opportunity for further exploration and discovery in the field of coal combustion. Further investigation into the influence of coal and char properties on the reaction rates can aid in optimization and future blending strategies.

This can provide valuable insights into the mechanisms governing coal combustion and gasification processes. Understanding how different coal properties affect reactivity can also help in predicting and controlling emissions of pollutants during combustion. Additionally, exploring the relationship between coal and char properties and reaction rates can lead to the development of more efficient and sustainable energy production methods.

For example, the porosity and surface area of coal and char particles can significantly impact their reactivity [143]. Higher porosity and surface area can enhance the access of reactants to the

active sites, leading to increased reaction rates [143]. On the other hand, the presence of mineral matter in coal can act as catalysts or inhibitors, further affecting the overall combustion or gasification process [144]. By studying these relationships, researchers can develop models and tools to predict and optimize the performance of coal-based energy systems.

Chapter 3: Research methodology

3.1 Introduction

The intrinsic coal and char properties can have a significant effect on gasification kinetics. The investigation into these properties can provide more information regarding the reactive behaviour of the coal samples. By correlating the intrinsic coal properties with the coal's reactivity, the gasification behaviour can be better predicted. In this chapter, the experimental setup and procedures used for the experimentation, as well as the statistical procedures are discussed.

Section 3.2 gives a brief overview of the coal samples and their origins. Section 3.4 discusses the preparation conditions and techniques used for coal and char preparation. Section 3.5 discusses the materials used, the experimental setup, the experimental procedures, and the data processing used to determine the coal char reactivities. Section 3.6 contains the characterization analysis and methods used for determining chemical, physical, and mineralogical properties. Finally, Section 3.7 contains a discussion on the coal/ char statistical modelling procedure.

3.2 Coal samples and origins

Seven South African medium rank C bituminous Highveld coals rich in inertinite with insignificant caking and swelling propensity were used. These coals are commonly used in commercial gasifiers and CTL technology. The exact mines and locations of these coals will not be disclosed due to confidentiality reasons. Seven coarse coal samples weighing approximately 3.5 kg each were received for this study.

3.3 Materials used

Table 8 contains a list of the materials used to conduct the pyrolysis and gasification experiments.

Table 8: Materials used

Material	Use
N_2 (> 99.99 %)	Used to ensure an inert environment for pyrolysis and gasification.
CO_2 (> 99.9 %)	Used as reactant for gasification process.
CO	Calibration gases for CO_2 analyzer - 1000, 1650 and 3900 ppm
Coal (2 – 3 cm)	Seven coarse coal samples

3.4 Coal and char preparation

3.4.1 Parent coal sample preparation

The coarse coal samples were crushed and milled individually to obtain the desired particle size distribution (PSD). The subsequent steps shown in Figure 6 were followed for each of the coal samples in preparation for coal pyrolysis.

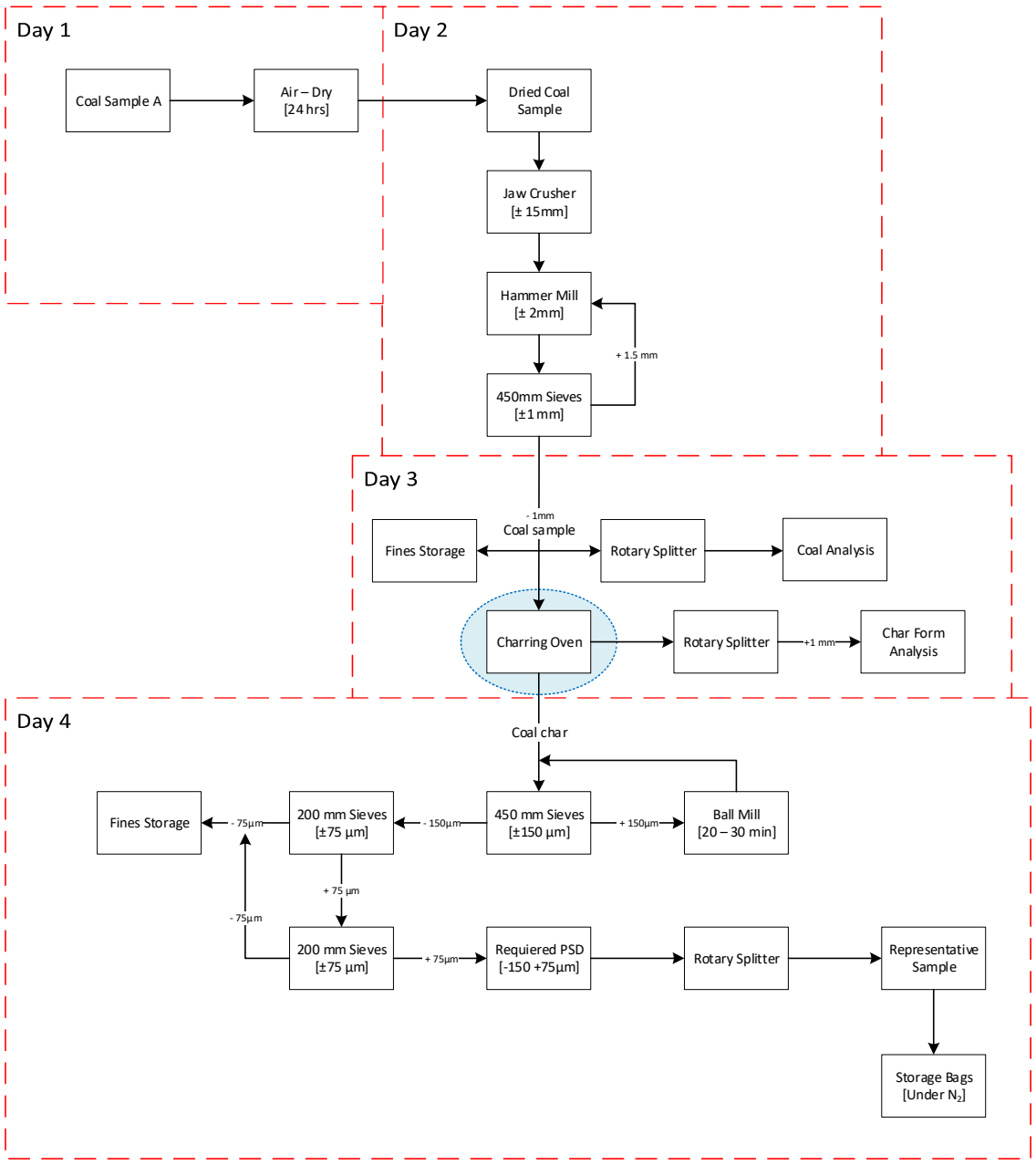

Figure 6: Coal and char sample preparation

The first step in the coal sample preparation involved air drying the samples for 24 hours in a temperature and humidity - controlled room before starting with the size reduction process. The lump coal samples were crushed to ±6 mm particles using an in-house jaw crusher. The samples were fed through the crusher a total of three times to ensure that most of the particles were in the required range of ±6 mm. The ±6 mm particles were then further crushed using a hammer mill. The hammer mill was employed twice for each sample to obtain the desired PSD of 1 mm ±500 µm. The ±1 mm samples were then placed in a ball mill for 30 min to further crush the samples.

The samples were sieved to obtain a PSD ranging from 850 µm to 1250 µm. The oversized samples were placed back in the ball mill for another 30 min and repeated until all the samples were within the -1250 µm to +850 µm PSD range. The undersized coal (-850 µm) was separated and stored under nitrogen in Ziplock bags (These samples were not used again). The cone and quartering approach was employed to achieve efficient homogenization of the coal samples. Each sample was placed on a clean flat surface, shaped into a cone and flattened as shown in Figure 7.

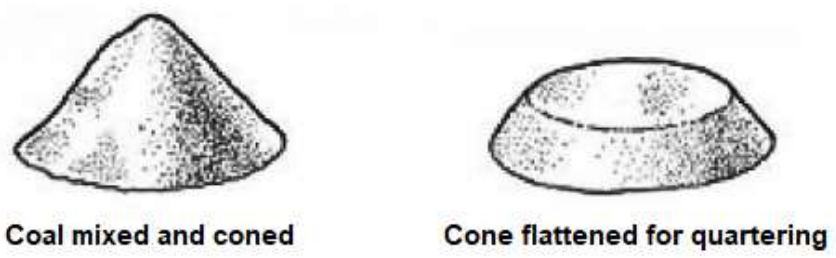

Figure 7: Step 1 & 2 of cone and quartering technique

After forming the cone, the samples were divided it into four quarters using a shovel. Typically, one of these quarters is selected randomly or systematically. Figure 8 illustrates the initial and subsequent stages taken to acquire the quarters.

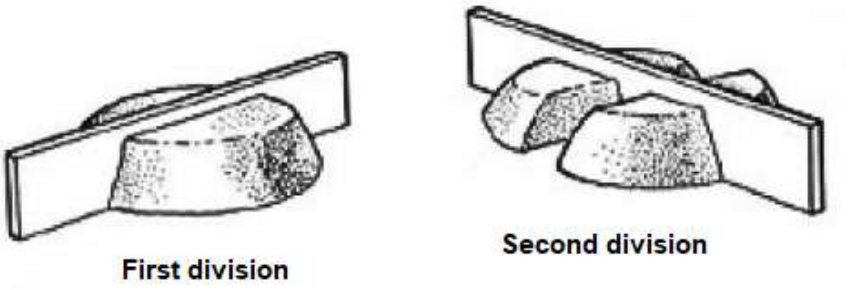

Figure 8: Step 3 & 4 of cone and quartering technique

The two quarters from the opposite ends are selected and set aside as shown in Figure 9. The remaining two quarters are reformed into a cone. The cone is again divided into quarters, and the process continues until a smaller sample size (±300 g) was obtained.

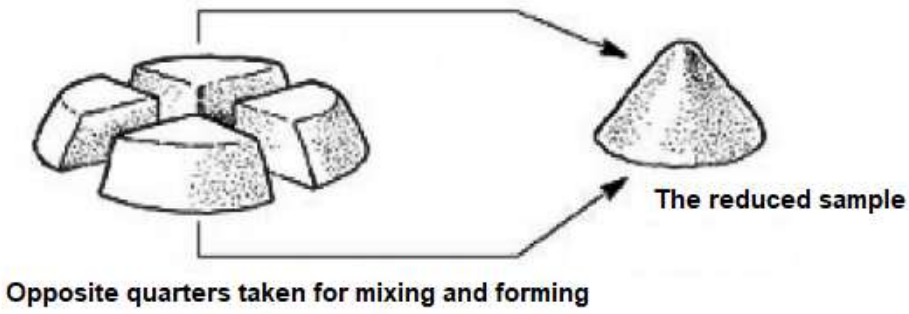

Figure 9: Step 5 & 6 of cone and quartering technique

The ±300 g sample (-1250 to +850 µm) was then placed in a rotary splitter to obtain a representative sample weighing around 160 g to be charred in the pyrolysis oven (charring) and a representative sample weighing around 25 g (-1250 to +850 µm) for the coal analysis. The 25 g samples were stored under nitrogen to be sent to Bureau Veritas for proximate, ultimate and XRF analysis. Bureau Veritas also conducted the mineralogical analysis and determined the gross calorific values using the standards and methods summarized in Table 12.

3.4.2 Coal char preparation (pyrolysis)

The coal samples (-1250 +850 µm) were charred using a laboratory-scale pyrolysis setup consisting of a Lenton® horizontal tube furnace, as shown in Figure 10. The horizontal tube furnace is surrounded by three heating elements controlled through set-point retransmission. The samples were placed in a ceramic sample boat with a length and width of 270 x 35 mm and a capacity of 200 g at the centre of the heated zone. The samples were charred in 160 g (±0.5 g) batches at a heating rate of 10 °C/min to 900 °C and maintained for 30 min at 30 bar. The pyrolysis experiments were conducted in an inert environment using nitrogen and at non-isothermal conditions to simulate typical gasification conditions. To avoid packing effects, the sample boats were only partially filled (approximately 2.5 cm deep) [60]. The conditions used for coal pyrolysis are summarized in Table 9.

Table 9: Pyrolysis operating conditions

Variable/Property	Conditions
Mass per batch	160 g
Temperature	900 °C
Pressure	30 bar
Heating rate	10 °C/min
Hold time	30 min
N_2 flow rate	5 NL/min

After the charring process had been completed, the furnace was depressurized to atmospheric pressure. After the furnace pressure stabilized, the system was allowed to cool to room temperature at a natural cooling rate while remaining in an inert atmosphere. This cooling process was necessary to prevent any potential reactions or combustion that could occur if the system was exposed to oxygen [54]. Additionally, maintaining an inert atmosphere during the cooling process ensured the preservation of the charred material's properties [116].

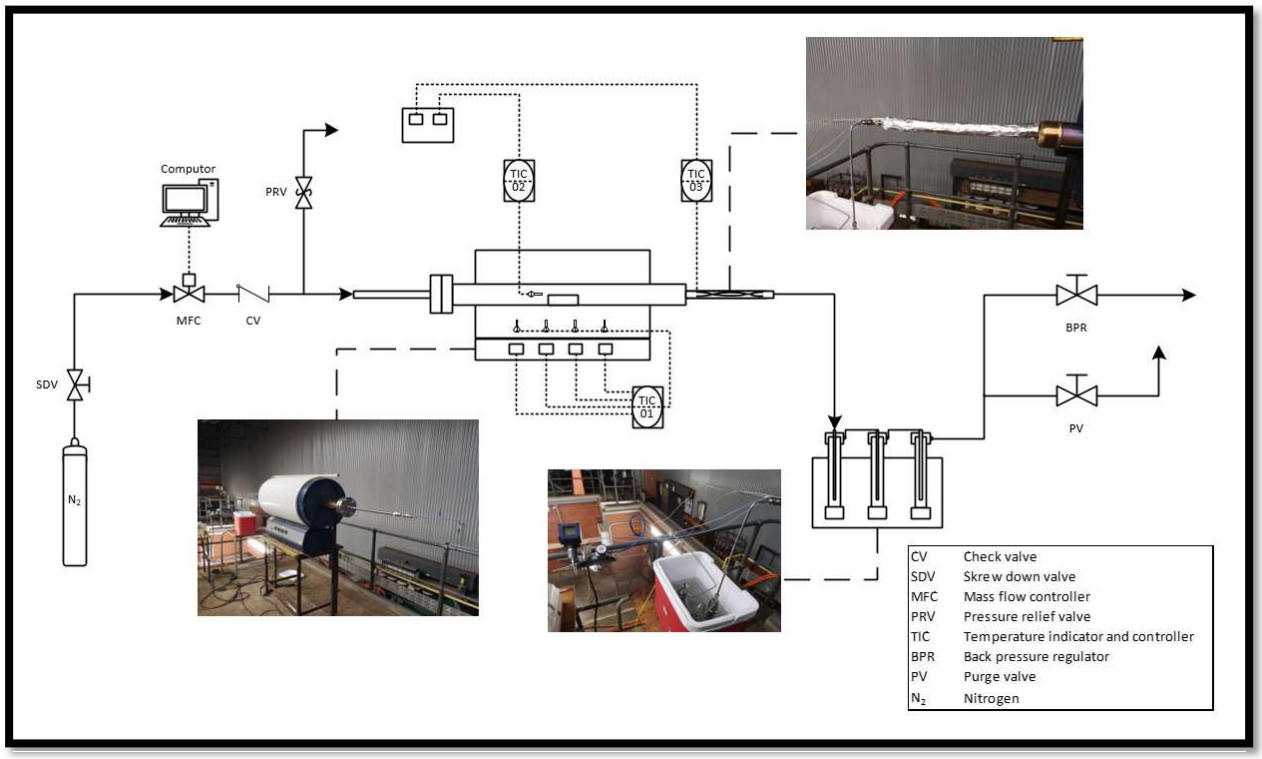

After the (-1250 +850 µm) coal samples were charred, a rotary splitter was used to ensure that a representative sample could be taken for the characterization analysis and the gasification experiments. The char sample (-1250 +850 µm) used for characterization weighing 15 g was subjected to proximate and ultimate analyses through Bureau Veritas to determine its composition and heating properties. Another 15 g (-1250 +850 µm) char sample was sent to Bureau Veritas for the char petrography analysis to be conducted. The remaining char samples (individually) were placed in the ball mill for further size reduction.

The char samples were placed in the ball mill for 30 min increments, sieved, and the oversized particles (+150 µm) were continuously crushed and sieved until the particles were within the -150 +75 µm range to be used for the gasification experiments. The ball mill consisted of containers filled with ceramic balls. The coal and char samples were sieved using a range of 450 mm laboratory sieves to obtain the required sample range of -150 +75 µm. A 150 µm sieve to retain larger particles was placed on top of a 75 µm sieve to separate the undersized particles from the sample and then placed on a laboratory scale sieve shaker.

A rotary splitter was then used to obtain a representative char sample (-150 +75µm) to be stored under nitrogen in zip lock bags and placed in containers to be used for coal char gasification studies. The rotary splitter ensured that each gasification experiment received a representative sample. The desired sample size (0.5 g) was carefully measured and placed into individual containers. These samples were then ready to be used in the gasification experiments to study the behaviour and characteristics of the char under different conditions.

3.5 Coal char gasification

The coal char samples (-150 +75 µm) were used for CO_2 gasification experiments. This section discusses the high-pressure fixed bed reactor (HPFBR) used for conducting the gasification experiments with the intent to determine the char gasification rates. The char gasification rates were determined through carbon-based product gas analysis by measuring the carbon monoxide (CO) concentration throughout the gasification process.

In Section 3.5.1 the materials used to conduct the gasification experiments are described. Section 3.5.2 contains the experimental setup and description of the gasification rig used to obtain the

reactivities of the coal char samples, followed by the experimental procedures, given in Section 3.5.3. Finally, the equations used for determining the carbon conversion and specific reactivities are given in Section 3.5.4.

3.5.1 Materials used

A summary of the materials used are shown in Table 10.

Table 10: Materials used for gasification experiments

Substance	Specification/ purity	Supplier
CO calibration gas	1000, 1650 and 3900 ppm	Afrox
CO_2	> 99.9 %	Afrox
N_2	> 99.99 %	Afrox

CO calibration gases, balanced with N_2, were used to calibrate the gas analyzer (see Appendix C). Instrument grade CO_2 and baseline N_2 obtained from Afrox were used for the gasification experiments. CO_2 was used as a reactant, and N_2 was used as an inert atmosphere during sample heating and pressure build-up in the gasification experiments.

3.5.2 Experimental setup and description

A high pressure fixed bed reactor (HPFBR) was used for conducting the gasification experiments of coal char particles. The rig was designed, constructed and commissioned in-house for conducting low- and high-pressure steam/ CO_2 gasification experiments. For the purpose of this study, the steam generation and condensation system were by-passed and a small particle range (-150 +75 µm) was used. A detailed schematic of the experimental rig is presented in Figure 11. The equipment description as well as operating range is summarized in Table 10.

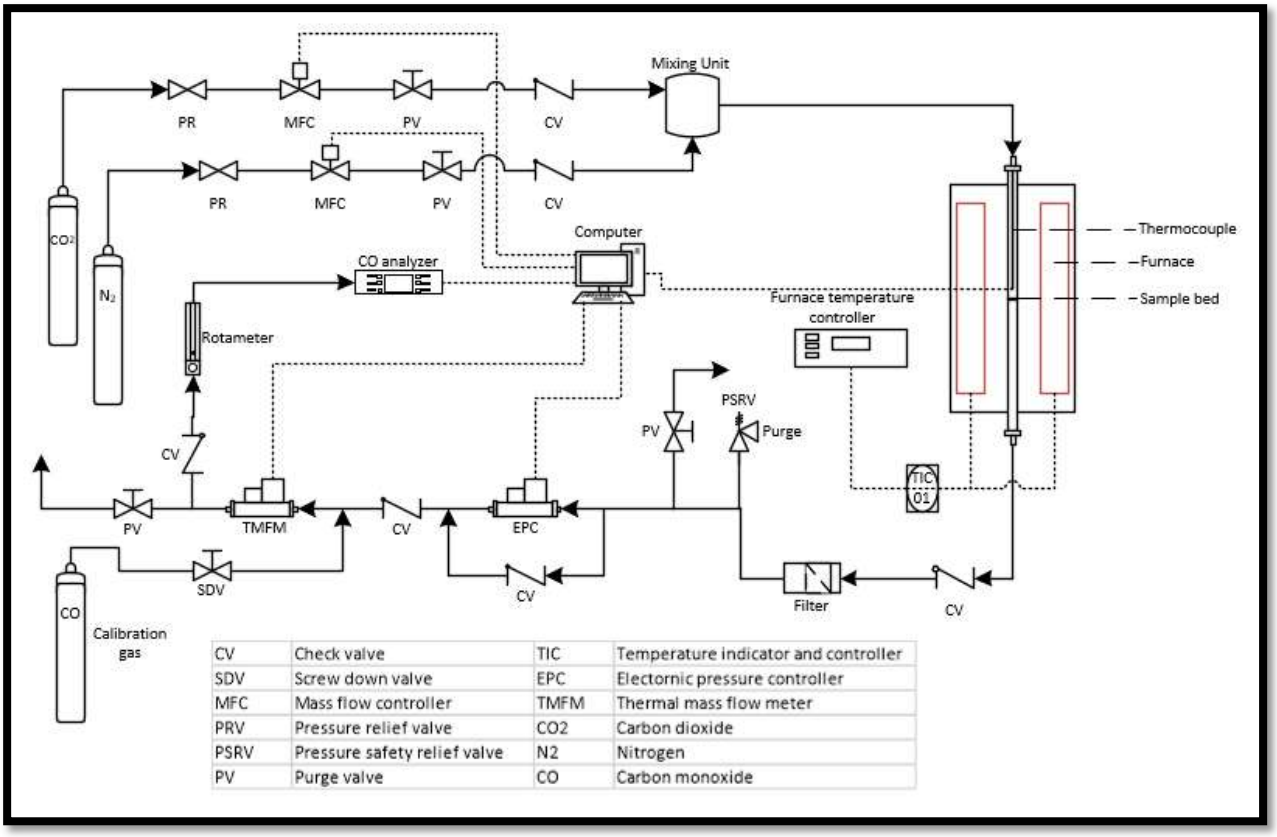

Figure 11: High pressure gasification rig

The gasification rig consists of a vertical split furnace with a temperature range of up to 1200 °C, providing sufficient power for endothermic gasification reactions. The sample is placed on a porous quartz frit (nominal pore size: -75 +40 µm) mounted to a flange at the centre of the reactor pipe. The furnace encloses the pipe with a heating length of about 40 cm and an isothermal heating zone of 5 cm [12]. The reaction temperature inside the pipe is monitored by a K-type thermocouple located 5 mm above the sample bed. The N_2 and CO_2 are fed from standard gas cylinders, controlled by two-stage regulators (gauge pressures of 0 – 52 bar). The gases are introduced at the top of the reactor and controlled using mass flow controllers (MFC) (0 – 5 NL/min) (calibration is provided in Appendix C).

At the outlet of the reactor, the product gas line passes through an electronic pressure controller (EPC), maintaining a constant total system pressure. The EPC can maintain pressures up to 80 bar, which is measured upstream using a pressure transmitter. A thermal mass flow meter (TMFM) is used to determine the gas flow rate going through the EPC to the CO/CO_2 analyser. The gases pass through the CO/CO_2 gas analyser, where the carbon containing gases from the

gasification experiments are measured before being purged. In this study, only the CO content was measured using the analyser as the analyser was not able to measure the CO_2 being fed into the system (>40 000 ppm).

Table 11: Summary of equipment used (Gasification rig)

Equipment	Model/description	Range/precision
Furnace	Carbolite® VST 12/100/200	Ambient to 1200 °C
Reactor pipe	Multi-alloys® C276 alloy	Ambient up to 120 bar and 1000 °C
CO/CO_2 analyser	ADC® MGA3000 analyser	NDIR: 200 to 40000 ppm
EPC	Bronkhorst® type EI-Press	Ambient to 80 bar
Pressure transmitter	Wika® Unitrans	Ambient up to 120 bar
CO_2 MFC	Bronkhorst® type EI-Flow	0 to 5.0 NL/min
N_2 MFC	Bronkhorst® type EI-Flow	0 to 0.75 NL/min
TMFM	Bronkhorst® type EI-Flow	0 to 2.0 NL/min

3.5.3 Experimental procedures

A char sample of approximately 0.50 g was weighed using a Mettler Toledo laboratory scale (Microsep®, MS-TS analytical balance) and placed onto the quartz frit in the reactor. N_2 was then allowed to flow through the rig at a specified flow rate of 0.58 NL/min for 15 minutes while the furnace was pre-heated to the desired reaction temperature. After the desired temperature had been reached, the furnace was enclosed around the reactor. N_2 was still allowed to flow through the gasification rig until the reaction temperature stabilized.

After reaching constant flow and isothermal conditions, the EPC and N_2 were used to pressurize the rig to the desired system pressure and regulated using a two-stage regulator. The data logging of total pressure, reaction temperature, and CO concentration was then started after the desired system pressure had been reached. After the data logging started, CO_2 was introduced (2.28 NL/min), and the N_2 flow was stopped. After the desired conversions were reached and the data logging stopped, the CO_2 flow was stopped while N_2 was reintroduced into the gasification rig and left running while dislocating the furnace and depressurizing the rig.

This allowed the converted chars to be flushed with N_2 while the reactor was cooled to ambient conditions. When the reactor reached ambient pressure and temperature, the N_2 flow was stopped, and the partially reacted char was collected.

3.5.4 Coal char reactivity

The reaction rate of char gasification in a CO_2 atmosphere was determined in order to evaluate the char reactivity by determining the carbon conversion. The equations used for determining the carbon conversion are discussed in this section.

3.5.4.1 Carbon conversion

A carbon mass balance was done (Appendix B) to measure the carbon monoxide (CO) concentration produced, because the complete conversion of the char particle can be explained from the formation of CO (evaluated through the carbon mass balance) for more than 98.7 % conversion. Carbon monoxide is measured because it is the primary product of the gasification reaction [145]. Equation 3.1 shows the mathematical expression for determining the carbon conversion.

$$r_C = \frac{y_{CO}\dot{n}MW_C}{2} \tag{3.1}$$

Where y_{CO} is the fraction of CO, ṅ is the molar flow rate (mol/s) and MW_C (g/mol) is the molecular weight of carbon. Next, $m_{C,t}$ is the total amount of carbon converted at each time interval (Δt) and is calculated using Equation 3.2. In this scenario, dt is equal to 3 seconds because the measurement of the CO concentration in the reaction is being taken at intervals of 3 seconds.

$$m_{C,t} = \int_0^t r_C dt \tag{3.2}$$

The instantaneous mass presented by Equation 3.2 is the amount of mass fed, attributed to the amount of carbon present within the char sample. The carbon content introduced into the reactor is primarily determined by the carbon content of the char sample, which consists of volatile matter,

ash, and fixed carbon. The instantaneous mass (Equation 3.2) can also be rewritten as a combination of Equation 3.1 and 3.2 as shown by Equation 3.3.

$$\Delta m_{C,t} = \int_{t_0}^{t_i} r_C dt \approx \frac{\Delta t}{2}\left(\sum_{i=1}^{n}\left(r_C(t_{i-1}) + r_C(t_i)\right)\right) \tag{3.3}$$

Where t (sec) is the time and r_c is the carbon conversion rate. The carbon conversion is calculated as shown in Equation 3.3.

$$X_C = \frac{m_{C,0} - m_{C,t}}{m_{C,0}} = \frac{m_{C,t}}{m_{Char,0}\left(1 - x_{ash,db}\right)x_{C,daf}} \tag{3.4}$$

where $m_{C,t}$ (g) is the instantaneous carbon mass, m_{Char} (g) is the initial mass of the charred coal sample used, $x_{ash,db}$ is the ash content of the char on a dry basis, and $x_{C,daf}$ is the weight fraction of carbon initially present within the char on a dry-ash-free basis.

The measured CO concentration was first calibrated as discussed in Appendix B: Equipment calibration. The calibrated CO concentration profile of Sample F at 740 °C and 30 bar is presented in Figure 12 for the first two and a half hours of the gasification experiment. The CO concentration increased exponentially to a maximum of 1050 ppm after about 7 min. The CO concentration started to decrease and stabilize around 70 min. The initial rise at the start of the run can be a consequence of dynamic system interruptions after CO_2 gas flow was introduced. Reaction rates are only shown from the point where they stabilised (around 4 % conversion) due to this initial peak in the CO concentration.

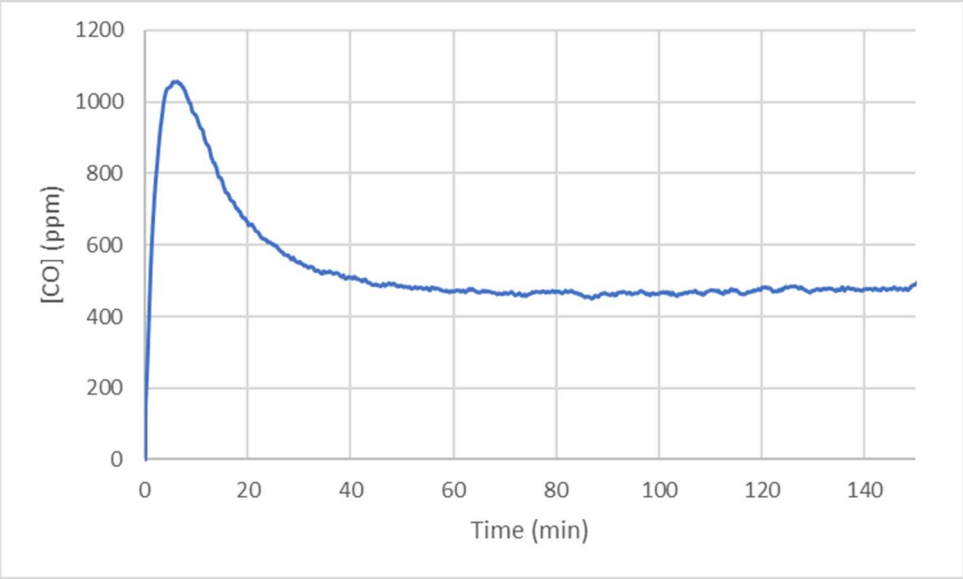

Figure 12: CO concentration profile with time (Sample F)

During the evaluation and comparison of the of the coal char reaction rates, the initial peak is not considered to allow for better comparisons by assisting in the isolation of the underlying differences or patterns between coal samples [146]. It makes it possible to comprehend the true variations present [146]. Gouws *et al*. [12] also reported an initial peak in reaction rates from 0 to 3 % conversion [12]. Mengjie *et al*. [147] reported that the reaction rate of in-situ char exhibited an initial increase followed by a drop. They attributed this behaviour to the gas changeover step, the rise in graphitization degree, and the inhibitory influence of minerals [147].

3.5.4.2 Specific reaction rate

The specific reaction rate is the normalized rate of change of carbon converted (X) with the unreacted carbon mass present in the sample [43]. Equation 3.5 presents the specific reaction rate r_s (g/g/s) based on conversion (X) [64], [130], [131].

$$r_s = \frac{1}{1-X}\frac{dX}{dT} \tag{3.5}$$

Based on literature, Equation 3.5 is used for describing char reactivity by quantifying the rate of reacted carbon relative to the unconverted carbon mass at a specific time. Because the data is not really continuous (every 3 seconds), a numerical approach is used to determine the derivative term (dX/dt) in Equation 3.5, as depicted in Equation 3.6:

$$\frac{dX}{dt} = \frac{\Delta X}{\Delta t} = \frac{X_i - X_{i-1}}{t_i - t_{i-1}} \quad (3.6)$$

From Equation 3.5, the carbon conversion can be expressed in terms of the carbon mass. Substituting the conversion (X) in Equation 3.5 with Equation 3.4 would result in the specific reaction rate being determined from the knowledge of carbon conversion as expressed by Equation 3.7.

$$r_s(g/g/s) = \frac{1}{1-X}\frac{dX}{dT} = \frac{1}{m_{C,0} - \Delta m_{C,t}}\frac{d\Delta m_c}{dt} = \frac{1}{m_{C,t}}\frac{dm_{C,t}}{dt} \quad (3.7)$$

A step by step example of the calculations used is presented in Appendix C:Gasification reactivity.

3.5.4.3 Activation energy

The activation energies are estimated using the Arrhenius equation as depicted by Equation 3.8.

$$\mathrm{k} = Ae^{\frac{-E_a}{RT}} \quad (3.8)$$

Where k is the reaction rate constant. A represents the pre-exponential factor of the Arrhenius equation, an empirical relationship between temperature and rate coefficient. E_a (J/mol) is the activation energy, R (8.31 J/mol·K) the universal gas constant and T (K) is the temperature. The Arrhenius equation can also be rewritten as depicted by Equation 3.9.

$$\ln k = \ln A - \frac{E_a}{RT} \quad (3.9)$$

The reaction rate Equation is depicted by Equation 3.10.

$$r = k[P_{CO}]^n \quad (3.10)$$

Where r is the specific reaction rate (g/g/s) and P_{CO} is the partial pressure (bar). Equation 3.10 can be rewritten in terms of the reaction rate constant k, as shown by Equation 3.11.

$$k = \frac{r}{[P_{CO}]^n} \tag{3.11}$$

Substituting Equation 3.11 into Equation 3.9, results in Equation 3.12.

$$ln\left(\frac{r}{P_{CO}^n}\right) = lnA - \frac{E_a}{RT} \tag{3.12}$$

Equation 3.12 can be further simplified

$$ln\, r - ln\,(P_{CO}^n)\; = ln\, A - \frac{E_a}{RT} \tag{3.13}$$

The partial pressure also remains constant for all the reaction rates in this study, Equation 3.13 can also be given as Equation 3.14.

$$\ln r = \ln(A.P_{CO}^n) - \frac{E_a}{RT} \tag{3.14}$$

The $\ln(A.P_{CO}^n)$ term remains constant at a constant pressure. To determine the activation energy of the coal char samples, a plot is made of the natural logarithm of r on die y-axis and 1/T on the x-axis.

3.5.4.4 Experimental uncertainty

Experimental uncertainty is a measure of the precision of the experiments and was calculated using Equation 3.15. The overall uncertainty was determined by considering the variation observed during an experimental run. The gasification experiments were repeated to determine the confidence interval and calculated using Equation 3.15 as determined by Devore and Farnum [148].

$$\bar{x} \pm z\frac{\sigma}{\sqrt{N}} \tag{3.15}$$

Where σ is the standard deviation, z = 1.96 for a 95 % confidence level [12], [148].

$$\sigma = \sqrt{\frac{\sum_{1=1}^{n}(x_i - \bar{x})^2}{N}} \tag{3.16}$$

x_i (g/g/s) represents each individual data point, $\bar{x}$ (g/g/s) is the mean of the data points and N is the total number of data points. The standard deviation for each run was calculated using Equation 3.16. The mean of the data points was calculated using Equation 3.17.

$$\bar{x} = \frac{x_1 + x_2}{2} \tag{3.16}$$

Using this method, an average experimental uncertainty of 0.04 g/g/s was obtained for the specific reaction rates of the coal char samples. More information (example) regarding the experimental uncertainty can be found in Appendix B:4. The experimental repeatability for Sample B and C at 750 °C and 30 bar is shown in Figure 13 and Figure 14 respectively.

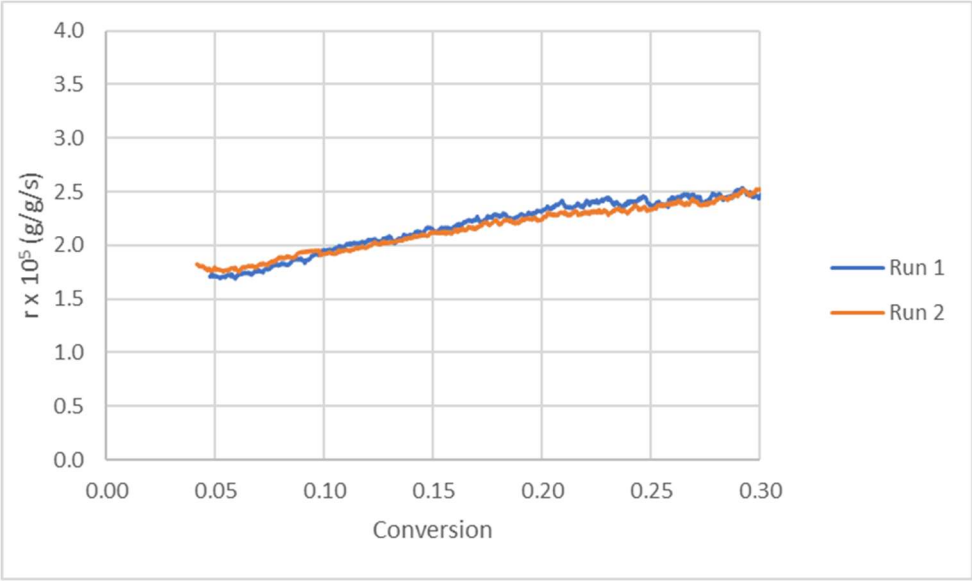

Figure 13: Sample B reaction rate repeatability, 750 °C, 30 bar

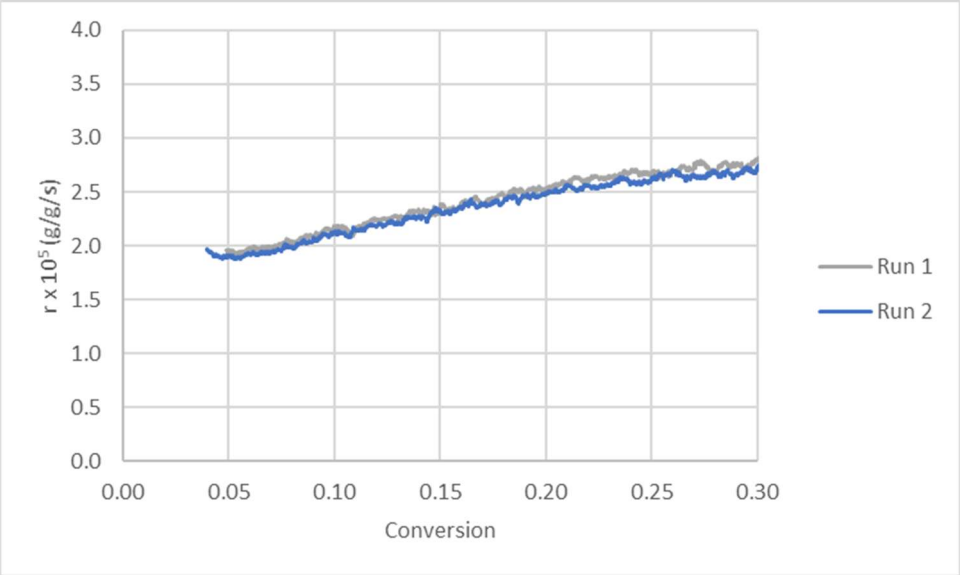

Figure 14: Sample C reaction rate repeatability, 750 °C, 30 bar

More information regarding the experimental uncertainty can be found in Appendix C:4.

3.6 Characterization analysis

The characterization analysis conducted on the coal and char samples as well as the standards used are summarized in Table 12. The chemical and mineralogical properties were investigated by Bureau Veritas, which included proximate and ultimate analysis, ash composition, and gross calorific values. The internal surface area of the coal chars was investigated in-house at the North-West University. The University of Johannesburg performed the petrographic and char morphology analyses.

Table 12: Summary of characterization analysis and standards

Parameter/Property	Standard/method used	Laboratory
Proximate Analysis		**Bureaus Veritas**
Inherent moisture (wt%)	ISO11722: 1999	
Ash yield (wt%)	ISO 1171: 2010	
Volatile matter (wt%)	ISO 562: 2010	
Fixed carbon (wt%)	By difference	
Ultimate Analysis		**Bureaus Veritas**
Carbon	ISO 12902 - CHN	

Hydrogen	ISO 12902 - CHN	
Nitrogen	ISO 12902 - CHN	
Oxygen	By difference	
Sulphur	ISO 19579: 2006	
Mineralogical Analysis		**Bureaus Veritas**
Ash composition (XRF)	ASTM D4326	
Gross Calorific Value		**Bureaus Veritas**
CV (MJ/kg)	ISO 1928:2009	
Surface area analysis		**North-West University**
Micropore surface area (m^2/g)	D-A method	
Mesopore surface area (m^2/g)	BET method	
Petrographic Analysis		**University of Johannesburg**
Maceral composition (Vol, %)	ISO 7404 - 3	
Microlithotype composition (Vol, %)	ISO 74.4 - 4	
Char form Analysis		**University of Johannesburg**
Char morphology	ICCP fly ash	

- **Chemical and mineralogical properties**

Proximate analysis and ultimate analyses were conducted based on the standards summarized in Table 12.

- **Structural properties: Surface area**

A Micrometrics 3-Flex analyzer was used to conduct the surface area analysis. In this study, the mesopore and mircopore surface areas were analysed. The char samples (~200 mg) were initially dried at a temperature of 105 °C for 4 hours. The mesopore surface area was then analysed using N_2 adsorption isotherms and the Brunauer–Emmett–Teller (BET) method [130]. The N_2 adsorption isotherms were measured at a relative pressure (P/P_0) range of 0.02 to 0.98. The mircropore surface area was analysed using CO_2 adsorption isotherms and the Dubinin-Astakhov (D-A) method [43], [116]. The CO_2 adsorption isotherms were measured at a relative pressure (P/P_0) range of 0.02 to 0.98 at 273.15 K. In addition, the characters underwent a degassing process within a vacuum environment with a pressure of 10 µmHg, at a temperature of 380 °C, for a duration of 24 hours.

- **Petrographic properties**

The coal samples were submitted to the University of Johannesburg (UJ) as +1 mm particles for the petrographic analysis to be conducted. The +1 mm char samples were used as received. The particles were set in epoxy resin under vacuum for 24 hours in order to make the polished blocks required for coal petrography. As per ISO 7404-2, the hardened blocks were ground to achieve a polished surface (final stage polish 0.05 µm OPS lubricant) using a Struers Tegraforce polisher.

The coal sample polished blocks were assessed using a Zeiss AxioImager M2M petrographic microscope fitted with a Fossil Hilgers system and a semi-automated point counting stage for petrographic point count analyses at a magnification of x500 under oil immersion. Maceral and Microlithotype analyses were conducted using the point count method. Results are reported on a volume % (vol%) basis, and all macerals are included in the maceral count (not determined by calculation).

The Microlithotype determination is a method used to analyse the mineral composition of coal char particles [101]. By classifying the char area falling within the 50 x 50 field of view, researchers can determine the progression of coal to char and ash during conversion [101]. This classification scheme developed by Wagner [101], provides valuable insights into the transformation of carbon particles and aids in understanding the conversion process.

- **Char morphology**

There is currently no standard procedure for the assessment of pyrolysis products or gasified chars. The classification for assessing fly ash has been suggested by the International Committee for Organic Petrology (ICCP) [101]. The chars prepared to 900 °C at 30 bar derived from coal particles ± 1mm in size were then assessed by adopting the fly ash classification scheme. The carbon-particle type classification scheme was developed by Wagner [101] to show the progression of coal to char and ash during conversion. The fly ash classification considers the whole particle or part of the char particle if the particle is larger than 50 x 50 microns. In the current study, most chars exceeded 100 microns, and hence the char area falling within the 50 x 50 field of view was classified. This approach is the same approach used in the Microlithotype determination [101].

The char sample polished blocks were assessed using the same equipment and point count method. There is no standard procedure for the assessment of gasified chars or pyrolysis products. The International Committee for Organic Petrology (ICCP) suggests a classification for assessing fly ash. The +1 mm feed coals are milled to pass 75 microns. A carbon-particle type classification scheme was developed by Wagner [101] and used previously in a gasification and pyrolysis research project. This scheme was developed to show the progression of coal to char and ash during conversion.

3.7 Coal/ char statistical modelling procedure.

The methods used for statistical modelling will be discussed in this section. Starting with the correlation of reactivity and temperature in Section 3.7.1, while the reactivity estimation based on the coal and char properties is explained in Section 3.7.2.

3.7.1 Correlating reactivity with temperature.

Equation 3.17 was used to correlate the reactivities of the coal samples. A statistical model was fitted on the reactivity data as a function of temperature and the different coal sources. The objective of the model is to predict reactivity for different coal sources at a specified temperature, within the experimental range. In addition, the difference in reactivity between the sources is also quantified through the model [149]. The model in Equation 3.17 was fitted to the reactivity data:

$$r = \beta_0 + \beta_{temp}x + \sum_{j=2}^{n} \beta_j Z_j + \sum_{j=2}^{n} \beta_{j,temp} Z_j x + \varepsilon \qquad (3.17)$$

where r is the reactivity, x the temperature, Z the indicator variables for the n different sources, except source one, which is Sample F, and $\beta_0, \beta_{temp}, \beta_j \; and \; \beta_{j,temp}, j = 2, \ldots n,$ are the regression coefficients to be estimated from the experimental data. Note the terms $Z_j x$ are the interactions between temperature and each of the coal sources, and the coefficients $\beta_{j,temp}$ represent the effect thereof on the reactivity. The errors ε are assumed to be independent and identically distributed with mean zero and constant variance σ^2. The coefficients of the model are estimated by least squares minimization. Consequently, the reactivities are obtained using Equation 3.18.

$$\widehat{r_s} = b_0 + b_{temp}x + \sum_{j=2}^{r} b_j Z_j + \sum_{j=2}^{r} b_{j,temp} Z_j x \tag{3.18}$$

where $\hat{r}$ is the predicted value of r, and b_0, b_{temp}, b_j and $b_{j,temp}$ are the least squares estimates of the coefficients in Equation 3.17.

The utilisation of multiple comparisons of means enables the examination of differences between means and the estimation of the magnitude of these differences [150]. The assessment of statistical differences between means can be conducted through the utilisation of statistical tools that are based on the fundamental principles of statistics. These tools involve the application of confidence intervals, hypothesis tests, or a combination of both [151], [152]. Tukey's honestly significant difference test is one of the most common and popular techniques for pairwise tests for variables with multiple levels [150].

The primary notion of the HSD is built on the basis of computation of the honestly significant difference between two means utilising a statistical method [150]. The procedure provides the true difference between two means at a specified confidence level [153]. Therefore, the difference in reactivity between every pair of coal sources at average temperature will be assessed through the Tukey HSD tests. The R^2values are also specified, as well as the parity plots of the observed versus predicted values in Section 5.2. The R^2 value is an indication of how well the model explains the variation in the reactivities. Further elaboration as well as an example can be found in Appendix F.1.

Coetzer *el al*. [154] used a similar model for a robustness study for a mixture and normal process variables. The optimisation of the Lurgi fixed bed dry bottom gasification process was conducted by dual response surface methodology [154]. This involved the implementation of response surface modelling and robustness analysis on the selected process variables [154].

3.7.2 Correlating reactivity with coal and char properties.

3.7.2.1 Statistical regression analysis

The primary goal of our statistical regression analysis is to uncover the correlations between various coal properties and reactivity at different temperatures. For simplicity and cost-effectiveness, focus has been placed on proximate analysis as it provides a fundamental

characterization, offering a comprehensive understanding of the link between coal quality and reaction rate. This grouping was specifically selected to consider volatile matter, carbon content, inherent moisture and fixed carbon with known relationships with reactivity. [4], [10], [116].

Moving beyond proximate analysis, the investigation delves into ultimate analysis, aiming to unravel the elemental composition of coal, specifically carbon, hydrogen, nitrogen, sulphur, and oxygen. The ultimate analysis grouping was selected because it is also an elementary characterization of coal, despite being less done and more expensive than the proximate analysis. Traditionally the ash yield included in this grouping is not part of the ultimate analysis. It has been chosen here since the sum of carbon, hydrogen, nitrogen, oxygen, sulphur, moisture and ash yield is equal to one (100 wt %) [99], [149].

A maceral grouping was also selected, with a focus on significant properties related to organic compounds like vitrinite, inertinite, and liptinite, allows for quantification and differentiation. It is essential to investigate the role of vitrinite, liptinite, and inertinite in coal reactivity in order to comprehend the gasification kinetics [23], [102]. Char morphology was also considered, and based on literature the physical structure and surface characteristics that influence coal reactivity a grouping was selected [127], [150].

Further, the catalytic effects of CaO, CaO/g coal and alkali index on coal reactivity was explored, acknowledging their potential influence during gasification [114], [116], [151]. Additionally, the Si/Al ratio was investigated to find a potential correlation with coal reactivity and offering valuable insights for optimising combustion processes [110], [152]. The Si/Al ratio is also indirectly included in the alkali index. The total reactives of the coal samples were also taken into account in this investigation, as they provide insight into the samples' gasification potential. The higher the reactivity, the greater the gasification potential [16], [153]. These properties were investigated individually and presented differently, since there is only an interest in the relationship between these individual variables and reactivity. For this reason, a contour plot is presented and no sensitivity analysis has been conducted.

The micropore and mesopore surface areas were also investigated based on findings reported in literature [132], [135]. From the data, no clear relationship was found between reactivity and surface are. **Error! Reference source not found.** (a) shows the relationship between reactivity and the micropore surface area. **Error! Reference source not found.** (b) shows the relationship between reactivity and the mesopore surface area. From these data points, there is no clear

relationship between the surface areas of the samples and their respective reactivities. For this reason, no grouping was done, and the statistical correlation was not evaluated further.

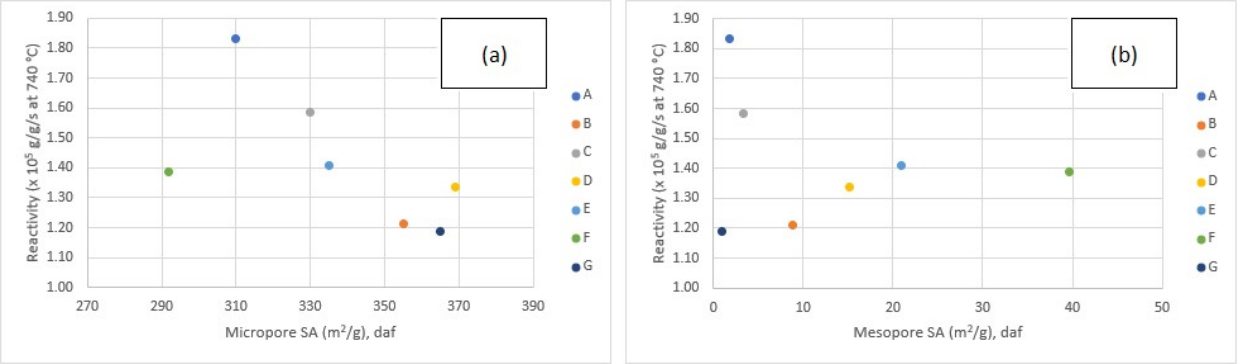

Figure 15: (a) Relationship between reactivity and micropore surface area. (b) Relationship between reactivity and mesopore surface area.

3.7.2.2 Sensitivity analysis

The sensitivity plots were generated using the correlated reactivity at 740 °C as this is the "average temperature" used in this study. Consider one variable with seven values. The data points of the variable are listed in ascending order as shown by Equation 3.14.

$$x_1 > x_2 > x_3 > x_4, > x_5 > x_6 > x_7 \qquad \begin{aligned} x_1 &= highest\ value \\ x_4 &= middle\ point \\ x_7 &= lowest\ value \end{aligned} \tag{3.14}$$

The difference of each point (x_1, x_2, …, x_7) from the middle value (x_4) is then taken to obtain the delta values.

$$\begin{aligned} \Delta x_1 &= x_1 - x_4 \\ \Delta x_2 &= x_2 - x_4 \\ &\dots \\ \Delta x_4 &= x_4 - x_4 = 0 \\ &\dots \\ \Delta x_7 &= x_7 - x_4 \end{aligned} \tag{3.15}$$

The list of delta values/ changes from the middle value, result in the centre point being zero (Middle point of new data). Now consider another variable with values ($z_1, z_2, \ldots, z_7$). Furthermore, assume that variables x and z form a composition where the sum of there values adds up to 100% for each point i.e., $x_i + z_i = 100, 1 = 1,2, \ldots,7$. Now the predicted values are obtained from the model for each value of x, while the values of z are adjusted to ensure the sum of the values remain 100% for each point. That is,

$$z_i = z_4(100 - x_i)/(100 - x_4) \tag{3.16}$$

where x_4 and z_4 are the middle values for the two variables. Plotting the predicted values against the delta values for x yields the sensitivity plot. This is also referred to as a trace plot. For example, the predicted reactivity was plotted against changes of fixed carbon, while the values of inherent moisture, volatile matter and ash yield were adjusted to ensure the sum of the components add up to 100% for each point. This procedure was followed for all the models that is a function of compositional variables.

Reactivity was estimated as a function of the coal and char properties. Equation 3.17 was used for this purpose [148].

$$y = \beta_{temp}x + \beta_1 P_1 + \cdots + \beta_n P_n + \varepsilon \tag{3.17}$$

where y is the reactivity, x is temperature,P_i is the proportion of the specific property of the coal, and ε is the error term which is assumed to be independent and identically distributed with mean zero and constant variance σ^2. The predicted values are obtained using Equation 3.18;

$$\hat{y} = b_{temp}x + \sum_{j=1}^{n} b_j P_j \tag{3.18}$$

where $\hat{y}$ is the predicted value of y, and b_j, b_{temp} are the least squares estimates of the coefficients in Equation 3.17. The coefficients of the model are displayed in Section 5.2. The calculation procedure together with an example is summarized in Appendix F.2. To better explain the above groupings as well as the relationship between the variables and reactivity, sensitivity plots were generated as given in Section 5.2.

Chapter 4: Coal and char characterization results.

The proximate, ultimate, CV and XRF analysis results are discussed in Section 4.1. The petrographic analysis results (microlithotype and macerals) are summarized in Section 4.2, followed by the char morphology results in Section 4.3. Finally, the surface area analysis is given in Section 4.4.

4.1 Chemical properties

Section 4.1.1 contains the CV, proximate and ultimate analysis results of the coal and coal char samples. Section 4.1.2 contains a summary of the XRF analysis of the coal samples used in this study.

4.1.1 Proximate and ultimate analysis

The proximate, ultimate analysis and gross calorific values of the parent coal and their respective chars are presented in Table 13 and Table 14 respectively. These coal samples are all Medium Rank C bituminous coals.

The inherent moisture content of Samples C, E and G are all in the lower range (3 wt% - 3.5 wt%). Samples A, B and F contain larger amounts (4.4 wt% - 4.7 wt%) of inherent moisture, with Sample D consisting of the highest moisture content. The inherent moisture contents reported here are slightly higher than the value reported by Mgano *et al*. [47], and within the same range as reported by Henning *et al*. [2]. Mgano *et al*. [47] and Henning *et al*. [2] both investigated typical Highveld coal samples, showing good agreement.

Sample A shows the lowest ash yield, and Sample E the highest. The ash yields of the coal samples are within the expected range of 15 - 30 wt% as reported by several authors for South African Highveld coal [2], [16], [47]. It is clear from the parent coal properties that these are low-volatile (18 – 24 wt%) and high-ash (> 22.5 wt%) coals [16].

Table 13: Coal chemical properties.

Sample		A	B	C	D	E	F	G
Proximate Analysis (wt % a.d.b.), Bureau Veritas Testing and Inspectors South Africa								
Inherent moisture	(ISO11722: 1999)	4.4	4.4	3.5	5.3	3.1	4.7	3.4
Ash yield	(ISO 1171: 2010)	22.5	27.8	34.2	25.7	41.0	29.6	39.3
Volatile matter	(ISO 562: 2010)	23.7	22.2	21.6	22.9	18.8	21.5	20.2
Fixed carbon	(by calculation)	49.4	45.6	40.7	46.1	37.1	44.2	37.1
Gross Calorific Value (MJ/kg)								
CV	(ISO 1928:2009)	22.7	20.7	18.9	20.7	16.4	19.2	16.9
Ultimate Analysis (wt % a.d.b.), Bureau Veritas Testing and Inspectors South Africa								
Carbon	(ISO 12902 - CHN)	58.7	53.3	48.4	54.0	42.8	50.4	44.3
Hydrogen	(ISO 12902 - CHN)	3.0	2.5	2.7	2.6	2.2	2.5	1.9
Nitrogen	(ISO 12902 - CHN)	1.5	1.4	1.2	1.4	1.1	1.3	1.3
Oxygen	(by difference)	9.1	9.0	8.3	10.1	8.2	8.7	8.1
Sulphur	(ISO 19579: 2006)	0.8	1.8	1.7	0.9	1.7	1.0	1.7

Sample A shows the highest fixed carbon and volatile matter content, while Samples E and G have the lowest fixed carbon contents, with Sample E also containing the least amount of volatile matter. The fixed carbon and volatile matter contents of these samples are within the expected range as reported by other authors [2], [16], [47]. When comparing the coal and char properties, it was clear that the char carbon content increased by 10 – 20 wt% after coal pyrolysis. The increase in carbon contents is generally similar to those observed in the literature for Highveld coal derived chars [16], [47], [94], [97].

In Table 14, the proximate and ultimate analysis results show only small amounts of inherent moisture and volatile matter present in the char samples when compared to those of parent coal samples (Table 13). Henning *et al*. [2] reported inherent moisture ranging from 0.6 to 1 wt %, ad for Highveld coal samples. The remaining traces of inherent moisture are likely due to the moisture adsorption characteristics of the coal samples as explained in the study of moisture adsorption and desorption characteristics of South African coals by Campbell e*t al*. [154].

Table 14: Char chemical properties.

Sample		A	B	C	D	E	F	G
Proximate Analysis (wt % a.d.b.), Bureau Veritas Testing and Inspectors South Africa								
Inherent moisture	(ISO11722: 1999)	0.9	0.7	0.6	0.7	0.5	1.1	0.8
Ash yield	(ISO 1171: 2010)	29.7	32.5	42.9	31.5	50.8	41.9	39.5
Volatile matter	(ISO 562: 2010)	1.8	1.3	1.0	2.1	1.1	2.4	2.0
Fixed carbon	(by calculation)	67.6	65.5	55.5	65.7	47.6	54.6	57.7
Gross Calorific Value (MJ/kg)								
CV	(ISO 1928:2009)	23.2	22.5	17.5	22.1	15.0	16.8	19.2
Ultimate Analysis (wt % a.d.b.), Bureau Veritas Testing and Inspectors South Africa								
Carbon	(ISO 12902 - CHN)	68.2	66.3	55.4	66.5	48.2	56.4	59.3
Hydrogen	(ISO 12902 - CHN)	0.2	0.1	0.0	0.1	0.0	0.1	0.1
Nitrogen	(ISO 12902 - CHN)	1.0	1.1	0.8	1.0	0.7	0.8	0.8
Oxygen	(by calculation)	0.0	0.0	0.0	0.0	0.0	0.0	0.0
Sulphur	(ISO 19579: 2006)	0.8	1.5	1.6	0.6	1.6	1.1	0.9

A volatile matter content of 4.47 wt. %, dry basis (db) has been reported by Komarova *et al*. [132] for a brown coal char sample. The amount of volatile matter in the coal char sample exhibits a relatively higher amount in comparison to other studies. Brown coals are known to possesses significant quantities of volatile matter as a result of its poor quality, specifically with regards to its lignite content [155]. Mafu *et al*. [153] conducted a CO_2 gasification study on biomass coal blends and their effect on coal gasification reactivity. From the proximate analysis of the coal char, lower amounts of volatile matter (0.6 wt %, db) were reported. Other authors have reported volatile matter contents in the range of 1.1 to 1.4 wt %, db for South African Highveld coal chars [2], [16], [47].

The coal samples were weighed before and after the pyrolysis process, as summarized in Appendix D (Table 39) in order to obtain the mass loss. The difference in moisture and volatiles between the coal samples have been added to obtain the percentage mass loss (moisture and volatiles). Figure 16 depicts the mass loss observed due to the pyrolysis process compared to the difference in volatile matter and moisture observed in the proximate analysis of the coal and char samples. The mass loss during the pyrolysis process is generally lower than the differences

observed between the coal and char samples. Zeng and Fletcher [74] investigated the effects of pressure on coal pyrolysis and char morphology and they observed a general decrease in mass loss with an increase in pressure.

Similarly, the mass loss observed during the pyrolysis process is lower when compared to the proximate analysis results [100]. This can be explained to the pyrolysis process being conducted at 30 bar and the proximate analysis at atmospheric pressure.

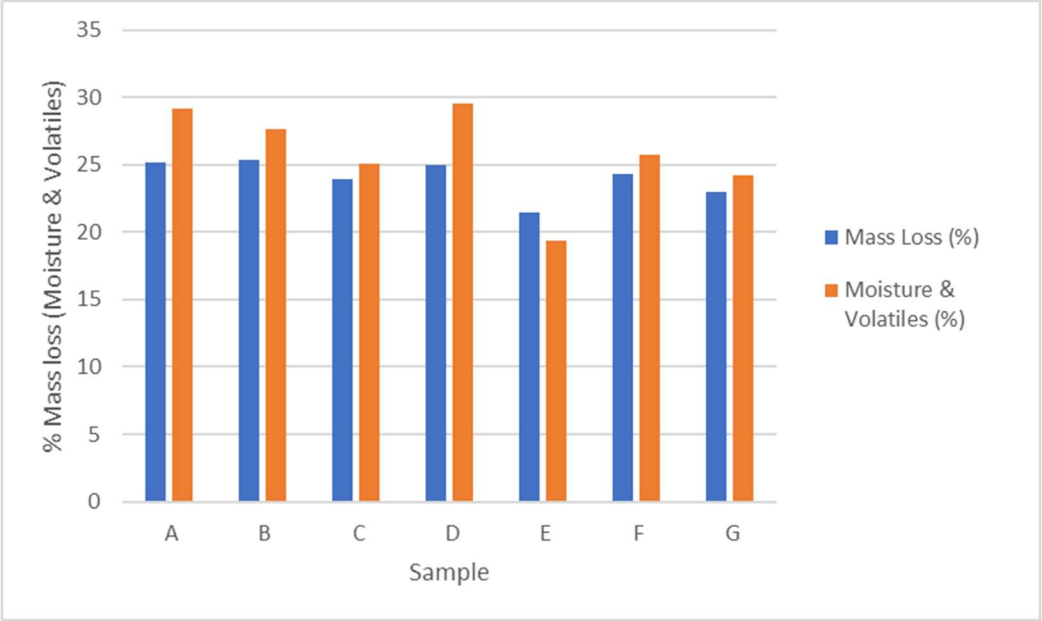

Figure 16: Change in moisture and volatiles after charring and mass loss after pyrolysis

Figure 17 shows the difference in carbon content between the parent coal samples and the coal char samples on a dry ash free basis. The coal char samples reported in Figure 16 were obtained by pyrolysis at 900 °C and 30 bar for 30 min. Sample A showed the smallest (16.9 wt % dry-ash free basis (daf)) increase in carbon content, and Sample G showed the highest (19.7 wt % daf) increase in carbon content. *Mgano et al.* [43] reported a 17.4 wt % daf increase in carbon content after pyrolysis for Highveld coal. Mgano *et al*. [43] charred for 30 min at a different temperature and pressure of 950 °C and 87.5 kPa respectively, and the changes in carbon content are within the same range. Gouws *et al.* [12] reported an increase in carbon content of 17.1 to 18.9 wt % daf. The range reported by Gouws *et al*. [12] for Highveld coal is within the same range as depicted in Figure 17. Gouws *et al.* [12] charred at 950 °C and atmospheric pressure for 2 hours.

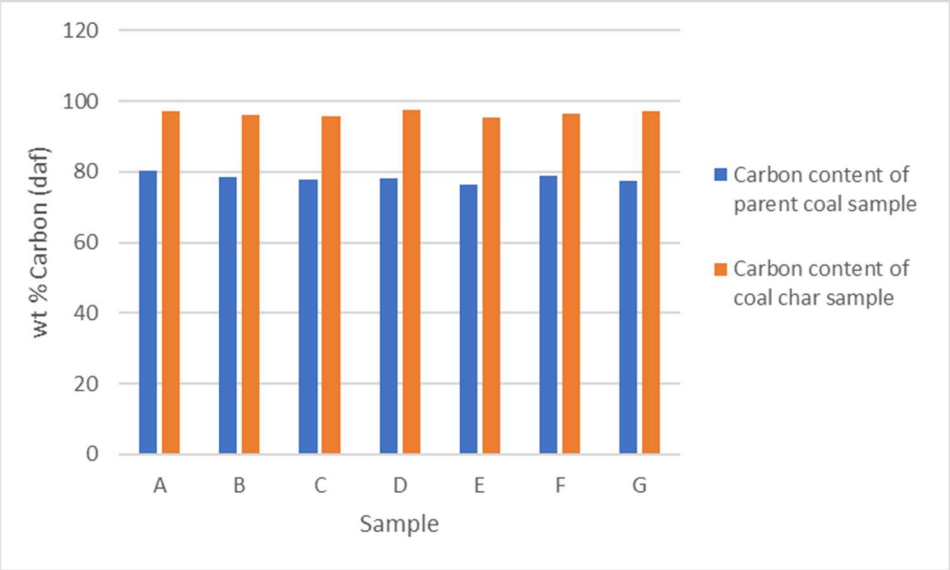

Figure 17: Carbon content of coal and char samples dry ash free basis

The hydrogen content within the coal char samples decreased on average by 3.7 wt %. Compared to literature, the decrease in hydrogen content is as expected [12], [43]. The hydrogen content of the coal itself can vary depending on the type of coal (e.g., lignite, bituminous, anthracite) [97]. The presence of more hydrogen-rich compounds in coal can lead to higher reactivity and faster reaction rates [97].

From literature, large amounts of oxygen within the coal particles convert into gaseous phase oxygen during pyrolysis, with only an insignificant amount of oxygen remaining within the coal char samples [161]. From the ultimate analysis of the coal char sample, it is clear that there is a negligibly small amount of oxygen remaining within the char samples. Compared to other studies done on Highveld coal chars, there is an insignificant amount of oxygen remaining within the coal char after pyrolysis [12], [43].

The results obtained from the proximate and ultimate analysis before and after pyrolysis corresponds to the results obtained by Gouws *et al*. [12] and Mgano *et al*. [43] of Highveld coal samples.

4.1.2 Ash composition (XRF)

The results of the XRF analysis of the parent coal samples are reported as elemental oxides in Table 15.

Table 15: Parent coal ash composition

Sample	A	B	C	D	E	F	G
XRF, Bureau Veritas Testing and Inspectors South Africa (wt %) (L.O.I. free basis)							
Al_2O_3	26	22	27	24	21	27	21
CaO	8.9	6.9	3.8	9.8	2.9	3.8	6.4
Cr_2O_3	0.0	0.0	0.0	0.0	0.1	0.0	0.1
Fe_2O_3	3.1	7.1	7.6	4.2	8.6	8.5	6.5
K_2O	0.6	0.6	0.8	0.7	1.3	0.8	0.9
MgO	2.4	2.0	1.0	2.3	1.0	1.0	1.9
MnO	0.0	0.0	0.0	0.0	0.0	0.0	0.0
Na_2O	0.3	0.2	nd	0.3	0.1	0.0	0.1
P_2O_5	1.1	0.7	0.4	0.7	0.2	0.4	0.3
SiO_2	49	56	53	52	60	52	56
TiO_2	1.4	1.2	1.6	1.4	1.1	1.6	1.2
V_2O_5	0.0	0.0	0.0	0.0	nd	0.0	0.0
ZrO_2	0.1	0.1	0.1	0.1	0.1	0.1	0.1
BaO	0.3	0.2	0.1	0.1	0.1	0.1	0.1
SrO	0.4	0.3	0.1	0.3	0.1	0.1	0.2
ZnO	0.0	nd	nd	nd	nd	nd	nd
SO_3	6.6	7.3	4.0	5.2	3.6	4.2	5.6
Alkali Index	4.6	6.4	5.6	5.9	7.1	5.3	8.1

From these results (Table 15) it is clear that the samples consist of high amounts of Si and Al containing species. Several authors have reported similar findings for bituminous high-ash yield coals [15], [43], [44], [92]. High amounts of quartz and kaolinite minerals have been reported in coals with high amounts of Si and Al [92], [43].

Sakawa *et al*. [94] introduced an alkali index as a means to quantitatively assess the catalytic capabilities of mineral matter. The alkali index can be mathematically expressed as the division of the total mole fractions of alkali compounds by the total mole fractions of acid compounds present in the ash, then multiplied by the ash content found in the coal sample as depicted by Equation 4.1 [94].

$$Alkali\ Index = ash\ (wt\ \%)\ x\ \frac{Fe_2O_3 + CaO + MgO + Na_2O + K_2O}{SiO_2 + Al_2O_3} \quad (4.1)$$

The alkali index of the coal samples is reported in Table 15. Numerous researchers have confirmed a strong association between gasification reactivity and the alkali index [87], [162], [163]. Specifically, an increase in the alkali index corresponds to a heightened catalytic impact [87], [162], [163].

Table 16 contains the Si and Al content as reported by Wang *et al*. [112]. As discussed in Section 2.2.2.1, there is a general increase in ash fusion temperature with an increase in Si and Al content. Flow temperatures ranging from 1200 to 1520 °C have been reported for coal ash with SiO_2 values ranging from 30.7 to 44.8 wt % and Al_2O_3 values ranging from 18.02 to 36.5 wt % [112]. Wang *et al*. [112] found that large amounts of SiO_2 and Al_2O_3 are unfavourable to ash fluidity as the ash fusion temperatures are extremely high. The SiO_2 content is slightly lower that the values reported in Table 15, and the $Al2O_3$ content reported by Wang et al. [112] is within the same range.

Table 16: Si/Al ratios compared to literature [112].

Sample	SiO_2 / wt %	Al_2O_3 / wt %	Fusion temperature (°C)
C00	44.8	36.3	1520
C01	41.5	36.5	1465
C02	44.3	34.9	1345
C03	31.7	19.4	1200
C04	31.8	18.0	1247
C05	30.7	27.8	1340

Average SiO_2 and Al_2O_3 values of 43.5 % and 35.9 % respectively had fusion temperatures in the range of 1476 °C [112]. The Si/Al ratios reported by Wang et al. [112] are relatively close as opposed to the ratios reported in this study. Generally, it is the fluxing elements which lower the ash fusion temperatures (AFT) [112], the alkaline index is thus a good metric to consider. As can be shown in Sample G (8.1), a greater Alkali Index denotes a larger concentration of alkali oxides (Na_2O and K_2O). By serving as catalysts in coal gasification, these alkali metals can speed up the gasification reaction rates [164]. Process efficiency may be enhanced by a quicker conversion of coal into syngas as a result of this enhanced reactivity [165].

High alkali content, however, can also result in problems with operation, including sticky deposits forming or slagging problems inside the gasifier, which can make maintenance more frequent and complex [164]. Samples with a lower Alkali Index, such as A (4.6), may exhibit a slower gasification rate due to the reduced catalytic action of alkali metals [112]. Even while it could be less effective, this could help the gasifier by lowering slagging and fouling, which could lead to a more stable operation over time [166].

There is a large Si to Al ratio reported for all the coal samples in this study. Al and Si are acidic components, whereas the basic components are fluxing constituents [167]. These ratios are favourable to lower ash fusion temperatures, increasing the likelihood that mineral matter blockage of pores could have occurred [112]. The pyrolysis experiments were conducted at 900 °C, which is significantly lower than the ash fusion temperatures reported by Wang *et al*. [112]. This indicates that no melting takes place, leave the pores accessible.

The high amounts of quartz and kaolinite mineral grains in the ash of the parent coals are in agreement with Si and Al content as reported in the XRF analysis Table 15 [63], [92]. High pyrite values of 10 vol% and higher as well as fine clays were observed in some of these samples as summarized in **Error! Reference source not found.** (Appendix E) [168], [169]. Yang *et al*. [170] reported that the there is a decline in apparent activation energies with higher amounts of pyrite. When comparing the apparent activation energies to the pyrite content, Samples B and E have the highest activation energies and a lower pyrite concentration. Sample G has the lowest activation energy and a higher pyrite concentration, indicating that the relationship between pyrite and activation energy does however need to be investigated further.

The sulphur content in coal can be categorised into two types: organic sulphur and inorganic sulphur. Among the several forms of inorganic sulphur, pyrite (FeS_2) is commonly recognised as the predominant form of inorganic sulphur [170]. The study conducted by Sujanti and Zhang [171] examined the impact of inorganic substances on the behaviour of coal oxidation. The findings of their research indicated that the presence of pyrite facilitated the process of spontaneous combustion in coal [171]. Table 17 contains the pyrite values obtained from the maceral analysis as well as the iron (III) oxide identified in the XRF analysis.

Table 17: Comparison between Pyrite and Fe_2O_3 from XRF analysis

Sample	A	B	C	D	E	F	G
FeS_2/ Pyrite (vol %)	3.1	11.3	4.1	6	11.6	8.9	6.9
Fe_2O_3 (wt %)	3.1	7.1	7.6	4.2	8.6	8.5	6.5

The oxidation of pyrite has been observed by a series of combustion studies, revealing the chemical sequence depicted by Equation 4.2 [172].

$$FeS_2 \rightarrow FeS \rightarrow FeO \rightarrow Fe_3O_4 \rightarrow Fe_2O_3 \quad (4.2)$$

The mineral pyrite (FeS_2) undergoes a transformation into troilite (FeS), followed by oxidation to generate wusite (FeO) [172]. The process of troilite to wusite transformation entails the oxidation of a oxysulfide melt (Fe-S-O) to an iron oxide melt (Fe-O) [172]. The crystallisation of magnetite (Fe_3O_4), or more precisely, $FeO \cdot Fe_2O_3$ occurs following the process of full oxidation of the oxide melt [172]. Under conditions of elevated oxygen concentrations, magnetite undergoes oxidation to form hematite (Fe_2O_3) [172]. No evidence of abnormality (extensive cracking/ fissuring/ zonation) or heat affect was determined in these samples.

4.2 Petrographic properties

The organic microscopic components of coal are divided into three groups: Vitrinite, inertinite and liptinite [100] and will be discussed in Sections 4.2.1. Section 4.2.2 discusses the microlithotype composition focusing on the monomaceral, bimaceral and trimaceral groups.

4.2.1 Maceral content

The vitrinite, inertinite and liptinite content of the coal samples is summarized in Table 18 and indicates a difference in the distribution of the macerals and minerals between the seven samples. The vitrinite, inertinite and liptinite values have been reported in a mineral matter free (mmf) basis, with the mineral matter of each sample listed separately for reference. The samples are dominated by inertinite, followed by vitrinite and liptinite, typical for South African Highveld coals

[12], [43], [157]. The vitrinite content of these 7 samples are low, classifying these coals as low vitrinite coals [55], [101]. Samples E and G have the lowest vitrinite content as well as the highest proportions of observable mineral matter. Gouws *et al*. [12] reported vitrinite values of 23.5 and 10.5 vol % mineral matter free (mmf) basis for the Seam 2 and 4 Highveld coal samples [12]. Roberts *et al.* [98] reported a similar vitrinite content for a Witbank #4 coal sample.

Table 18: Parent coal maceral content

Sample	A	B	C	D	E	F	G
Maceral group analysis (vol %) (mmf)							
Vitrinite	17.7	21.1	27.0	24.1	13.8	22.6	17.2
Inertinite	75.6	75.4	65.5	70.6	80.0	67.1	79.7
Liptinite	6.70	3.50	7.50	5.30	6.20	10.3	3.10
Maceral group analysis (vol %) (including mineral matter)							
Mineral matter	28.6	40.0	35.7	32.0	50.5	41.2	50.7

The liptinite values are within the expected range for Highveld coal when compared to other Highveld coal samples. The liptinite values are within the same range as to the values reported by Gouws *et al*. [12], which is 4.9, 5.1 and 11.5 vol % (mmf). The high mineral matter values can be correlated with the ash yields reported in Table 14. There are some differences between the ash yield. The temperatures involved in preparing ash samples for traditional (proximate) analysis [167], as well as combustion temperatures [108], [173], cause crystallographic and chemical changes in the minerals in coal.

Table 19 contains a summary of the maceral group analysis. The vitrinite values consist mainly of collodetrinite as shown in Table 20. These values are similar to those reported by Roberts *et al*. [98] for a Witbank coal sample. Gouws *et al.* [139] reported a similar Inert Semifusinite content as shown in Table 19. Sporinite dominates the liptinite values, ranging from 1.5 to 5.1 vol%. Roberts *et al.* [98] reported similar sporinite values of 3 and 4 vol% for Witbank and Waterberg coals respectively.

Table 19: Maceral group analysis

Sample		A	B	C	D	E	F	G
Maceral group analysis (vol % including mineral matter)								
Vitrinite	Telinite	0.0	0.2	0.2	0.4	0.2	0.2	0.0
	Collotelinite	4.4	2.9	7.3	4.9	1.9	3.5	2.1
	Vitrodetrinite	0.0	0.0	0.0	0.0	0.0	0.0	0.0
	Collodetrinite	7.6	8.6	9.5	10.1	4.7	9.1	5.8
	Corpogelinite	0.0	0.4	0.0	0.6	0.0	0.4	0.4
	Gelinite	0.6	0.6	0.4	0.2	0.0	0.0	0.2
	Pseudovitrinite	0.0	0.0	0.0	0.2	0.0	0.0	0.0
Inertinite	Fusinite	5.4	2.1	2.6	4.3	1.3	3.0	1.5
	Reactive Semifusinite	1.7	1.5	1.3	2.4	0.4	0.6	0.8
	Inert Semifusinite	30.2	24.3	19.2	27.4	21.2	18.7	22.7
	Micrinite	0.0	0.2	0.2	0.9	0.6	0.0	0.4
	Macrinite	0.0	0.0	0.0	0.4	0.0	0.0	0.0
	Secretinite	0.8	1.0	1.5	0.9	0.2	2.2	0.6
	Fuginite	0.0	0.0	0.0	0.0	0.0	0.0	0.0
	Reactive Inertodetrinite	0.2	0.6	0.7	0.8	0.9	0.2	0.4
	Inert Inertodetrinite	15.7	15.5	16.6	10.9	15.0	14.8	19.9
Liptinite	Sporinite	4.8	2.1	3.3	3.4	2.7	5.1	1.5
	Cutinite	0.0	0.0	0.0	0.0	0.0	0.0	0.0
	Resinite	0.0	0.0	0.2	0.2	0.0	0.2	0.0
	Alginite	0.0	0.0	1.3	0.0	0.4	0.8	0.0
	Liptodetrinite	0.0	0.0	0.0	0.0	0.0	0.0	0.0
	Suberinite	0.0	0.0	0.0	0.0	0.0	0.0	0.0
	Exsudatinite	0.0	0.0	0.0	0.0	0.0	0.0	0.0
Mineral matter	Clay	4.2	4.6	9.1	9.7	9.3	8.5	16.6
	Quartz	15.7	18.2	20.5	11.2	26.9	20.3	21.4
	Pyrite	3.1	11.3	4.1	6.0	11.6	8.9	6.9
	Carbonate	5.4	5.9	2.0	5.1	2.7	3.1	5.2
	Other	0.2	0.0	0.0	0.0	0.0	0.4	0.6

The mineral matter observed in these coal samples are dominated by quartz particles. The main crystalline phase in quartz consists of S_iO_2 and authors have reported S_iO_2 accounting for as high as 95.64 % of the quartz structure [174]. The S_iO_2 content of the coal samples in Table 15 can be related to the amount of quartz seen in the mineral matter content Table 19. The higher mineral matter contents can be indicative of lower reaction rates [139], [140].

4.2.2 Microlithotype composition

The maceral analysis provides information about the maceral and mineral composition of the samples. The microlithotype analysis on the other hand, enables the determination of the maceral and mineral associations. For example, does the vitrinite occur as a monomaceral, or is it intimately associated with semifusinite, or inertodetrinite. The microlithotype data is reported in Table 20.

Table 20: Microlithotype analysis results

Sample	A	B	C	D	E	F	G
Microlithotype analysis (vol % mmf)							
Monomaceral	44.8	33.5	37.8	42.2	30.8	31.1	44.8
Vitrite	11.9	4.7	16.2	14.0	10.0	11.7	10.1
Semifusite	31.6	31.4	21.9	35.1	31.7	25.0	29.9
Fusite / secretinite	3.0	5.1	5.7	3.7	5.4	5.2	6.0
Inertodetrite	10.4	10.9	11.5	5.0	10.0	9.7	9.7
Inert Inertodetrite	10.7	8.8	9.8	7.5	15.8	11.7	13.4
Liptite	0.0	0.4	0.7	0.3	0.0	0.4	0.5
Bimaceral	16.5	16.5	15.5	17.6	9.3	13.5	16.5
Vitrinertite vit+sf/f	7.2	7.3	7.1	5.3	1.8	3.2	4.6
Vitrinertite vit+int	7.5	5.1	4.1	6.8	7.2	4.0	5.5
Clarite vit+lipt	1.5	1.5	1.7	1.9	1.4	1.6	0.5
Durite int+lipt	0.0	16.4	14.2	13.3	11.3	18.6	14.7
Trimaceral	4.8	4.6	4.1	4.6	2.3	4.3	4.8
Duroclarite (V>I, L)	9.0	5.8	4.4	6.5	4.5	6.9	4.6
Clarodurite (I>V, L)	4.8	2.6	2.4	0.6	0.9	1.6	0.5
Vitrinertoliptite (L>I, V)	2.4	0.0	0.3	0.0	0.0	0.4	0.0
Microlithotype analysis (vol % mineral matter)							
Carbominerite	14.4	12.3	17.5	9.8	11.3	16.7	14.4
Rock	19.5	33.1	25.1	25.8	46.3	34.4	19.5
Reactive maceral content (vol % mmf)							
Total reactives	60.6	50.5	57.1	59.4	57.9	56.7	52.8

The samples are dominated my monomacerals; implying that the particles typically contain one maceral (>95% of a single maceral) within a 50 x 50 µm microscopic field of view. The samples are dominated by semifusinite (25 - 31 vol% mmf), followed by inert inertodetrinite or combinations of semifusinite and inertodetrinite, which is characteristic of South African Highveld coals [175].

A comprehensive petrographic investigation and characterisation of coals is necessary to accurately anticipate their combustion and gasification behavior, especially at temperatures below 1100°C [176]. To achieve this objective, it is necessary to identify and quantify all the individual components, such as mono-macerals, bimacerals, tri macerals, and carbominerites [176], [177]. These components can exist in various forms, including reactive and non-reactive macerals and minerals. It is crucial to evaluate the reactivity of even low reflecting inertinites during combustion conditions, as they have been found to be chemically reactive [176], [177]. Additionally, the examination of diverse mineral-maceral interactions, particularly in coals with high mineral matter content, must take into account their composition [178].

Bimaceral durite (combination of inertinite plus liptinite) accounts for 11 – 16 vol% (mmf) for all samples. In terms of char formation, the liptinite is highly reactive and will devolatilize quickly when heated, providing porosity to the inertinite particle [101]. Typically, durite is comprised of inertodetrinite and liptinite, and may include fine clays and quartz grains [91], [101].

The microlithotype data also reflects the trends observed in the maceral data. As shown in Table 20, Sample E has the greatest proportion of rock particles. Samples A and G have the lowest portion of rock, but is not the lowest in terms of carbominerite at 14.4 vol% carbonate-organic associations. Sample C contains the highest carbominerite proportion and Sample D the lowest. Everson *et al*. [48] reported a carbominerite composition of 30 % for a high ash coal from South Africa. Carbominerite compositions ranging from 15 – 20 vol % (mineral matter basis) have been reported for South African Highveld coal samples [179]. These values are within the same range as the carbominerite compositions reported in Table 20.

In terms of total reactive maceral content (vitrinite, liptinite and reactive inertinite), Sample A has the greatest proportion of reactive macerals, and Sample B contains the lowest proportion. Henning *et al*. [157] investigated coals from the same seams as Gouws *et al*. [12] and reported similar maceral compositions with total reactive macerals ranging from 68.8 to 71.5 vol%. Gouws [12] investigated three South African Highveld and reported a higher total reactive macerals content in the range of 80 to 85 vol % (mmf).

Du Toit *et al*. [48] and Mgano *et al*. [43] reported lower reactive maceral contents of 47 and 45.6 vol % respectively. Du Toit *et al*. [48] and Mgano *et al.* [43] investigated typical Highveld coal samples reporting similar maceral compositions. Roberts et al [98] reported a reactive maceral content of 34 vol % for a Witbank coal sample, which is significantly lower. According to Table 20,

the reaction rates are expected to be higher than those of the coal samples examined by the other authors due to the increased total reactive maceral content.

4.3 Char morphology

The char morphology analysis indicates some differences between the chars in terms of their conversion behaviour at 900 °C and 30 bar as shown in Table 21. All samples are dominated by mixed dense (16 – 37 vol% mmf) and inertoid / dense particles (22 – 36 vol% mmf). There are more unreacted minerals compared to partially reacted minerals, and no amorphous or neoformed minerals were determined. The absence of amorphous or neoformed minerals suggests a lack of high-temperature alteration indicating that the reaction temperature falls below the melting point of the minerals [180].

Table 21: Char morphology results

Sample	A	B	C	D	E	F	G
Char morphology (vol % mmf)							
Honeycomb thin	3.1	0.9	1.8	2.1	1.3	0.3	3.5
Honeycomb thick	7.2	2.1	4.2	7.7	2.6	2.7	4.1
Mixed porous	37.8	21.8	26.6	17.4	13.4	10.3	34.7
Mixed dense	18.1	37.3	16.4	25.6	23.3	29.5	26.2
Inertoid/dense	22.7	25.2	36.7	29.0	32.3	34.8	22.4
Fusinoid	2.2	2.1	5.2	2.4	3.0	5.3	4.1
Oxidised/cracked	8.9	10.6	9.1	15.8	24.1	17.1	5.0
Consumed	0.0	0.0	0.0	0.0	0.0	0.0	0.0
Cenospheres	0.0	0.0	0.0	0.0	0.0	0.0	0.0
Coal	0.0	0.0	0.0	0.0	0.0	0.0	0.0
Char morphology (vol % mineral matter)							
Unreacted minerals	8.1	13.0	23.3	10.2	34.5	18.7	21.1
Carbominerite 20-60	8.9	11.1	10.8	11.0	9.6	12.0	10.2
Partially reacted minerals >60%	1.0	5.9	8.8	1.8	9.6	3.5	2.7

From Table 21, the porous honeycomb (thin and thick) particles account for 11 vol% or less and no cenospheres were determined, which is expected due to the maceral composition and size of charred particles. [181]The small proportion of honeycomb indicates that the chars did not develop extensive porosity during pyrolysis. Samples A and D had the highest proportion of honeycomb chars, while Samples B, E and F contain the lowest percentages.

Samples A and G contain more porous (honeycomb + mixed porous) particles than the other samples. However, there does not appear to be a correlation between the proportion of porous chars and reactive maceral composition as indicated in Figure 18. From the first plot in Figure 18, (Honeycomb + mixed porous) contains the honeycomb thin, honeycomb thick and mixed porous components as summarized in Table 21. A second plot (Honeycomb + mixed porous + mixed dense) includes the mixed dense components. The results confirm the complexity in char conversion. The R^2 values indicate that the data is not a good fit, but it did increase with the added mixed dense data as indicated by the orange plots in Figure 18.

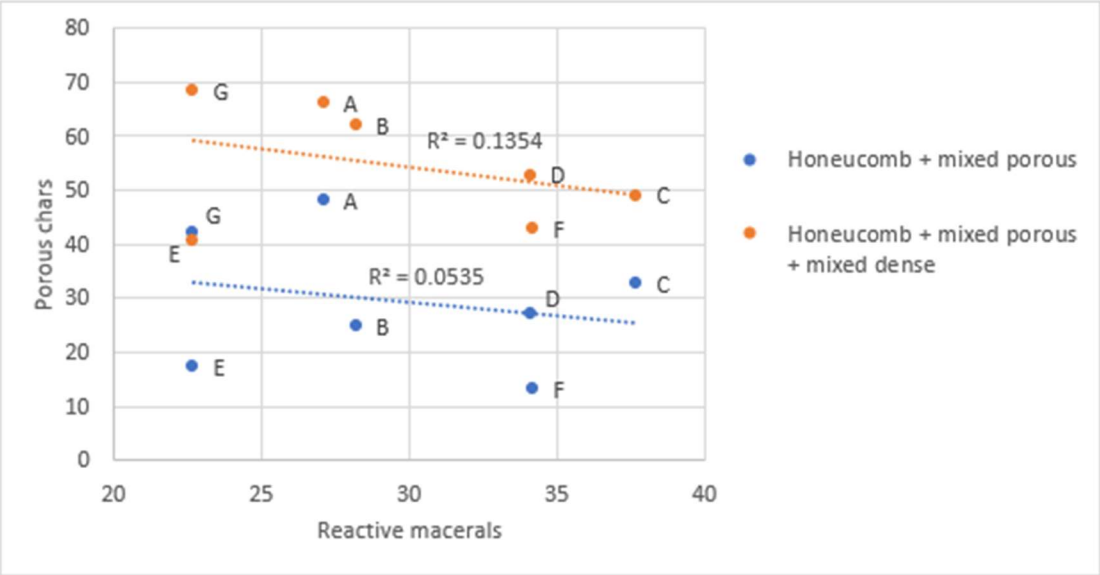

Figure 18: Reactive Macerals and Porous Char (vol% mmf)

Cracking during conversion is related to the particle's response to heat and the release of water vapor and other volatile gases [182]. From the maceral analysis (Done at the University of Johannesburg) there does not appear to be an obvious relationship between cracking and maceral type, as most particles are dominated by inertinite. Sample E has the highest proportion of cracked particles (24.1 vol% mmf), and G the least (5 vol% mmf). The maceral and microlithotype data indicate that these samples are almost identical, so it is uncertain why the char morphology differs so much.

There were no discernible zonation or transitional regions found after careful examination of both the particle margins and the particle as a whole. This intriguing observation implies that the entire particle reacts at the same time, with no distinct areas reacting at different times. In other words, there is a lack of evidence supporting the presence of a shrinking core model.

The lack of zonation or transitional regions suggests that the reaction process is uniform and homogeneous throughout the particle. This discovery calls into question the traditional notion of localized reactions within particles, in which a core region reacts first and the outer layers gradually join in. Instead, the reaction appears to take place uniformly across the entire particle, indicating that the reaction is taking place in the chemically controlled regeim.

Figure 19 provides illustrative examples that visually depict the absence of zonation or transitions within the particles to support this observation. These images serve as empirical evidence that supports the concept of whole-particle reaction. This discovery has implications for the understanding of particle reactivity, as well as for other fields such as materials science, chemistry, and catalysis. More research into the underlying mechanisms and factors influencing this simultaneous reaction behaviour is needed to shed light on this phenomenon and its potential applications.

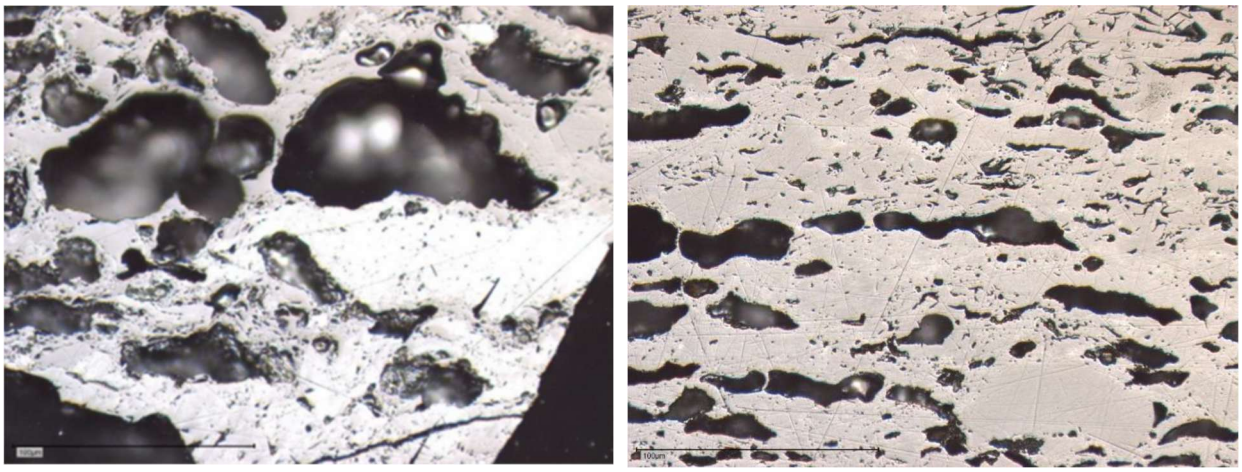

Figure 19: ISI and MSH mixed porous char particles; no evidence of zoning or transitional char formation.

Table 21 summarizes the study's char morphology results, which also include mineral matter. The table shows that sample E has the highest proportion of unreacted minerals when compared to the other samples. Sample E has previously been identified and concluded to be an outlier in terms of mineral content, implying that it differs significantly from the other samples in the study.

Furthermore, the table shows that carbominerites, a subset of char morphology, exhibit relatively consistent characteristics across samples. Samples A and E, in particular, are located at the lower end of the range within this group, indicating a similarity in carbominerite composition. The specific

properties or features that define this carbominerite range may vary depending on the study and characterization methods employed.

4.4 Surface area analysis

The micro and mesopore surface areas are summarized in Table 22.

Table 22: Micro- and mesopore surface areas

Parameter	Method/ technique	A		B		C		D	
		(db)	*(daf)*	*(db)*	*(daf)*	*(db)*	*(daf)*	*(db)*	*(daf)*
Micropore SA (m^2/g)	D-A method	240	310	256	355	217	330	274	369
Mesopore SA (m^2/g)	BET-method	1.33	1.72	6.40	8.87	2.16	3.28	11.3	15.2
Parameter	**Method/ technique**	**E**		**F**		**G**			
		(db)	*(daf)*	*(db)*	*(daf)*	*(db)*	*(daf)*		
Micropore SA (m^2/g)	D-A method	210	355	201	292	221	365		
Mesopore SA (m^2/g)	BET-method	12.3	20.9	27.3	39.7	0.60	1.00		

The micropore surface areas determined using the D-A method is within the expected range for unreacted Highveld coal chars [12], [43]. Miocropore surface areas of 211 to 284 m^2/g (mmf) have been reported for South African coals [12]. Mgano *et al*. [43] reported a similar micropore surface (249 m^2/g *daf*) area for a South African Highveld coal using the D-A method. The micropore surface area reported for Sample F is the closest to the micropore surface areas reported by Mgano *et al*. [43]. Gouws *et al*. [12] reported micropore surface areas ranging from 211 to 284 m^2/g (mmf).

The differences between the mesopore surface areas are however significantly larger when compared. Samples A and G have the smallest mesopore surface areas. Sample E on the other hand, has the largest mesopore surface area and also the smallest micropore surface area. The mesopores provide passage for the reactant gases to reach the active carbon sites within the micropores for gasification to take place [183]. Gouws *et al.* [12] reported mesopore surface areas similar to those of samples in Table 20 ranging from 14.4 to 18.2 m^2/g at 9 bar. The mesopore

surface area of Sample F is however an outlier when compared to the other samples and the results reported by Gouws *et al*. [12].

The higher pore volume allows for increased accessibility for the reactant gas, resulting in increased reactivity [12], [43], [131]. Previous studies have reported that there is a significant decrease in surface area in the later stages of conversion [96]. The decrease in surface area can be attributed to the mineral matter melting point of the coals being below the operating temperature [96]. Tremel and Spliethoff [96] found that an increase in pyrolysis temperature resulted in a decrease in observed reactivity. The pyrolysis temperature was increased from 1200 to 1600 °C and the observed reaction rate decreased from 3.8 to 1 (dm/dt·m)[$10^{-4}s^{-1}$] [96]. The melting mineral matter likely blocked the micropore structure, due to the operating temperatures being higher than the ash fusion temperature. The surface area of the coal after pyrolysis is important as this is the starting point for char conversion [96].

Chapter 5: Results and discussion

The results of the coal gasification reactivity experiments are discussed in Section 5.1. The reactivities of the seven coal char samples are compared to each other and to the literature. The results show that the coal char samples exhibited varying reactivity levels. The comparison to the literature also highlighted the importance of understanding the specific characteristics of each coal sample in predicting its reactivity.

Section 5.2 discusses the correlations between reactivity and coal properties. Looking at the connections between proximate analysis, ultimate analysis. CaO, Si/Al ratio, alkali index, maceral composition, and reactivity in more detail. These correlations reveal the relationship between coal and coal properties. These correlations provide valuable insights into the factors that contribute to the combustion characteristics of coal and can inform strategies for optimising combustion processes in industrial applications.

Section 5.3 discusses the difference in predicted reactivity and experimental reactivity of the coal sources. Tukey Honest Significant Differences (HSD) tests were also performed to assess the difference between the coal samples.

Section 5.4 contains a summary of the findings from the statistical model and its comparison with the experimental reactivities.

5.1 Coal char gasification reactivity.

The experimental specific reaction rates obtained for all the coal char samples will be discussed in this section. The specific reaction rates were determined using the experimental procedures and methods discussed in Section 3.5.

Figure 20 shows the specific reaction rates at 730 °C and 30 bar for the seven coal chars. When observing the general trends of the specific reaction rates depicted in Figure 20, Sample A has the highest reaction rate at 730 °C. Sample E had the lowest recorded reactivity throughout when compared to the other samples. The reactivities showed a constant increase with conversion for most of the samples. Samples F and E however, showed a constant increase up to 11 % conversion, followed by a decrease in reactivity. Mgano *et al*. [43] observed similar trends, showing a general increase in reactivity followed by the stabilization of the reaction rates around

16 % conversion. Gouws *et al*. [12] reported a constant increase in reactivity up to 20 % conversion.

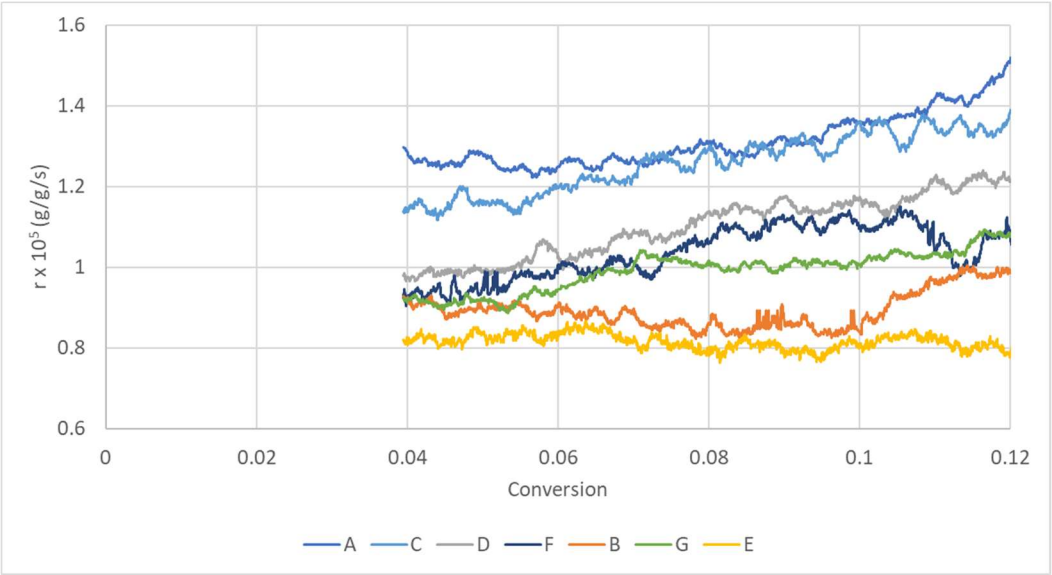

Figure 20: Coal char reactivity of all samples at 730 °C and 30 bar

Figure 21 shows the reaction rates of the seven coal chars at 740 °C and 30 bar. The reactivities of the char samples showed a steady increase with conversion at 740 °C. At 740 °C, Sample A showed the highest reaction rate while Sample G showed the lowest specific reaction rate. Samples A, C, D, E and G all showed a general increase in reactivity with an increase in conversion. Samples D, E and F show similar reaction rates with conversion. The reaction rates increased with an increase in temperature (730 °C to 740 °C). An average increase in reaction rate of 0.33 g/g/s has been observed at 8 % conversion.

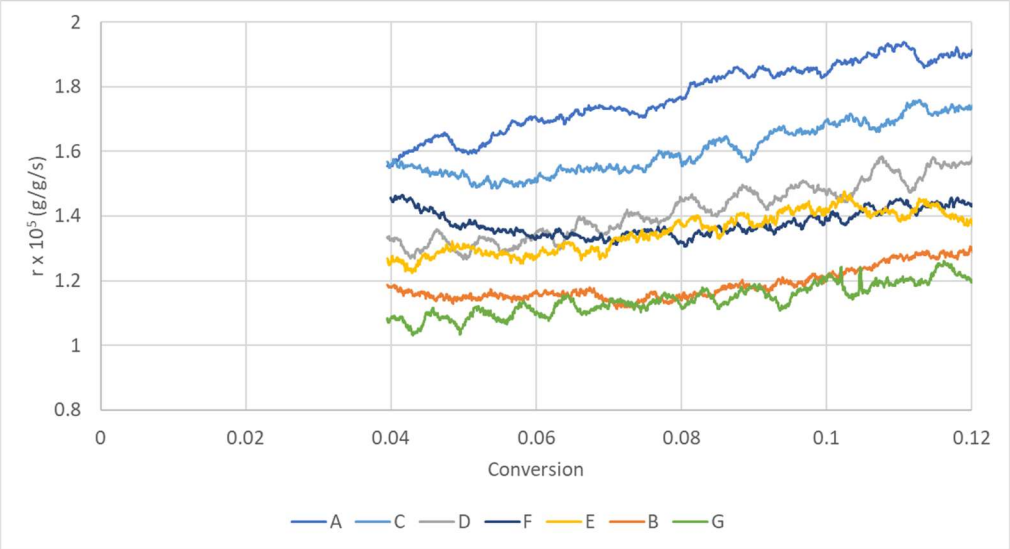

Figure 21: Coal char reactivity of all samples at 740 °C and 30 bar

Figure 22 illustrates the specific reaction rates of all the coal chars at 750 °C and 30 bar with conversion. The specific reaction rates showed an increase with an increase in carbon conversion, except for Samples E and F. Sample F showed a decrease, while Sample E remained constant with an increase in carbon conversion. At 750 °C, Sample A showed the highest specific rate and Sample G the lowest reaction rate with conversion. The reaction rates exhibit a greater increase in the average reaction rate (seven samples) when the temperature rises from 730 °C to 740 °C (at 8 % conversion; $r_{average,730°C} = 1.01 \times 10^5$ to $r_{average,740°C} = 1.44 \times 10^5$), as opposed to the increase found when the temperature rises from 740 °C to 750 °C (at 8 % conversion; $r_{average,740°C} = 1.44 \times 10^5$ to $r_{average,750°C} = 1.83 \times 10^5$). At the higher temperature, the specific reaction rate trends more closely represent the trends reported by Gouws *et al*. [12]. They observed a consistent increase in reactivity, subsequently moving towards a state of stability.

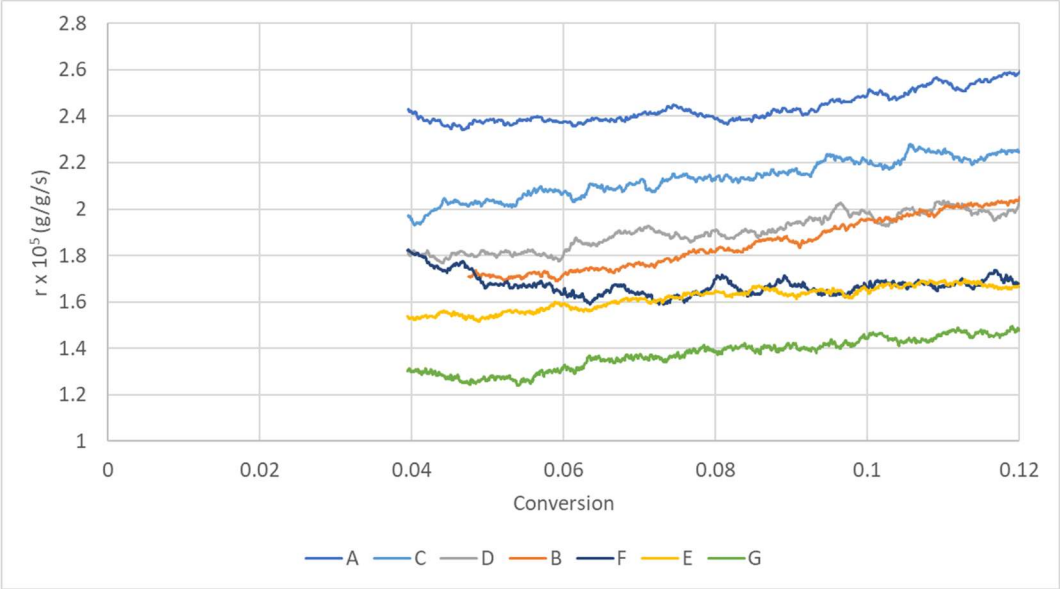

Figure 22: Coal char reactivity of all samples at 750 °C and 30 bar

Table 23 contains a summary of all the specific reactivities of the coal chars at the three different temperatures and 8 % conversion. Sample A and E had the lowest reaction rate at 730 °C, but showed a significant increase in reaction rate when compared to the other samples at 740 and 750 °C. Sample F initially has a higher reaction rate compared to that of Sample E, but becomes similar around 7 % conversion. When considering the reaction rates from 7 % conversion, Samples E and F have similar reaction rates at 750 °C as shown in Figure 22.

Table 23: Specific reactivities at different temperatures

Sample	r x 10^5 (g/g/s)			E_a (kJ/mol)
	730 °C	740 °C	750 °C	
A	0.87	1.41	1.65	248 ± 25
B	0.88	1.21	1.80	307 ± 36
C	1.10	1.39	1.66	176 ± 27
D	1.36	1.83	2.43	195 ± 30
E	0.87	1.41	1.65	273 ± 38
F	1.00	1.19	1.42	149 ± 32
G	1.24	1.58	2.10	224 ± 36

A general observation can be drawn from Table 23, i.e., the fact that Sample D always had the highest reaction rate followed by Sample G. These two samples also had some of the highest

estimated activation energies due to the increase in reaction rates observed with an increase in temperature.

Lee *et al*. [128] found that chars produced from bituminous coals of the ASTM ranks can display significant differences in reactivities. By comparing coal samples obtained from the same region will provide the best basis for this study. The CO_2 gasification studies that are available for South African Highveld coal have all been conducted using a CO_2 and N_2 mixture as reactant feed [12], [43], [157]. There is a significant increase in reaction rate up to higher CO_2 partial pressures of around 10 bar, after which only a small increase in reaction rate is observed [12], [43], [96], [157].

Gouws *et al*. [12] reported a reaction rates of 9.1 x 10^6 g/g/s at 780 °C for the 5N char at 10 % conversion. to 5.51 x 10^5 g/g/s at 855 °C for South African Highveld coals. These experiments were conducted at 30 bar using a reactant feed consisting of 30 % CO_2 and the balance N_2. Mgano *et al*. [43] conducted experiments at the 30 bar and a reactant concentration of 50 % CO_2. He reported a reaction rate of 1.25 x 10^5 g/g/s at 10 % conversion and 780 °C. Henning *et al*. [157] conducted gasification experiments on five coal chars at 900 °C and 20 bar and reported specific reaction rates ranging from 2.2 x 10^4 to 3.9 x 10^4 g/g/s. The results of these studies confirm the typical reaction rates of South African Highveld coals.

The inherent reactivity of the Highveld char from seam 4, as utilised by du Toit *et al*. [48], is nearly indistinguishable from the reactivity of the 4N char investigated by Gouws *et al*. [12]. This outcome is anticipated because both of these chars were derived from seam 4 Highveld coals and subjected to devolatilization at an identical temperature of 950°C. When the partial pressure is increased to a level over 2 bar, the estimated reactivity of the char utilised by du Toit et al. [48] is lower than the reactivity of 4N [12]. Gouws *et al*. [12] attributed the difference in reactivity due to variations in the total quantity of active sites.

Roberts and Harris [40] reported a reaction rate of 1.6 x 10^5 g/g/s at 10 % conversion for an Australian coal char (15.2 bar and 900 °C). The inherent reactivity of char D exhibited the highest level among all samples, which can be attributed to its elevated volatile content [40]. The intrinsic reactivity of both chars were comparable to the reactivity of the chars used in this study [116]. This could be attributed to the resemblance in the properties of the coals and the ensuing chars. The NL char exhibited a relatively high mineral matter content of 21 % on a dry basis and a high inertinite content of 58 % on a mineral matter-free basis [116], which is comparable to the chars utilised in this investigation.

Figure 23 shows the Arrhenius plot of the specific reaction rates at 730, 740 and 750 °C as well as the trendline of the data points. The activation energies in Table 23 are calculated using the equations presented in the figure. All the trendlines fit relatively well with the data points, accept for Samples B and E. For Samples B and E, the specific reaction rates at 740 °C are outliers. Figure 23 clearly indicates that Samples A and C have the highest reaction rates and that there are large differences between the reaction rates of the coal char samples.

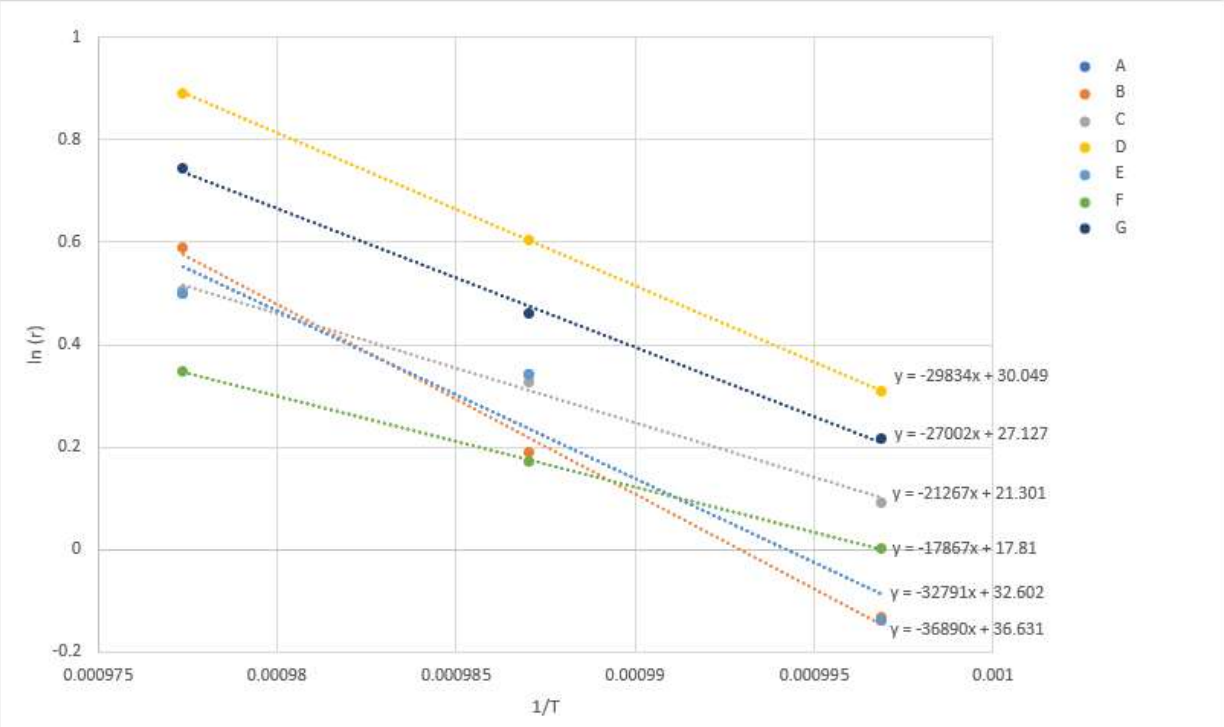

Figure 23: Arrhenius plot – Activation Energy calculation

The activation energies align closely with the values documented in the literature for comparable coal chars. Kajitani *et al.* [44] found activation energies ranging from 222 to 251 kJ/mol for the gasification of a bituminous coal char at CO_2 partial pressures up to 7 bar, using the LH model. Du Toit *et al*. [48] employed the Langmuir Hinshelwood (LH) equation to interpret the reactivity of a Highveld Seam 4 char when subjected to CO_2 gasification at atmospheric pressure. The activation energy was determined using Arrhenius plots. The reported values include an activation energy of 243 ± 32 kJ/mol. Zhang et al. [184] employed the LH model to characterise the reactivity of a bituminous coal char at low pressure conditions (2 to 5 bar) during CO_2 gasification. They observed activation energies within the range of 131 to 280 kJ/mol. Gouws *et al.* [16] reported

activation energies of 268 kJ/mol, 218 kJ/mol and 211 kJ/mol for the 2N, 4N and 5N coal samples respectively.

5.2 Relationship between variables

Section 5.2.1 explores the correlation among reactivity, proximal analysis, and temperature. The results of the association between ultimate analysis and reactivity is discussed in Section 5.2.2. An examination of the correlation between reactivity and macerals is discussed in Section 5.2.3. The correlation between the level of reactivity and the physical structure of char is examined in section 5.2.4. The correlation between reactivity and the parameters of coal ash, including CaO, CaO x Ash yield, Si/Al, and alkali index, is examined in Section 5.2.5, 5.2.6, 5.2.7 and 0. Section 5.3 discusses the variation in reactivity among different coal sources, followed by Section 5.4 which contains a summary of the results obtained in Section 5.2.

5.2.1 Relationship between coal reactivity and proximate analysis.

A regression model was fitted for reactivity as a function of temperature and proximate analysis using the reactivity data for the different sources as depicted in Figure 24. The model has a R^2 = 0.78 and standard error equal to 0.186 x 10^{-5} g/g/s or 13 %. Temperature and proximate analysis have significant effects on the reactivity. The reactivities were correlated using the regression model as discussed in Section 3.7. The coefficients obtained from the model fitted to the data are listed in Table 24. The estimated coefficients can now be used to obtain the predicted reactivity for any combination of values of the components and temperature in the model. The parity plot indicates that the model fits the data well and can be used to interpret the effect of the variables on reactivity and for the prediction of reactivity.

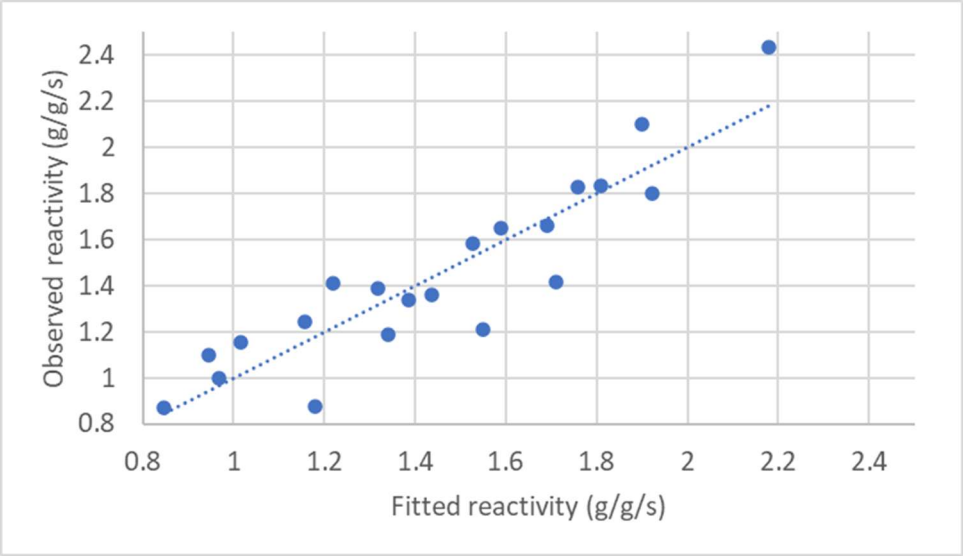

Figure 24: Observed versus predicted Reactivity as a function of proximate analysis.

The proximate analysis coefficients determined are summarized in Table 24 using least squares minimization. The p-value is the probability that the effect of the variable on reactivity is only by chance and the smaller the value, the more significant is the effect. For example, the volatile matter p-value is equal to 0.039, which indicates that the variable is significant on a 3.9 % level i.e. there is a 96.1 % confidence that the variable has a true effect on reactivity. Usually, a p-value smaller than 0.05 is used as a reference for statistical significance.

Note the proximate analysis is a composition, and therefore the coefficients should not be directly interpreted. However, the effect of temperature on reactivity, which is an independent variable, can be assessed from the estimated coefficient. Specifically, for every 1 °C increase in temperature, the reactivity increases by 0.037 x 10^{-5} g/g/s on average for the proximate analysis.

Table 24: Proximate analysis coefficients and errors

Variables	Coefficients	Standard error	P value
Temperature	0.037	0.005	$1.27 \cdot 10^{-06}$
Inherent moisture	- 0.545	0.104	$8.49 \cdot 10^{-05}$
Ash yield	- 0.286	0.037	$9.36 \cdot 10^{-07}$
Volatile matter	- 0.180	0.080	$3.90 \cdot 10^{-02}$
Fixed carbon	- 0.255	0.049	$8.90 \cdot 10^{-05}$

The trace plot is generated for the interpretation of the effects of the components on reactivity. The trace plot is depicted in Figure 25 for 740 °C, as this is the average temperature used in this study. The trace plot depicts the predicted reactivity as a function of the change of the component from its centre point to its minimum and maximum value, while the other components are kept constant at a fixed ratio to each other. For example, from Figure 25, it is observed that the x-axis ranges from -9 to 9.5 in ash yield units to accommodate the change in ash yield from its minimum to its maximum value. Therefore, given an average ash yield of 31%, the range on the x-axis goes from 22% to 40% ash yield. Note the ranges of the components are different. The trace is constructed in such a way such that the centre point of each component is equal to zero, and the x-axis depicts the deviation from the centre point for each component, simplifying the interpretation of the relationships between the reactivity and the components.

From Figure 25, it can be observed that reactivity has a positive correlation with volatile matter and fixed carbon. Several authors have reported that coal char reactivity is directly proportional to volatile mater content [93], [185], [186], and that there is an increase in reactivity with an increase in volatile matter.

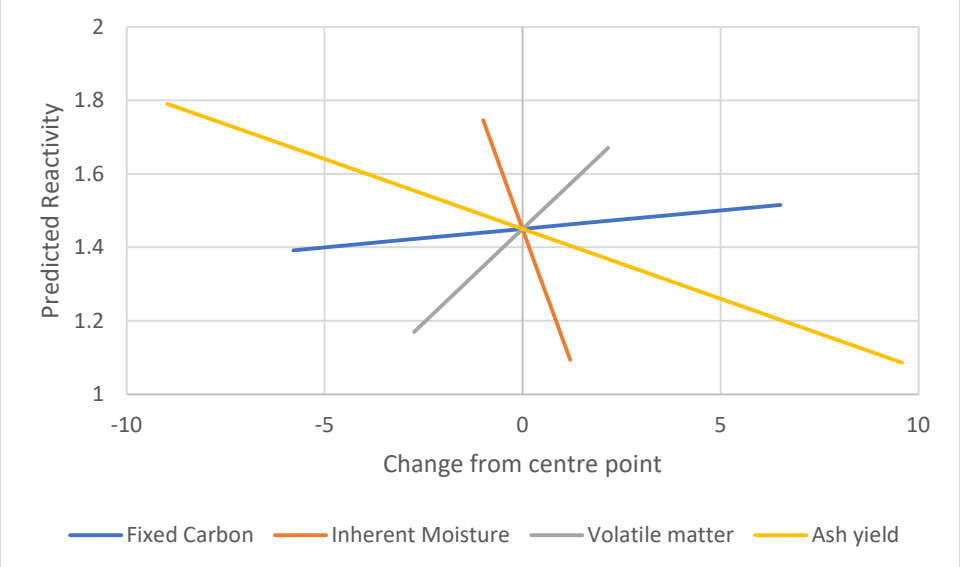

Figure 25: Sensitivity analysis plot of predicted reactivity as a function of the changes in the proximate analysis

Casal *et al*. [171] found that there is an increase in reactivity with an increase in volatile matter due to the lower activation energies [16], [47], [171]. From the trace plot, volatile matter seems to have the largest positive effect on reactivity as indicated by the steep slope. Several authors have

confirmed a positive relation between carbon content and reactivity [2], [16], [47].A similar positive relation between reactivity and fixed carbon is observed although less pronounced.

5.2.2 Relationship between reactivity and ultimate analysis of coal

A regression model was fitted for reactivity as a function of temperature and ultimate analysis using the measured gasification reactivities of the different sources. Figure 26 shows a plot of the experimental observed reactivities and the predicted reactivity as a function of the ultimate analysis and temperature. The parity plot indicates that the model fits the data well and can be used to interpret the effect of the variables on reactivity and for the prediction of reactivity.

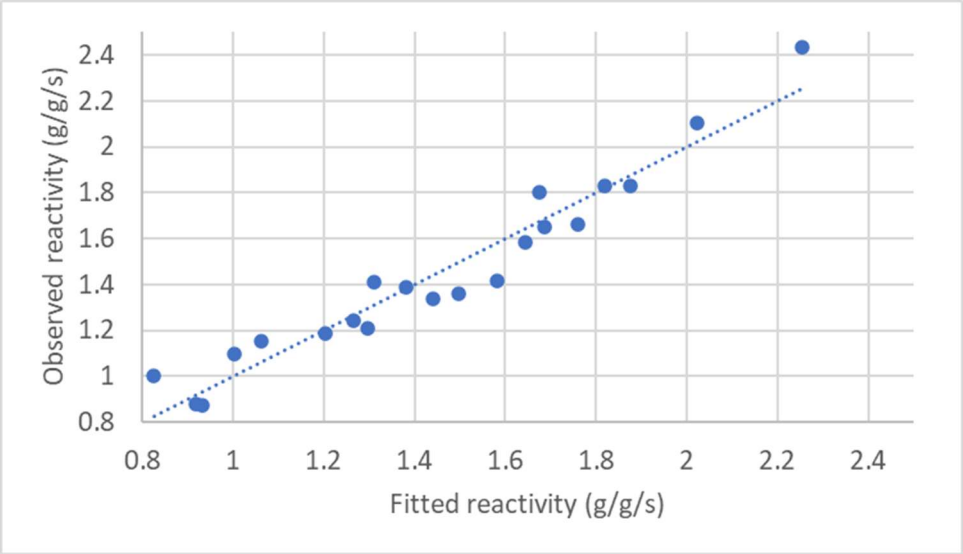

Figure 26: Observed versus predicted reactivity as a function of ultimate analysis.

The coefficients in Table 25 were used to determine the reactivities as discussed in Section 3.7.2. The model has a R^2 = 0.90 and standard error equal to 0.124 or 8.55 %. Temperature and ultimate analysis have significant effects on the reactivity.

The coefficients of the regression model determined are summarized in Table 25. The p-value is the probability that the effect of the variable on reactivity is only by chance and the smaller the value, the more significant is the effect. For example, the carbon p-value is equal to 3.72 x 10^{-5}, which indicates that the variable is significant on a 0.0037 % level i.e., there is a 99.99 % confidence that the variable has a true effect on reactivity. According to the p-values listed, the ash yield has the largest effect and nitrogen has the smallest effect on reactivity.

The reactivities were correlated using the model as discussed in Section 3.7.2. The coefficients listed in Table 25 can be used to obtain the predicted value of reactivity for any combination of values of the components and temperature in the model. The effect of each variable and component on reactivity can only be interpreted through the trace plots.

Table 25: Ultimate analysis coefficients and errors

Variables	Coefficients	Standard error	P value
Temperature	0.038	0.003	$3.90 \cdot 10^{-08}$
Inherent moisture	- 0.484	0.122	$1.56 \cdot 10^{-03}$
Ash yield	- 0.280	0.026	$7.95 \cdot 10^{-08}$
Carbon	- 0.318	0.052	$3.72 \cdot 10^{-05}$
Hydrogen	0.707	0.049	$1.02 \cdot 10^{-01}$
Nitrogen	0.738	0.836	$3.94 \cdot 10^{-01}$
Oxygen	- 0.200	0.104	$7.76 \cdot 10^{-02}$
Sulphur	- 0.435	0.132	$5.79 \cdot 10^{-03}$

The trace plot depicted in Figure 27 is generated for the interpretation of the effects of the variables listed in Table 25 on reactivity. The trace plot depicts the predicted reactivity as a function of the change of the component from its centre point to its minimum and maximum value, while the other components are kept constant at a fixed ratio to each other. For example, from Figure 27, it is observed that the carbon ranges from -7.5 to 8 wt % carbon to accommodate the change in carbon content from its minimum to its maximum value. From Figure 27, ash yield and carbon content show the largest changes from the centre point. This indicates large variations in carbon content and ash yield between the coal samples.

Figure 27, reactivity shows a positive correlation with hydrogen, oxygen and carbon content. Niksa [172] conducted an investigation on the prediction of the devolatilization behaviour of coal based on its ultimate analysis. She determined that the rates of oxygen and hydrogen are optimal for the selectivity coefficient between separation and condensation into char links. This is because oxygen encourages the formation of crosslinks, while the addition of hydrogen to broken bridge fragments stabilises them. Oxygen facilitates the process of crosslinking, while hydrogen atoms hinder it by stabilising big polynuclear free radicals [172].

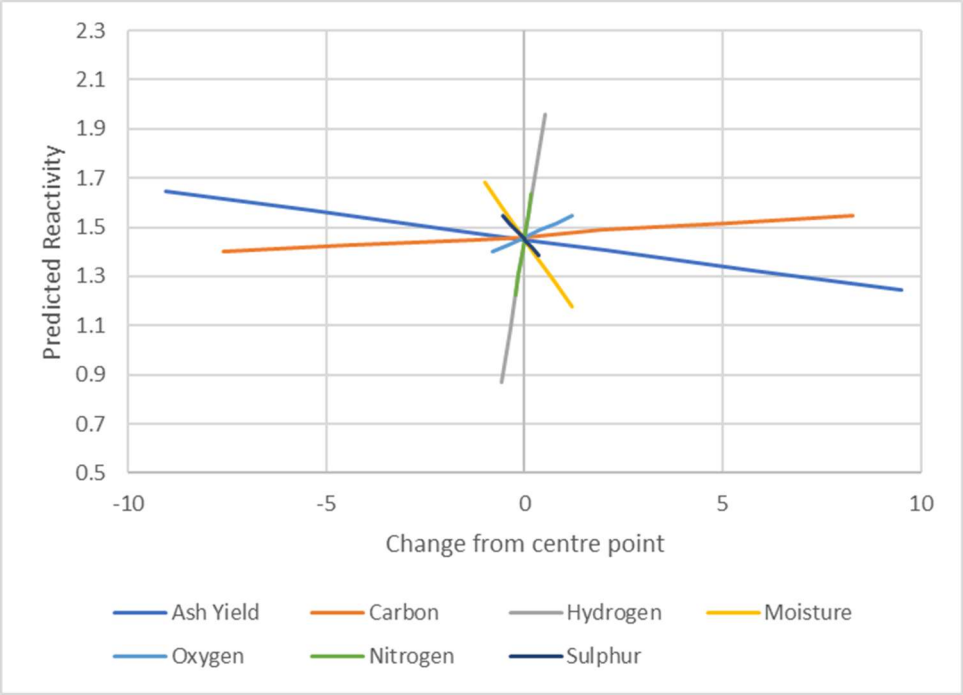

Figure 27: Sensitivity analysis plot of predicted reactivity as a function of the changes in ultimate analysis.

Sun *et al*. [99] observed that inertinite had a significant reactivity towards hydrogen under elevated temperatures, resulting in higher reactivities. Coals that have a high hydrogen content contain a significant amount of vitrinite and exinite [173]. Keboletse *et al.* [173] concluded that an increase in hydrogen content leads to an increase in reactivity.

During coal combustion, oxygen reacts with carbon to produce CO_2 and heat [44], resulting in the positive slopes observed in Figure 27 between reactivity and carbon/ oxygen content. Higher oxygen content results in higher reaction rates and more heat due to the reaction between oxygen and carbon [44]. Steam gasification uses oxygen as a catalyst to promote chemical reactions between coal and other reactants like steam or water [47], [61]. Oxygen speeds up coal reaction by breaking down complicated hydrocarbon structures [44].

A significant decrease in reactivity is observed with an increase in Sulphur and Moisture content. During combustion, sulphur in coal oxidizes to form sulphur dioxide (SO2) and this process consumes oxygen and competes with the combustion of carbon, thereby reducing the overall combustion efficiency [174]. As a result, coal with higher sulphur content tends to exhibit lower combustion reactivity and may require additional air or oxygen for complete combustion [174]. The presence of moisture in coal has an adverse impact on its higher heating value (HHV), a

metric used to quantify the energy content per unit mass [175]. Moisture reduces the effective energy content by absorbing heat during combustion [175]. Ashes and moisture-rich coal are indicative of inferior quality coal.

5.2.3 Relationship between reactivity and Maceral group analysis

- **Excluding minerals**

A regression model was fitted for reactivity as a function of temperature and the maceral group analysis excluding the minerals using the coefficients in Table 28 and the reactivity data for the different sources as depicted in Figure 28. The model has a R^2 = 0.63 and standard error equal to 0.244 x 10^{-5} g/g/s or 16.83 %.

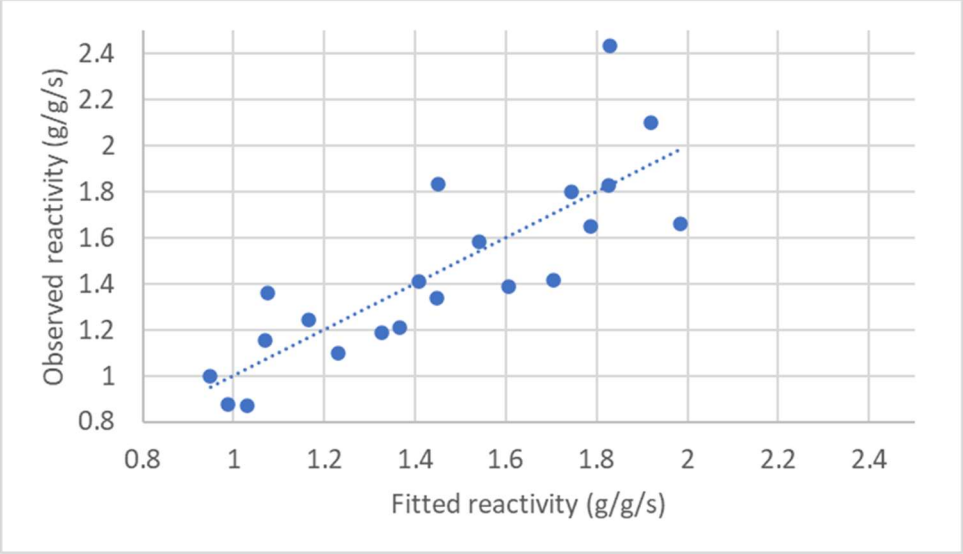

Figure 28: Observed versus predicted reactivity as a function of temperature and maceral group (mmf).

From the p-values it can be noted that temperature and all three maceral components have significant effects on the reactivity. The vitrinite and inertinite components have the largest effects on reactivity. The trace plot is depicted in Figure 29 for an average temperature.

Table 26: Maceral coefficients and standard errors (mmf).

Variables	Coefficients	Standard error	P value
Temperature	0.038	0.007	$2.17 \cdot 10^{-5}$
Vitrinite	- 0.262	0.050	$6.12 \cdot 10^{-5}$
Inertinite	- 0.268	0.048	$3.50 \cdot 10^{-5}$
Liptinite	- 0.235	0.054	$4.37 \cdot 10^{-4}$

The trace plot depicts the predicted reactivity as a function of the change of the component from its centre point to its minimum and maximum value, while the other components are kept constant at a fixed ratio to each other. From Figure 29, it is observed that the x-axis ranges from about -9 to 9 to accommodate the change in the components. Reactivity increases with an increase in liptinite content and decreases with an increase in inertinite content.

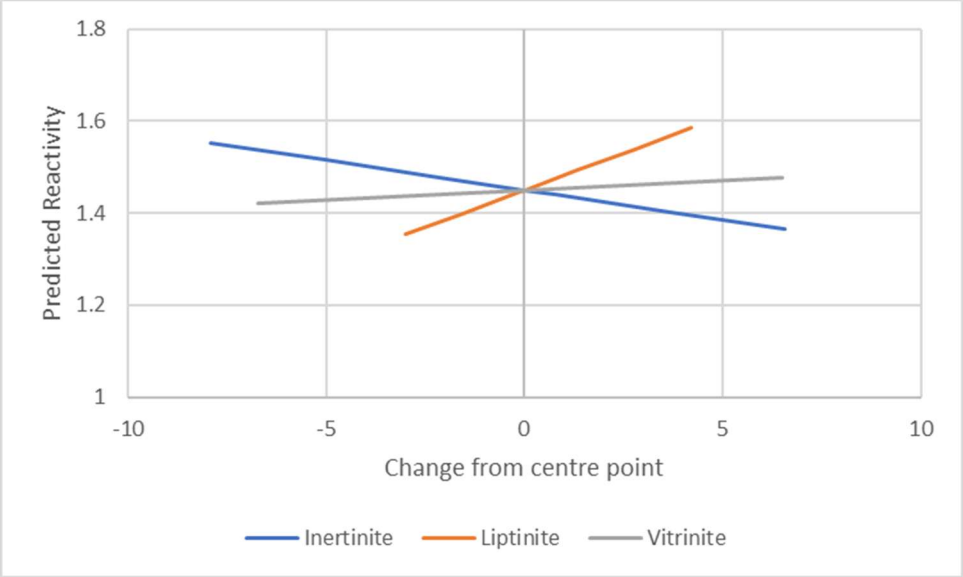

Figure 29: Sensitivity analysis plot of predicted reactivity as a function of the changes in the maceral group components excluding minerals.

Vitrinite shows a slight positive effect on reactivity. Liptinite shows a much larger positive effect on reactivity. Inertinite showed a negative effect on reactivity. Inertinite rich coal normally has a low reactivity [22], as confirmed by the negative effect shown in Figure 29. The inhibiting effect of inertinite is due to the presence of dense chars, specifically inert Inertodetrite [1]. Several studies have confirmed that liptinite is the most reactive maceral [23], [47], [102]

5.2.4 Relationship between reactivity and Char Morphology analysis excluding mineral matter

A regression model was fitted for reactivity as a function of temperature and the morphology analysis excluding minerals, using all the data for the different sources as depicted in Figure 30. The model has a R^2 = 0.90 and standard error equal to 0.124 x 10^{-5} g/g/s or 8.55 %.

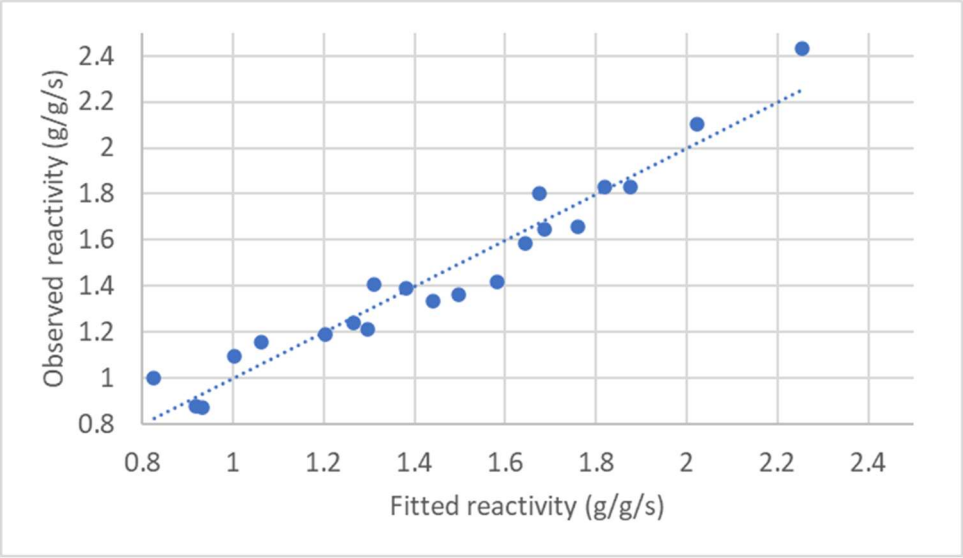

Figure 30: Observed versus predicted reactivity as a function of temperature and char morphology (mmf).

The coefficients determined for the char morphology analysis properties excluding mineral matter is summarized in Table 27. The properties listed have significant effects on reactivity.

Table 27: Char morphology coefficients and standard errors (mmf).

Variables	Coefficients	Standard error	P value
Temperature	0.038	0.003	$3.90 \cdot 10^{-8}$
Honeycomb thin	- 0.916	0.138	$1.67 \cdot 10^{-5}$
Honeycomb thick	- 0.389	0.048	$2.14 \cdot 10^{-6}$
Mixed porous	- 0.202	0.028	$6.77 \cdot 10^{-6}$
Mixed dense	- 0.212	0.029	$5.87 \cdot 10^{-6}$
Inertoid dense	- 0.153	0.031	$2.91 \cdot 10^{-4}$
Fusinoid	- 0.999	0.146	$1.21 \cdot 10^{-5}$
Oxidized cracked	- 0.366	0.031	$2.19 \cdot 10^{-8}$

The trace plot is depicted in Figure 31 for an average temperature of 740 °C. The trace plot depicts the predicted reactivity as a function of the change of the component from its centre point to its minimum and maximum value, while the other components are kept constant at a fixed ratio to each other. From Figure 31, it is observed that the x-axis ranges from about -16 to 16 to accommodate the change in the components. Reactivity increases with an increase in inertoid, mixed porous and mixed dense content, and decreases with an increase in honeycomb content.

Energy (J/mol) has a positive correlation with the mixed dense results. Honeycomb results are negatively correlated with the mixed dense and fusinoid results. Mixed porous are negatively correlated with mixed dense, inertoid dense and oxidized cracked results.

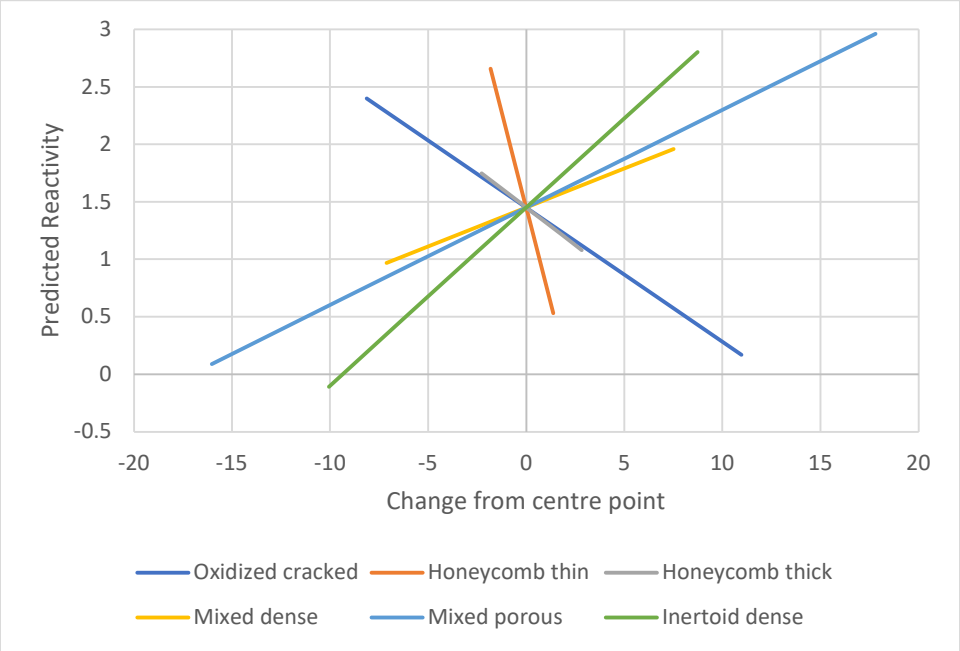

Figure 31: Sensitivity analysis plot of predicted reactivity as a function of the changes in the char morphology components.

5.2.5 Relationship between reactivity and CaO

Figure 32 shows the regression model fitted for reactivity as a function of calcium oxide (CaO). In the depicted graph, the x-axis represents the concentration of CaO (calcium oxide), while the y-axis displays the corresponding reactivity values. The model has a R^2 = 0.71 and standard error equal to 0.23 x 10^{-5} g/g/s or 15.69 %. In Figure 32 there is a positive relationship between reactivity and calcium oxide. A distinct highlight on the graph draws attention to a specific area, marking the 95% confidence interval. This shaded region adds a layer of statistical significance to the data

points, indicating the range within which the true values are likely to fall. The solid black line represents the mean value of the data.

Notably, out of the seven data points plotted, five lie comfortably around and within this highlighted area, suggesting a consistent and reliable pattern. The positioning of these points within the confidence interval contributes to the overall understanding of the relationship between CaO concentration and reactivity, emphasising the reliability and accuracy of the observed trends. This implies that reactivity increases with an increase in CaO concentration. However, the presence of data points remote from the confidence interval raises questions about potential outliers or external factors influencing the reaction.

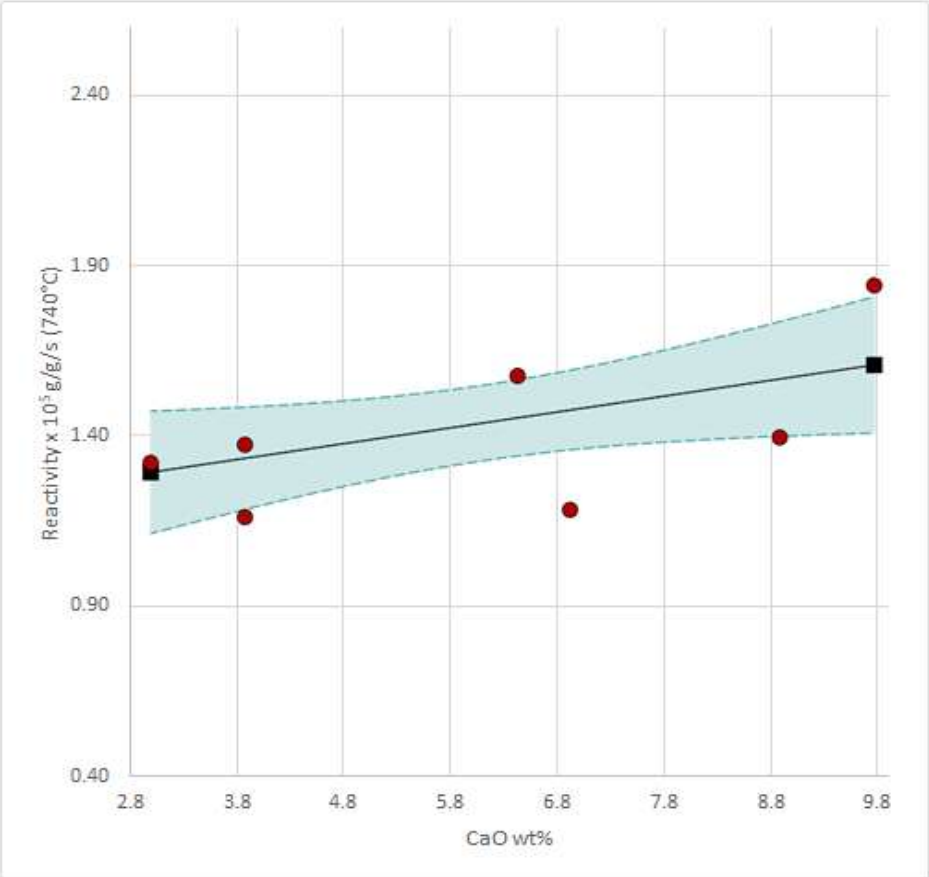

Figure 32: Correlation between reactivity and CaO content (wt%).

Table 23 contains the significant variables and coefficients of the model. For every 1 °C increase in temperature, reactivity increases by 0.038 x 10^{-5} g/g/s. The p-values indicate that the variables are significant (p-value < 1). The p-value of CaO is equal to $4.57 \cdot 10^{-02}$, which indicates that the

variable is significant on a 4.57 % level i.e. there is a 95.4 % confidence that the CaO has a true effect on reactivity.

Table 28: Regression model for reactivity and CaO coefficients and p-values.

Variables	Coefficients	P value
Temperature	0.038	$1.00 \cdot 10^{-4}$
CaO	0.043	$4.57 \cdot 10^{-2}$

In their study, Liu *et al.* [115] have identified that CaO is a key chemical compound that has a significant impact on the AFTs (ash fusion temperatures) of coal samples. The coal AFT is reduced to a minimal degree by the presence of alkaline oxides (CaO, MgO, and Fe_2O_3). Mao *et al.* [109] examined the impact of including a CaO catalyst on the slagging characteristics and ash sintering temperature. They observed a decrease in ash sintering temperature with an increase in CaO [109]. The impact CaO on the slagging characteristic is however, contingent upon the quantity of CaO, reaction circumstances, and the inherent properties of the selected coal [109].

The increase in reactivity aligns with the decline in ash sintering temperature [176]. Coals with high reactivity tend to liberate volatile materials more easily during combustion, resulting in an increased combustion rate [42]. The combustion of high-reactivity coals can lead to elevated temperatures within the combustion zone [138]. Increased combustion temperatures can affect the process of sintering in ash, potentially lowering the temperature at which ash begins to sinter [176].

5.2.6 Relationship between reactivity and CaO x Ash Yield

The coefficients of the regression model for reactivity as a function of CaO x Ash yield is shown in Table 23. Multiplying the concentration of CaO (calcium oxide) by the ash yield in coal analysis serves to calculate the amount of CaO present in the ash fraction of the coal, resulting in a better comparison between samples. The rationale for this multiplication is to quantify the contribution of CaO to the overall ash content. By determining the concentration of CaO and multiplying it by the ash yield, you get the amount of CaO that is present in the ash component of each coal. The model has a $R^2 = 0.87$ and standard error equal to 0.16×10^{-5} g/g/s or 11 %. The p-value of CaO x Ash Yield is significant on a 0.02 % level i.e. there is a 99.98 % confidence that the variable has a true effect on reactivity.

Table 29: Regression model for reactivity and CaO x Ash yield coefficients and p-values.

Variables	Coefficients	P value
Temperature	0.038	$1.00 \cdot 10^{-4}$
CaO x Ash Yield	0.043	$2.00 \cdot 10^{-4}$
Temperature (CaO x Ash Yield)	0.110	$5.13 \cdot 10^{-2}$
(CaO x Ash Yield) ^{2}	0.247	$6.10 \cdot 10^{-3}$

Figure 33 shows the observed reactivity as a function of calcium oxide (CaO) x Ash yield.

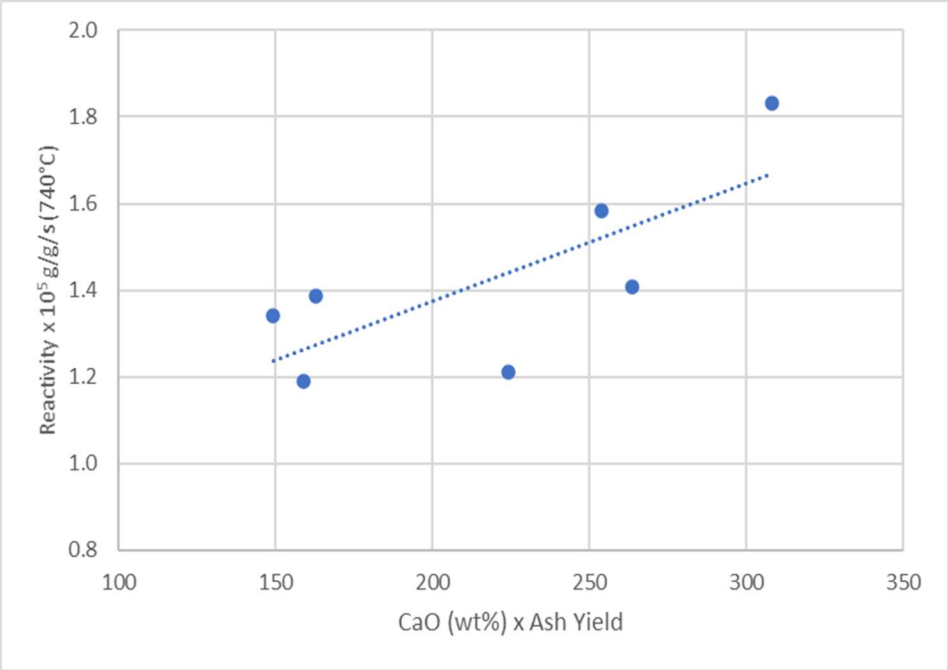

Figure 33: Correlation between reactivity and CaO x Ash Yield.

It is important to note the standard error here, which is in reactivity units, is smaller than the standard error observed from the relationship between reactivity and CaO. Figure 34 shows a contour plot for the predicted reactivity as a function of CaO x ash yield and temperature. From this figure, there is a larger increase in reactivity at higher CaO x Ash concentrations, confirming the catalytic effect of CaO.

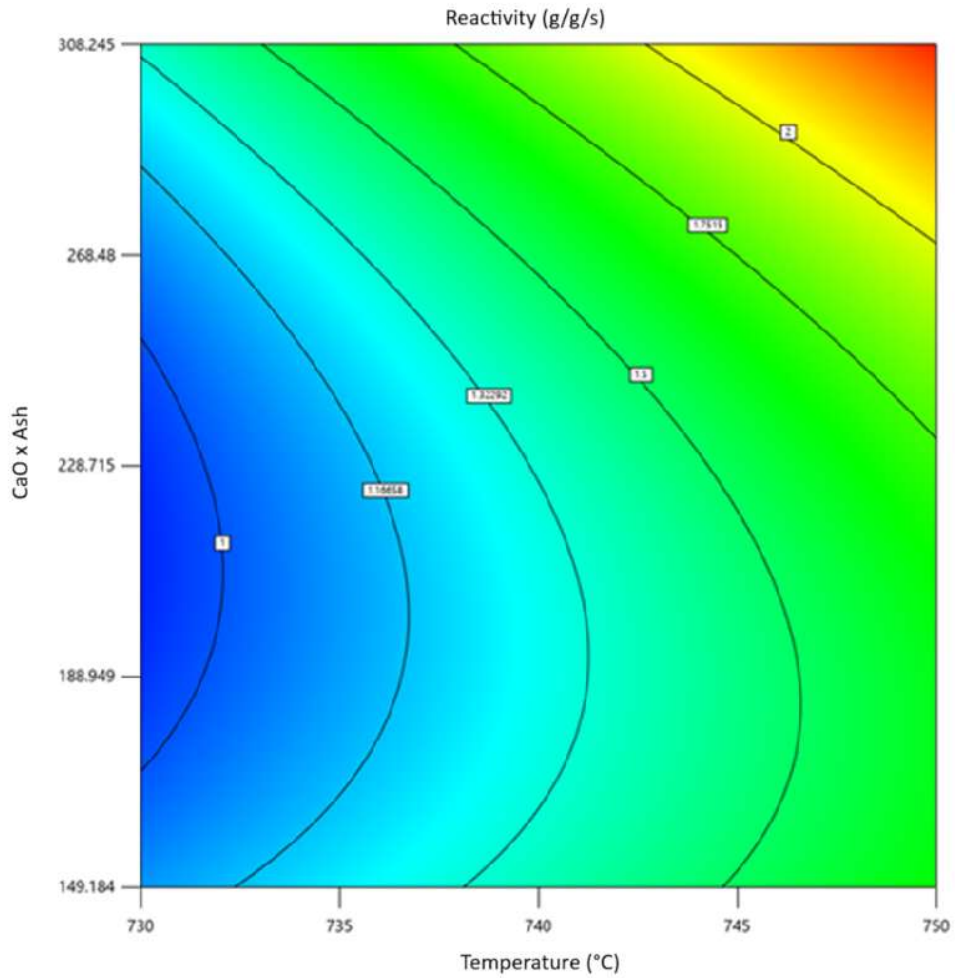

Figure 34: Contour plot showing the predicted reactivity as a function of changes in CaO x Ash Yield and Temperature.

5.2.7 Relationship between reactivity and Si/Al

Figure 35 shows the observed reactivity as a function of Si/Al, using all the data for the different sources at 740 °C. The model has a R^2 = 0.74 and standard error equal to 0.22 x 10^{-5} g/g/s or 15.56 %.

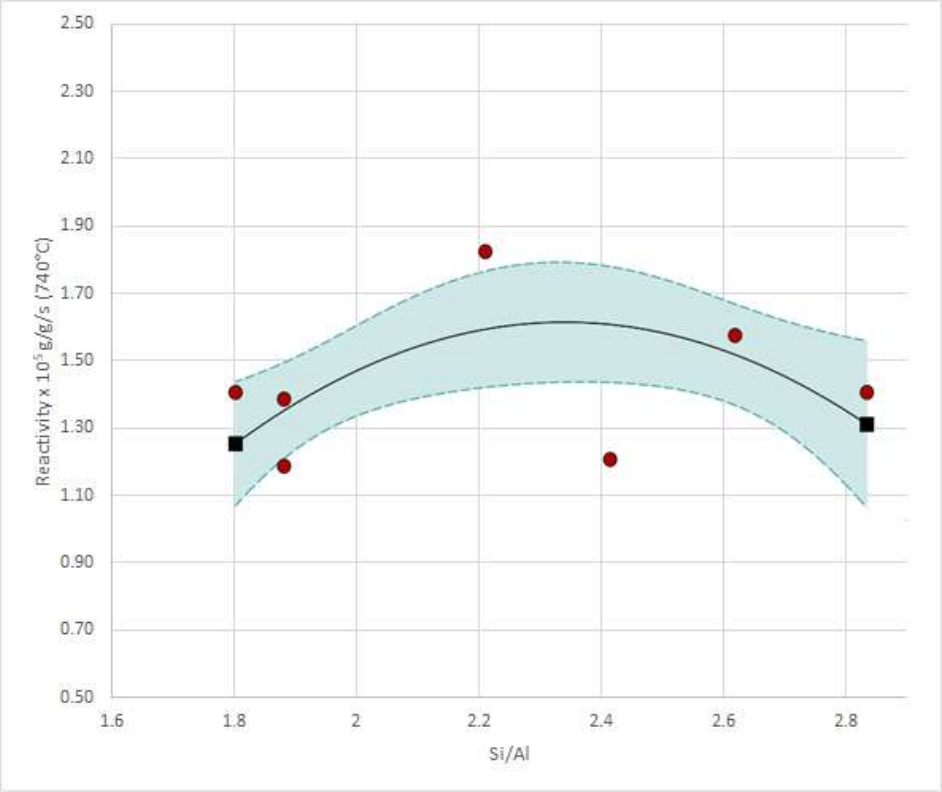

Figure 35: Correlation between reactivity and Si/Al ratios.

From the data in this study, lower Si/Al ratios, boosts reactivity catalytically up to an Si/Al ratio of 2.3 where the inhibiting effect is observed. It is however, recommended that more data points should be used to confirm the results obtained. The inhibitory impact becomes evident at higher Si/Al ratios. This inhibitory effect occurs because the increased presence of silicon can block active sites on the catalyst, reducing its overall effectiveness [177]. As a result, the catalytic activity of the material decreases as the Si/Al ratio continues to rise.

He *et al.* [178] investigated the effects of Si and Al on Fe catalysed brown coal and found that the activity of the Fe catalyst is improved with the increase in Si and Al content at 0.1 to 1 wt %. Simultaneously, Si and Al inhibits the activity of Fe at higher weight percentages (> 1 wt %), similar to the results observed in Figure 35.

Lu *et al.* [152] conducted active site analysis to compare a demineralized char with an Si and Al containing char. The presence of Si and Al in the char results in a reduced number of active sites, which directly contributes to a lower reactivity during gasification [152]. This is due to the fact that Si and Al not only lack the ability to adsorb the gasifying agent, but also hinder the functionality of

certain active sites and even render some carbon inactive [152]. Similar results have been reported by Dupont *et al*. [179]

A contour plot of reactivity, Si/Al and temperature is presented in Figure 36. This visual representation shows the quadratic effect observed in the correlation between reactivity and Si/Al ratio at different temperatures. At Si/Al ratios lower than 2.10, reactivity decreases with and increase in Si/Al. The opposite is however true for Si/Al ratios higher than 2.10.

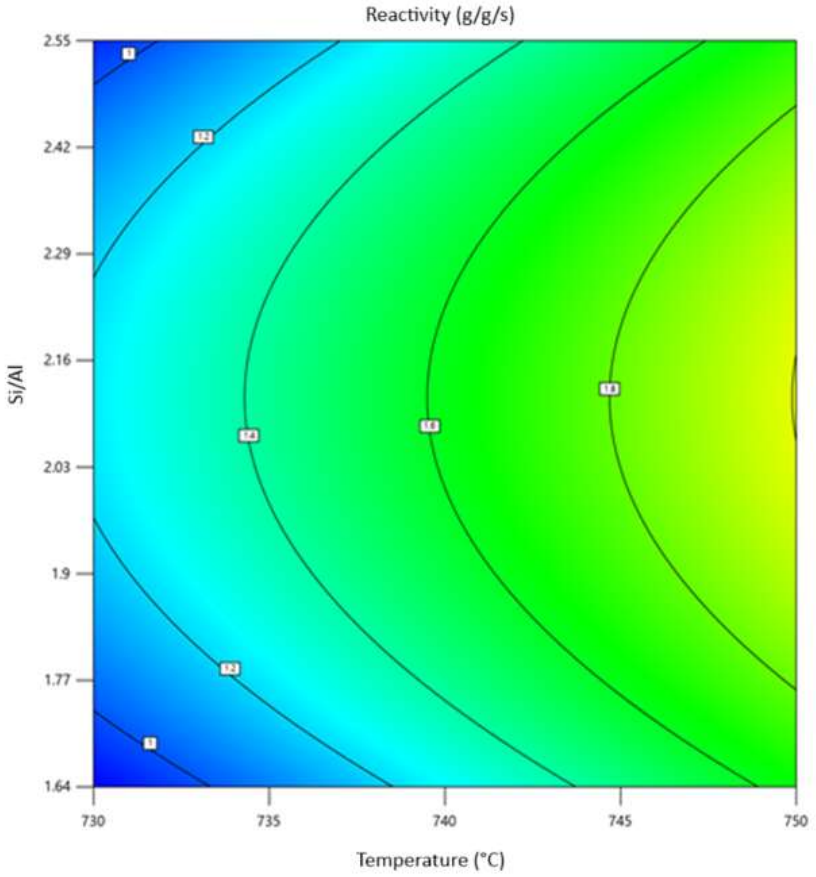

Figure 36: Contour plot showing the predicted reactivity as a function of changes in CaO x Ash Yield and Temperature.

Table 30 contains the coefficients and p-values of temperature, Si/Al and Si/Al^2. The quadratic effect of Si/Al ratio is statistically significant with a p-value equal to 0.0197. The high R^2 value indicates that the correlation is accurate. This indicates that the Si/Al ratio is a good variable to consider compared to the other correlations considered in this chapter.

Table 30: Regression model for reactivity and Si/Al coefficients and p-values.

Variables	Coefficients	P value
Temperature	2.08	$1.00 \cdot 10^{-4}$
Si/Al	0.01	$6.79 \cdot 10^{-1}$
$(Si/Al)^2$	0.33	$1.97 \cdot 10^{-2}$

5.2.8 Relationship between reactivity and Alkali Index

Figure 37 shows the regression model fitted for reactivity as a function of the alkali index, using all the data for the different sources at 740 °C. The model has a R^2 = 0.68 and standard error equal to 0.24 or 16.26 %.

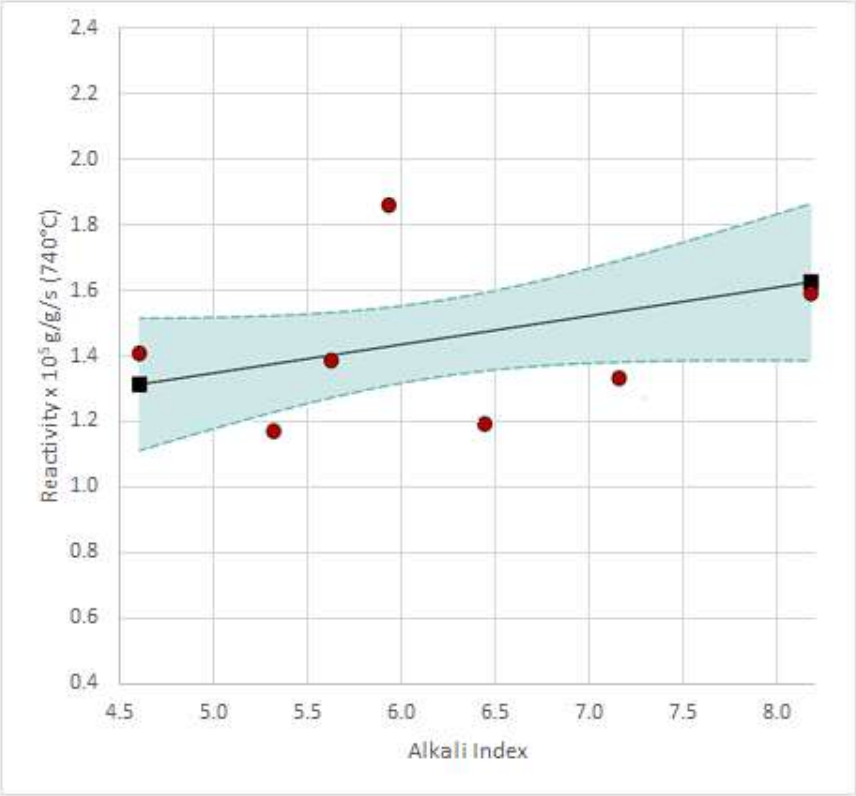

Figure 37: Correlation between reactivity and Alkali Index.

The reactivity has a positive correlation with the alkali index. The alkali index is a metric introduced by Sakawa *et al.* [108] to measure the catalytic capabilities of naturally occurring minerals in coal. Multiple authors have verified a strong positive association between reactivity and the alkali index

[180],[181]. This correlation suggests that minerals with higher alkali index values are more effective catalysts for coal reactions [135]. It also indicates that the alkali index can be a reliable indicator of a mineral's ability to facilitate chemical reactions in coal [158].

Furthermore, studies have shown that the alkali index is not only indicative of a mineral's catalytic capabilities, but it can also provide insights into the overall reactivity of coal itself [158]. By analyzing the alkali index of different coal samples, researchers have been able to predict the extent to which these samples will undergo chemical reactions when exposed to certain conditions [158],[180],[181]. Table 31 contains a summary of the coefficients and p-values of temperature and alkali index. From the p-values it can be noted that temperature and alkali index have a significant effect on the reactivity.

Table 31: Regression model for reactivity and alkali index coefficients and p-values.

Variables	Coefficients	P value
Temperature	1.99	$1.00 \cdot 10^{-4}$
Alkali Index	0.17	$9.76 \cdot 10^{-2}$

Figure 38 shows the contour plot of reactivity, temperature and alkali index. Reactivity increases with an increase in alkali index and temperature.

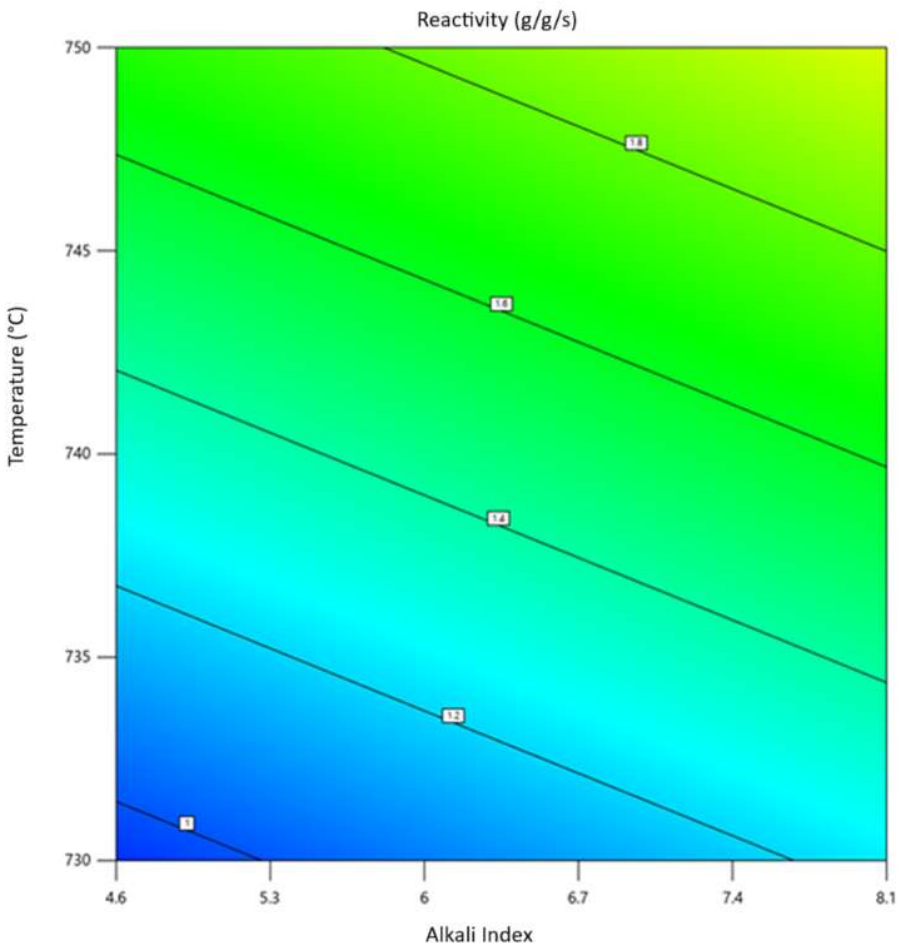

Figure 38: Contour plot showing the predicted reactivity as a function of changes in Alkali Index and Temperature.

5.3 Difference in reactivity between coal sources

The objective of the statistical regression analysis is to quantify the difference in reactivity between the different coal sources, and the relationship between reactivity and temperature. Figure 39 shows the parity plot for the model. From Figure 39, it is observed that there exists a strong positive but linear trend of reactivity with increasing temperature for the different sources. Note that a p-value smaller than 0.05 indicates that the variable has a significant effect on the response at significance level 5 %, or there is 95% confidence that the variable affects the response.

Tukey Honest Significant Differences (HSD) tests were performed to assess which sources are different with respect to their reactivity. Equation (3.13) was used to quantify the differences in reactivity between the coal sources.

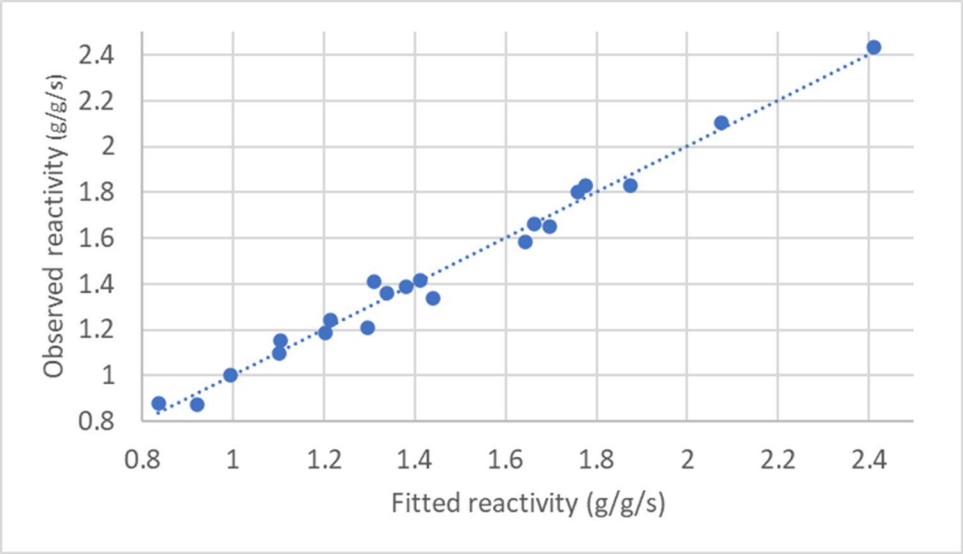

Figure 39: Parity plot of observed reactivity versus model predicted values.

The predicted reactivities of all seven coal char samples are plotted in Figure 39 for the different temperatures (730, 740 and 750 °C). Due to the significant interaction between temperature and the coal sources, the slopes of the regression lines are different in Figure 40 for the different coal sources. The average reactivity difference between the predicted and experimental reactivities was determined to be 0.085 x 10^{-5} g/g/s over all three temperatures. Theoretically, the relation between reactivity and temperature is described by the Arrhenius equation. The linear relation used for the predicted reactivities as shown in Figure 39, is still an acceptable approximation, given the relatively small temperature interval that was used [136]. Further details regarding the differences in experimental and predicted reactivities are provided in Appendix F.

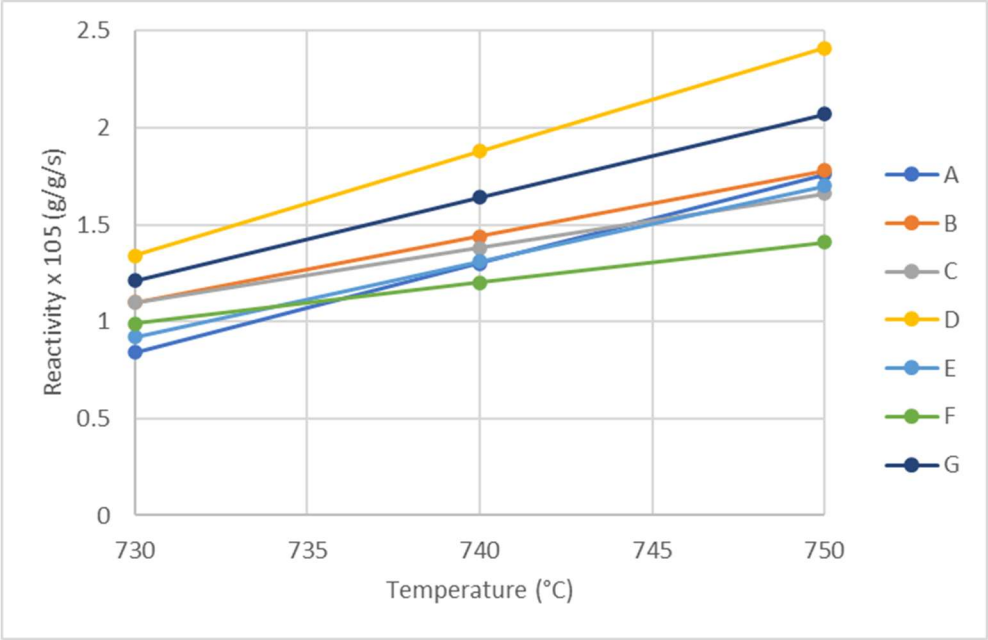

Figure 40: Predicted reactivities as a function at 730, 740 and 750 °C.

Figure 41 shows the difference in reactivity between the coal sources (only two samples compared as indicated by the legend). The regression model output indicates that the reactivity of Sample C is significantly higher (0.26 g/g/s higher) compared to that of Sample F at average temperature. Also, reactivity of Sample A is significantly higher (0.49 g/g/s higher) compared to that of Sample F at average temperature. See Appendix F for more information.

The reactivity of each pair of coal sources is compared individually. For example, there are seven coal sources (A, B, C, D, E, F and G), which are then compared (A vs. B, A vs. C, and B vs. C). Each comparison focuses on the difference in reactivity between the two sources being compared. For each pairwise comparison, a 95% confidence interval (CI) is also calculated. The confidence interval provides a range of values within which the true difference in reactivity is expected to lie with 95% confidence. This means that if you repeated the experiment many times, 95% of the calculated confidence intervals would contain the true difference in reactivity between the two sources.

The magnitudes of the differences in the reactivity between the sources together with the 95% confidence interval of the differences (pairwise comparisons) can be observed from the output as shown in Figure 41. The data points are labelled to the right as shown. If the confidence interval for the difference in reactivity between two coal sources does not include zero, it means that the difference between the sources is statistically significant at the 5% significance level. If the interval

contains zero, it suggests that the difference in reactivity could be zero, meaning the two sources might not be different in terms of reactivity. If the interval does not contain zero, you can be confident that there is a real difference between the two sources.

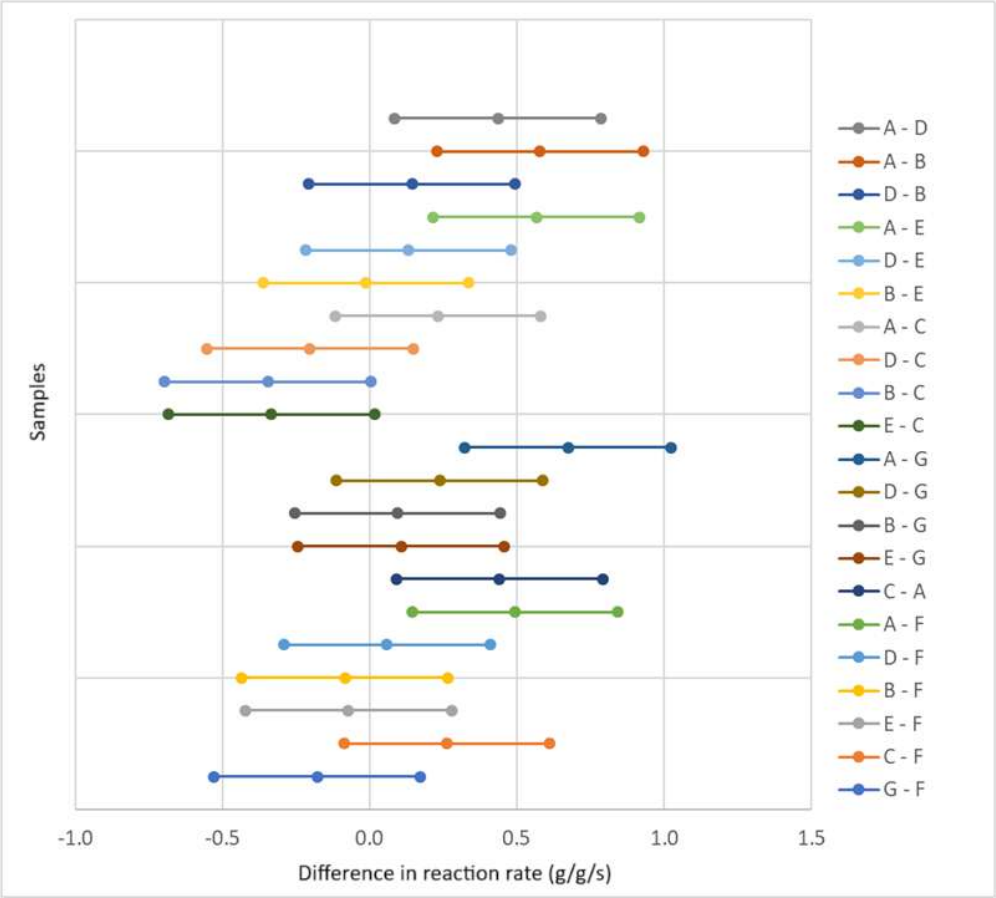

Figure 41: Differences in mean levels of source samples

The middle dot presents the mean difference in reactivity between the two sources compared (e.g., G – F = reactivity of Sample G minus the reactivity of Sample F). This is an indication of the extent to which the reactivities of the two samples differ. Data points than includes the zero/ centre point (on x-axis) indicates that there is statistically little to no difference in the reactivities as seen with Samples B and E, at a 5 % significance level. There are however several samples that show statistically significant differences in reactivity with at least 95 % confidence. These are the confidence intervals that do not contain zero.

The comparison between Samples A and E is one example showing a statistically significant difference in reactivity. The confidence interval of A - E is on the positive side not including the

zero/ centre point, therefore the reactivity for coal source A is significantly greater than the reactivity for coal source E. The comparison between Samples E and C (E – C) is on the negative side, indicating that the reactivity for coal source C is significantly larger than that of E.

5.4 Results and Discussion Summary

From the summary in Table 32, it is observed that the best model for prediction is reactivity as a function of the temperature and ultimate analysis of the coal, which has the highest R^2 value and smallest standard error of the model. The char morphology is a difficult and complex analysis, it is thus recommended to use the relation between reactivity and ultimate analysis [103].

Table 32: Summary of R^2 values and standard errors of the regression models.

Variable	R^2	SE of Fit
Proximate analysis	0.78	0.19
Ultimate analysis	0.90	0.12
CaO	0.71	0.23
CaO x Ash yield	0.87	0.16
Si/Al ratio	0.74	0.22
Alkali index	0.68	0.24
Maceral group analysis, excluding minerals	0.63	0.24
Char morphology analysis	0.90	0.12

Table 33 contains the predicted reactivities as a function of temperature, as well as the specific reactivity results from the gasification experiments. As shown, the predicted reactivities are relatively close to the reactivities obtained through the gasification experiments. There are some differences between the predicted and experimental reactivities, but the results are relatively close at 730 and 750 °C. The deviation between the experimental and estimated reactivities is smaller than 6 % (0.09 x 10^{-5} g/g/s) with an average difference of 3 % (0.04 x 10^{-5} g/g/s).

Table 33: Reactivity estimations based on temperatures.

Sample	r x 10^5 (g/g/s)					
	730 °C		740 °C		750 °C	
	Experimental	Estimated	Experimental	Estimated	Experimental	Estimated
A	1.36	1.34	1.83	1.88	2.43	2.41
B	0.88	0.84	1.21	1.30	1.8	1.76
C	1.24	1.21	1.58	1.64	2.1	2.07
D	1.16	1.10	1.34	1.44	1.83	1.78
E	0.87	0.92	1.41	1.31	1.65	1.70
F	1.10	1.10	1.39	1.38	1.66	1.66
G	1.00	0.99	1.19	1.20	1.42	1.41

Chapter 6: Conclusions and recommendations

6.1 Introduction

Seven bituminous (medium rank C) coal samples were obtained in lump size and representative coal char samples with a particle size range of -150+75 µm was prepared using mechanical size reduction and devolatilization in a N_2 atmosphere. From the characterization analysis carried out on the coals it was found that the parent coal is rich in inertinite and consists of a high ash content. The chemically controlled regime was determined as the temperature range where there are no mass transfer limitations, and determined to be below 750 °C. The coal char reactivities obtained at 730, 740 and 750 °C show significant differences. Some of the coal samples have higher reactivities compared to others, depending on the temperature used during gasification. All the gasification experiments were conducted at a pressure of 30 bar in a CO_2 atmosphere and conversions up to 12%. From the parent coal analysis and conversion results obtained, the reactivities were determined.

This chapter provides the conclusions drawn from the experimental results and discussed in Section 6.2 and 6.3 addresses the contributions to science and the recommendations for further studies respectively.

6.2 Conclusions

From the characterization analysis of the coal samples, it was found that these coal samples are inertinite rich, bituminous and medium rank C samples. The reactivity of CO_2 gasification was conducted under conditions in which the overall reaction rate is solely controlled by the surface reaction. The reaction rate was exclusively dependent on the temperature and the partial pressure of CO_2 under these circumstances. The reaction rate exhibited a positive correlation with temperature, aligning with the findings commonly documented in literature.

With an increase in hydrogen concentration and CV, there was a corresponding rise in reactivity. The tricameral group demonstrated a positive association with reactivity, in contrast to the monomaceral and bimaceral groups, which were found to have a negative effect. Liptinite shows a large positive relationship (For every 1-point increase in liptinite content, reactivity increased by 0.032 g/g/s) with reactivity, while vitrinite showed a small positive relation (For every 1-point increase in vitrinite content, reactivity increased by 0.004 g/g/s). Inertinite shows a strong negative

relation (For every 1-point decrease in inertinite content, reactivity decreased by 0.013 g/g/s). with reactivity when excluding mineral matter. The correlation of the maceral groups with mineral matter resulted in inertinite showing a positive relationship with reactivity. This can be explained by the catalytic effects of some minerals. The presence of certain minerals in inertinite can enhance its reactivity, leading to a positive relationship with reactivity when considering mineral matter. This suggests that the catalytic effects of these minerals play a significant role in influencing the reactivity of inertinite. Further research is needed to understand the specific mechanisms through which these minerals interact with inertinite and contribute to its reactivity.

Reactivity showed a positive relation with mixed porous, inertoid dense and mixed dense char characteristics. The honeycomb thin, honeycomb thick and oxidized cracked char characteristics showed a negative relation with reactivity. The relation between reactivity and oxidized cracked particles is similar to that of the relation between honeycomb thick particles.

From the correlations of intrinsic coal reactivity of the seven different single source coal samples and their respective coal characteristics it was observed that the best model for prediction is reactivity as a function of the temperature and ultimate analysis and the correlation between reactivity and char morphology analysis of the coal samples, which both have the highest R^2 value (0.90) and smallest standard error (0.12) of the model. The accuracy of this model does however need to be confirmed by comparing the predictions of other coal samples to that of the measured values. The relationship between reactivity and macerals can also be considered as the model was found to be a good fit. The correlation between reactivity and maceral group analysis (excluding minerals) showed the worst correlation ($R^2 = 0.63$) and a standard error of 0.24.

Tukey Honest Significant Differences (HSD) tests were performed to assess which sources are different with respect to their reactivity. The magnitudes of the differences in the reactivity between the sources together with the 95% confidence interval of the differences were determined. The reactivity of Sample A is the highest at 730, 740 and 750 °C followed by Sample C. Samples D, E and F have similar reaction rates at 740 °C, while samples B and G also have similar reactivities at 740 °C. Samples B and G have similar reaction rates at 730 °C but different reactivities at 740 and 750 °C. The order of the coal sources are as follows for reactivity at an average temperature, from greatest to smallest: A > C > D > F > E > B > G.

6.3 Contribution to existing knowledge field and science

The following contributions were made to the existing knowledge field and science:

- The systematic determination of coal char reactivity in a high-pressure CO_2 atmosphere in the chemically controlled regime for South African coal chars.
- The results of this investigation can be incorporated into coal gasifier models and used to simulate and predict the gasification of selected Highfield coal chars at elevated pressures.

6.4 Recommendations

Based on the investigations conducted and conclusions drawn in this study, the following recommendations are made for further studies on the underlying topic:

- Other Highfield coal samples can be used to test the model predicting the reactivity as a function of temperature and ultimate analysis as this was the most accurate model.
- Investigate the inhibition effects of product gases such as CO and H_2 to better understand the char reactivity.
- Evaluation of the impact of mineral matter on pore development of coals from different areas.
- Find the correlation between reactivity and the pyrite content of the coal samples.
- Conduct correlations between individual coal properties and coal reactivity.
- Determine the ash fusion temperatures of the coal samples.

Low pressure gasification studies should also be considered and compared with the results obtained in this study.

Appendix A: Evaluation of operating regime

The ideal operating regime would contain no internal mass transfer limitations. In order to ensure that there were no internal mass transfer limitations, large and small coal char particles were gasified at the same operating conditions. The large particles were in the range of -450 +300 µm, while the small particles ranged from -150 +75 µm. The specific reactivities at 750 °C and 30 bar of these coal char particles were then compared as shown in Figure 42. The reaction rates of the large particles and the small particles are relatively close to each other, confirming the absence of mass transfer limitations.

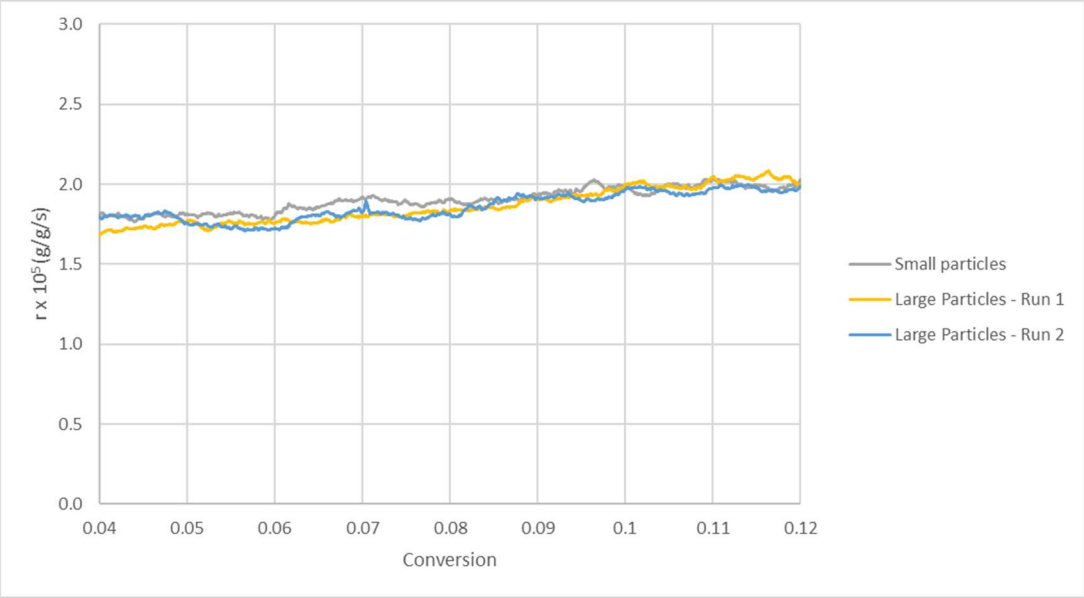

Figure 42: Reaction rate mass transfer limitations test (Sample D)

Figure 43 shows the mass transfer limitations test of Sample G at 750 °C and 30 bar. Again, the reaction rates of the larger particles and smaller particles are relatively close. This again confirms the absence of mass transfer limitations.

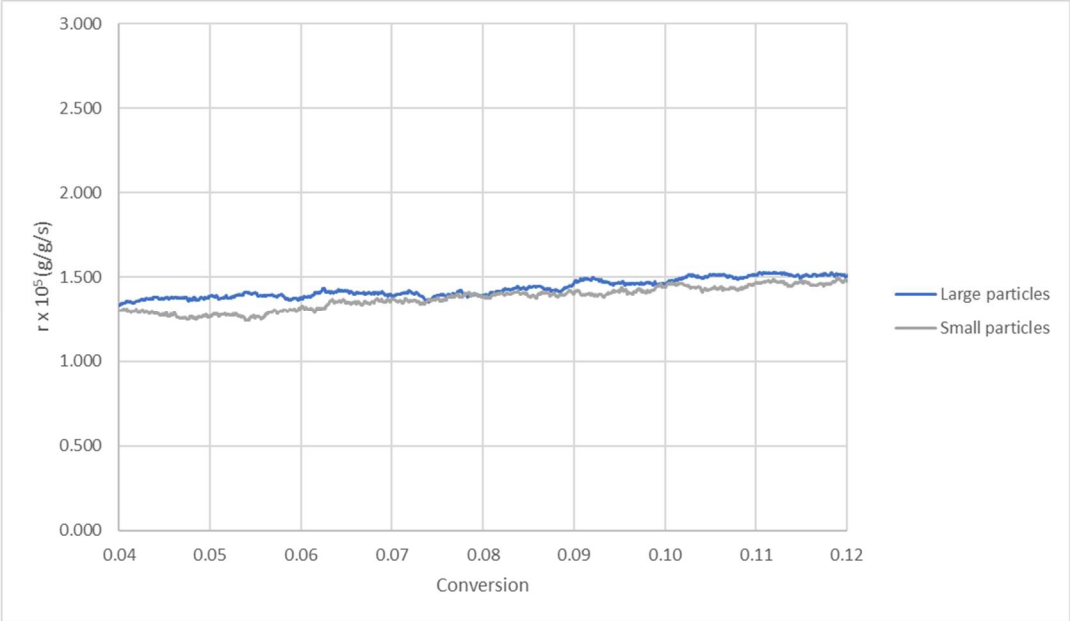

Figure 43: Reaction rate mass transfer limitations test (Sample G)

Appendix B: Equipment calibration

Appendix B.1: Mass flow controller (MFC)

The two MFC's supplied by Bronkhorst High-Tech® was re-calibrated to ensure that the specific amount of CO_2 is present in the total gas stream. The 1st MFC has a flow rate range of 0 to 0.75 NL/min and was calibrated for N_2 using a bubble flow meter with 50 ml increments. The actual gas flow rates at certain MFC set points were monitored under atmospheric conditions as depicted in Table 34. The set points were ranged from 0.2 to 0.7 NL/min and the actual flow rates at these set points were measured.

Table 34: N_2 MFC calibration data

MFC (NL/min)	Flow rate (NL/min)	Standard flow rate (NL/min)
0,20	0,22	0,18
0,30	0,32	0,26
0,40	0,41	0,33
0,50	0,53	0,43
0,60	0,64	0,52
0,70	0,75	0,61

The measured actual flow rates were converted to flow at standard conditions (1 atm and 0°C) using Equation C.1. The temperature and pressure at the time of calibration was 17.5 °C and 0.86 atm respectively.

$$\dot{V}_{STP} = \dot{V}_a \left(\frac{T_{STP}}{T_a}\right)\left(\frac{P_a}{P_{STP}}\right) \quad \text{(C.1)}$$

Figure 44 illustrates the linear behavior of the calibration data and confirms that the linear regression model is best suited for accurate data representation. The linear regression model was used to express the MFC set point as a function of the standard flow rate.

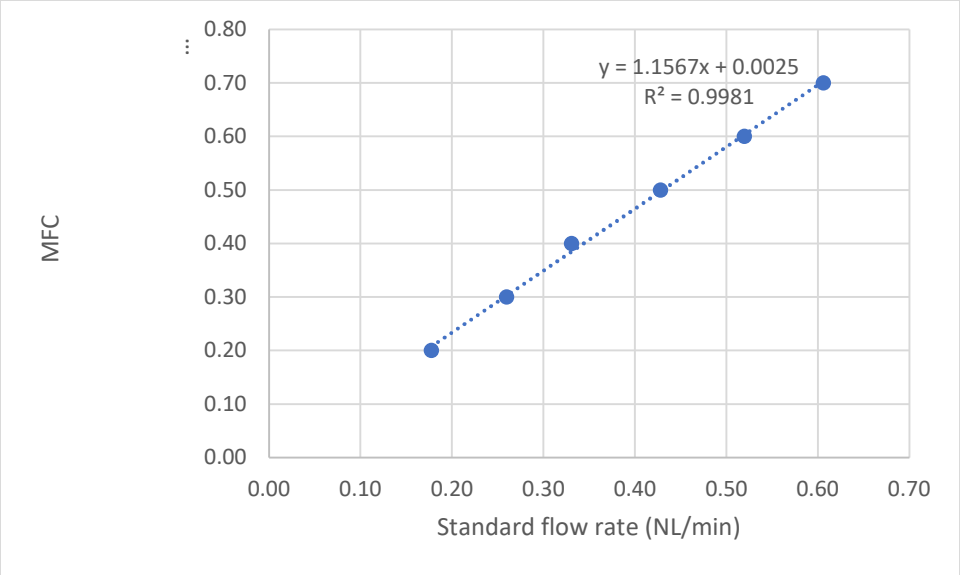

Figure 44: N_2 MFC calibration curve

The calibration curve was used as presented in Equation C.2 to determine a specific flow rate in conjunction with the MFC set point.

$$MFC_{set\ point}\left(\frac{NL}{min}\right) = 1.1567\dot{V}_{STP} + 0.0025 \tag{C.2}$$

The 2nd MFC has a range of 0 to 5 NL/min and was calibrated for CO_2 by using a bubble-flow meter with 500ml increments. The set points were ranged from 0.5 to 3 NL/min and the actual flowrate was then determined at each set point. The flow rates at standard conditions were calculated using Equation C.1 and summarized in Table 35.

Table 35: CO_2 MFC calibration data

MFC (NL/min)	Flow rate (NL/min)	Standard flow rate (NL/min)
0,50	0,38	0,31
1,00	1,00	0,81
1,50	1,50	1,21
2,00	2,14	1,73
2,50	2,73	2,20
3,00	3,33	2,69

The linear regression model was used as shown in Figure 45 to express the MFC set point as a function of flow at standard conditions.

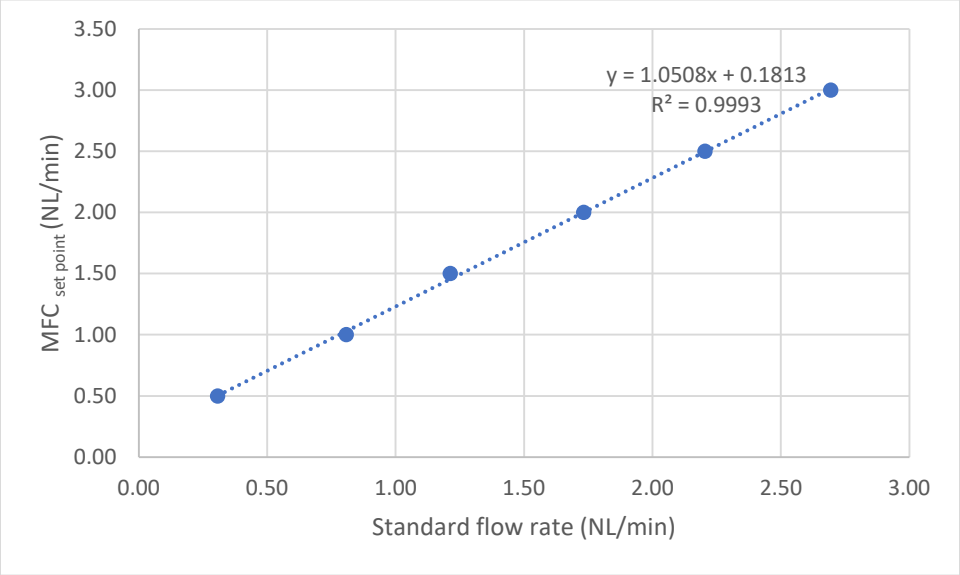

Figure 45: CO_2 MFC calibration curve

The specific flow rate in conjunction with the MFC set point is determined using Equation C.3.

$$MFC_{set\ point}\left(\frac{NL}{min}\right) = 1.05\dot{V}_{STP} + 0.18 \tag{C.3}$$

The setpoint was calculated and used to ensure that a constant CO_2 flow rate of 2NL/min was used for conducting all the gasification experiments.

Appendix B.2: CO Analyser

The CO analyser was calibrated using a CO calibration gas of know concentration. The CO calibration gas was allowed to enter the system and measured using the CO analyser. The results obtained are summarized in Table 36 and were used to create the calibration curve showed in Figure 46.

Table 36: CO analyser calibration data

CO, detected (ppm)	CO, actual (ppm)
-231	0
-245	0
868	1000
871	1000
3539	3900
3546	3900

The actual CO concentrations were plotted against the detected CO concentrations and a trendline was fitted to the data. This calibration curve was then used to adjust the measured CO concentration to the actual concentration. This process was repeated throughout the gasification experiments to ensure that the analyzers reading remains accurate.

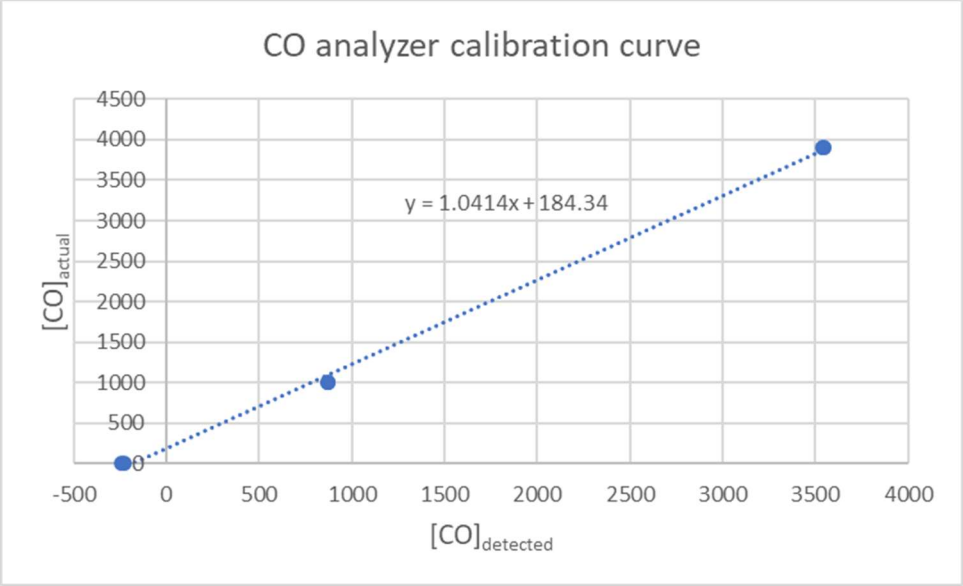

Figure 46: CO analyzer calibration curve

Appendix C: Gasification reactivity

Appendix C.1: Carbon mass balance

Raw experimental data was obtained using a CO gas analyzer and the true concentrations determined by using the calibration curves as discussed in Appendix B: Equipment calibration. One random sample was chosen as an example for this section. The sample was gasified at 850 °C and 30 bar to ensure complete conversion was achieved of the sample. Figure 47 shows the CO concentration profile of Sample A over time.

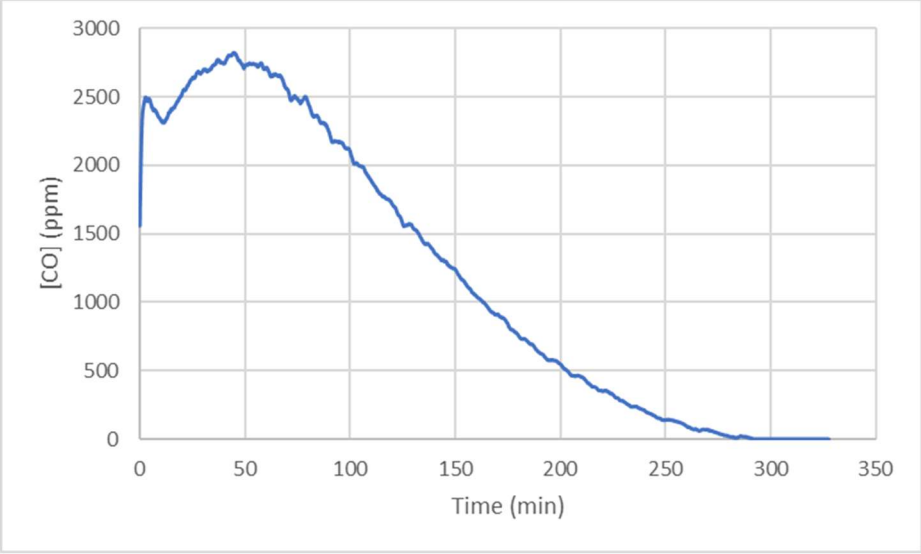

Figure 47: Sample A CO concentration profile, 30 bar and 850 °C

The CO concentration profile of Sample A increased significantly in the first 50 min, followed by a gradual decrease to an extent where the CO concentration was low and levelled off. The CO concentration profile was used to determine the conversion curve as shown in Figure 48

From the measurement of the CO concentrations Figure 47, the carbon conversion was determined. In order to determine the precise reaction rate related to the consumption or conversion of carbon inside the char, which is undergoing a reaction with CO_2, the stoichiometry of the total reaction is employed. In this particular scenario, the rate at which carbon is converted is immediately ascertained based on the measured rate of carbon monoxide (CO) production. The instantaneous rate of carbon conversion is determined by employing the subsequent equation;

$$r_C = \frac{1}{2}\left(\frac{\dot{V}_T}{V_{STP}}\right)[CO]MW_C \quad \text{(B.1)}$$

Where r_c is the instant rate of carbon conversion, $\dot{V}_T$ is the total standard volumetric flow rate of the product gas, V_{STP} is the standard molar volume at standard temperature and pressure, determine from Equation C.1. [CO] is the true CO concentration produced and MW_C is the carbon molecular weight. Equation B.1 was then used to determine the mass of carbon fed ($\Delta m_{C,t}$), which is given by Equation B.2.

$$\Delta m_{C,t} = \int_{t_0}^{t_i} r_C dt \approx \frac{\Delta t}{2}\left[\sum_{i=1}^{n}\left(r_C(t_{i-1}) + r_C(t_i)\right)\right] \quad \text{(B.2)}$$

Where t is time, and Δt is the time interval between measurements which is 3 seconds in this case (The CO concentration is logged every 3 seconds by the analyzer). Given that the accurate measurement of carbon monoxide (CO) concentration is often stated in parts per million (ppm), the conversion rate of carbon can be quantified as 10^5 (g/s). The total standard volume flow rate of the product gas is converted to a total molar flow rate, as indicated by Equation B.1. From this total molar flow rate, the molar flow rate of CO produced is determined by utilising the measured CO concentration. Subsequently, the stoichiometric analysis of the complete CO_2 gasification process is employed to transform the calculated molar flow rate of carbon monoxide (CO) produced into the quantity of carbon that is either converted or consumed.

In the majority of applications and literature, the specific reaction rate is commonly quantified by the ratio of the mass of carbon converted within a given time interval to the mass of carbon fed. Consequently, the calculated molar flow rate of carbon converted is subsequently converted to the rate of carbon conversion at any given moment by employing the molecular weight of carbon. The carbon input to the reactor is primarily determined by the carbon content in the char sample, which consists of volatile materials, ash, and fixed carbon.

It is apparent that in the process of char-CO_2 gasification, the carbon present in the char matrix undergoes conversion to carbon monoxide (CO). The rate of this carbon conversion can be estimated by employing Equation C.1. In order to ascertain the precise reaction rate, the carbon

conversion is assessed by quantifying the extent to which carbon is transformed, hence serving as an indicator of the reaction's advancement. The carbon conversion rate is quantified as the cumulative mass of carbon transformed during a specific time span, divided by the mass of carbon introduced into the reactor. The aforementioned expression is depicted in Equation B.3 in the following manner.

$$X = \frac{\Delta m_{C,t}}{m_{C,0}} = \frac{\Delta m_{C,t}}{m_{Char}(1 - x_{ash,d.b})x_{C,daf}} \approx \frac{m_{C,0} - m_{C,t}}{m_{C,0}} \quad \text{(B.3)}$$

Where X is carbon conversion, $m_{C,0}$ is the initial mass of carbon fed, m_{Char} is the mass of the char sample, $x_{ash,d.b}$ is the weight persentage of ash on a dry basis, $x_{C,daf}$ is the weight persentage of carbon within the char sample on a dry ash free basis. From Equation B.3, the conversion profile was drawn as shown in Figure 48.

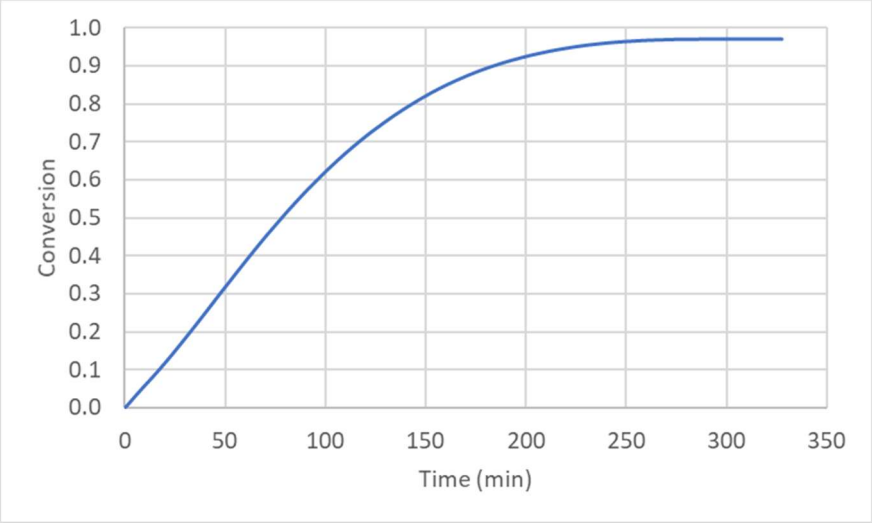

Figure 48: Sample A carbon conversion profile, 30 bar and 850 °C

Appendix C.2: Specific reaction rates

The specific reaction rates were determined from the carbon conversion measurements using the methods described in Section 3.5.4 and Equation B.4.

$$r_s = \frac{1}{1-X}\frac{dX}{dt} = \frac{1}{m_{C,0} - \Delta m_{C,t}}\frac{d\Delta m_C}{dt} = \frac{1}{m_{C,t}}\frac{dm_{C,t}}{dt} \tag{B.4}$$

The specific reaction rate r_s (g/g/s) of Sample A showed an initial decrease, followed by a constant increasing trend up to 90% conversion as shown in Figure 49. A large peak was initially observed at low conversions, which can be explained due to the use of pure CO_2 as reagent gas.

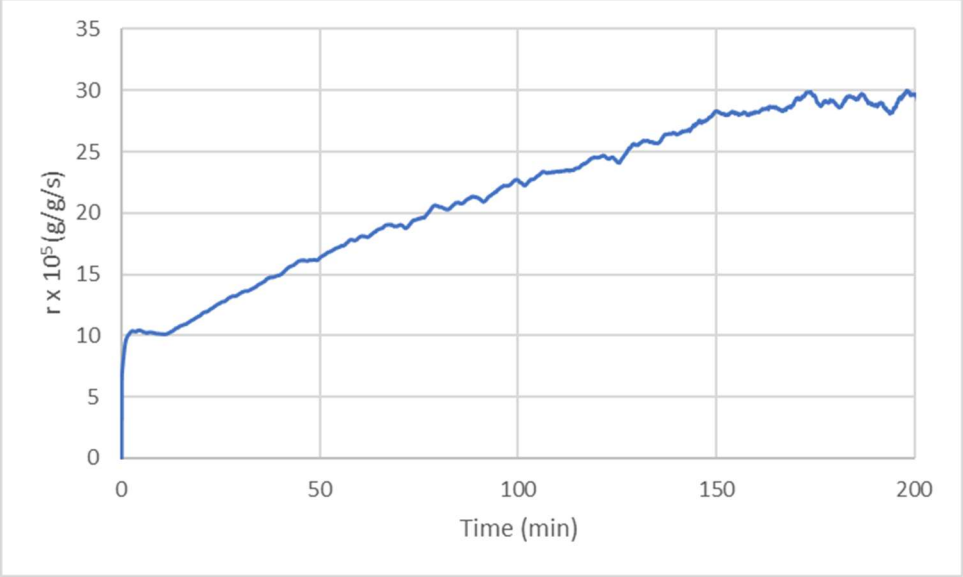

Figure 49: Sample A specific reaction rate with time, 30 bar and 850 °C

Finally, the specific reaction rate with conversion can be plotted as shown in Figure 50.

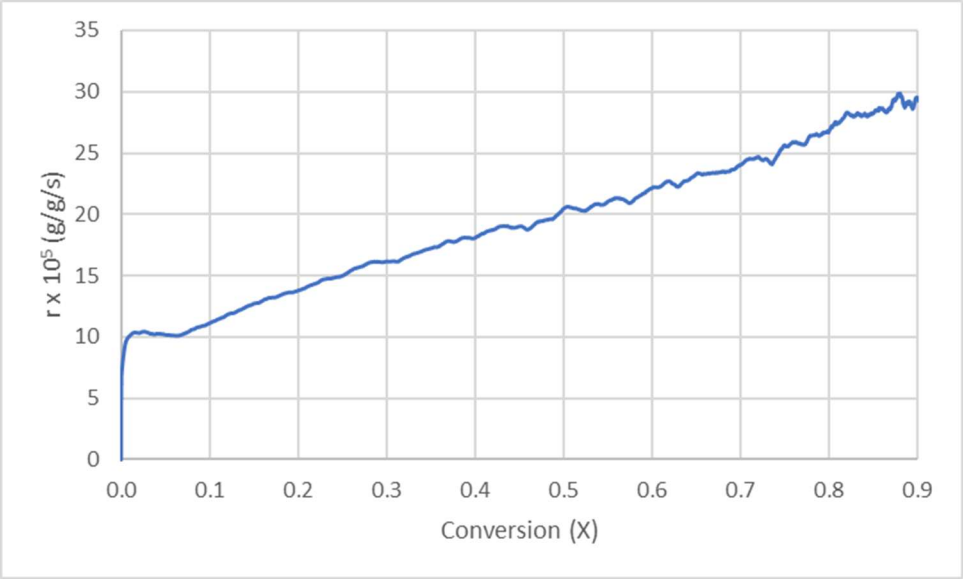

Figure 50: Sample A specific reaction rate with conversion, 30 bar and 850 °C

Appendix C.3: Experimental reaction rates

By introducing pure CO_2 a sharp peak of CO is observed as displayed in Figure 51, which only stabilises after a conversion of about 4 to 5 %. Gouws *et al.* [12] reported similar findings using a mixture of CO_2 and N_2. The peaks observed in the specific reaction rates of this study are larger and can be explained due to the fact that pure CO_2 was used. Only reactivities at a conversion of more than 4% are shown in the report as the reaction rates started stabilizing at this point.

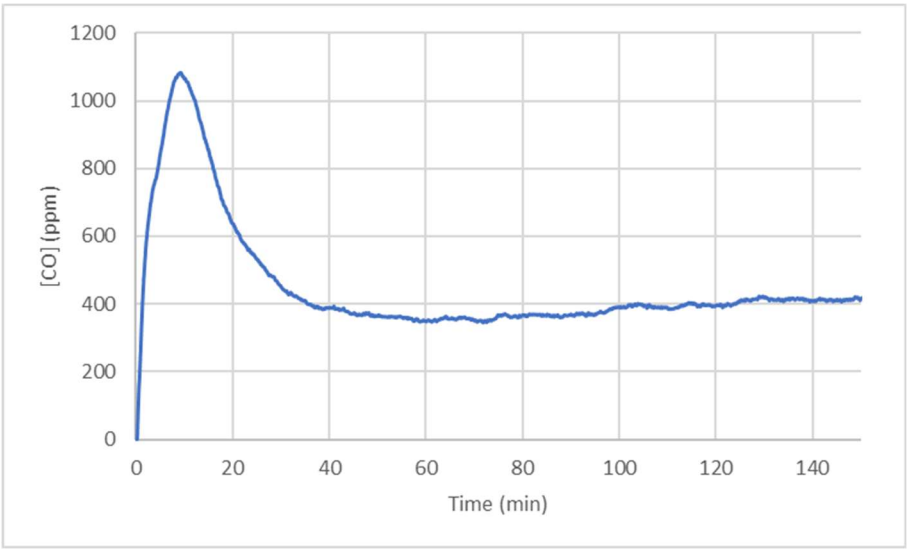

Figure 51: Specific reaction rate with conversion for Sample E at 750°C and 30 bar

Appendix C.4: Repeatability and experimental uncertainty calculations of gasification experiments

To ensure reliability of the results, some of the gasification experiments were conducted a second time. This ensured that no random errors were made and that the reaction rates obtained were accurate and reliable. Table 37 contains the specific reactivities of Sample B at conversion intervals of 2.5 % for two different experimental runs. The average of the two experimental runs were calculated first, followed by the standard deviation calculation (Equation 3.16). Using Equation 3.15, the confidence interval was obtained.

Table 37: Confidence interval of Sample B

Conversion (%)	Reactivity (g/g/s)			Standard deviation (σ)	Confidence Interval
	Run 1	Run 2	Average		
5.00	1.72	1.78	1.75	0.04	1.75 ± 0.06
7.50	1.79	1.84	1.81	0.03	1.81 ± 0.05
10.00	1.95	1.92	1.94	0.02	1.94 ± 0.03
12.50	2.04	2.01	2.03	0.02	2.03 ± 0.03
15.00	2.15	2.11	2.13	0.02	2.13 ± 0.03
17.50	2.26	2.21	2.24	0.03	2.24 ± 0.05
20.00	2.32	2.24	2.28	0.05	2.28 ± 0.07
22.50	2.41	2.32	2.36	0.06	2.36 ± 0.08
25.00	2.38	2.34	2.36	0.02	2.36 ± 0.03
27.50	2.41	2.38	2.39	0.03	2.39 ± 0.04
30.00	2.45	2.52	2.48	0.05	2.48 ± 0.07

The data points for the repeatability calculations are listed in Table 38. From the average of the differences in reactivity, it is clear that there is a very small difference of 0.053 g/g/s between the reaction rates. From the experimental repeatability calculations of Sample B and C, an average error of 0.04 (g/g/s) on a 95 % confidence level was obtained.

Table 38: Confidence interval of Sample C

Conversion (%)	Reactivity (g/g/s)			Standard deviation (σ)	Confidence Interval
	Run 1	Run 2	Average		
5.00	1.94	1.91	1.93	0.02	1.93 ± 0.03
7.50	2.01	1.97	1.99	0.02	1.99 ± 0.03
10.00	2.17	2.12	2.15	0.02	2.15 ± 0.03
12.50	2.23	2.20	2.22	0.02	2.22 ± 0.02
15.00	2.33	2.32	2.32	0.00	2.32 ± 0.01
17.50	2.44	2.40	2.42	0.02	2.42 ± 0.02
20.00	2.53	2.48	2.50	0.02	2.50 ± 0.03
22.50	2.64	2.54	2.59	0.05	2.59 ± 0.07
25.00	2.67	2.62	2.65	0.02	2.65 ± 0.03
27.50	2.76	2.64	2.70	0.06	2.70 ± 0.08
30.00	2.80	2.71	2.75	0.05	2.75 ± 0.06

Appendix D: Volatile matter

The mass loss observed during the charring of each coal sample as well as the measured amounts of moisture and volatiles are summarized in Table 39. The mass loss during the charring process consists mostly of moisture and volatiles. For some samples there are clear correlations, while others show significant differences.

Table 39: Moisture and volatiles

	Pyrolysis mass loss			Proximate analysis		
Sample	Initial Weight (g)	Final Weight (g)	Mass Loss (%)	Moisture (%)	Volatiles (%)	Moisture & Volatiles (%)
Sample A	170.0	127.3	25.1	4.4	24.8	29.2
Sample B	160.0	119.4	25.4	4.4	23.2	27.6
Sample C	160.0	121.7	23.9	3.4	21.7	25.1
Sample D	160.0	120.0	25.0	5.3	24.2	29.5
Sample E	160.0	129.7	18.9	2.5	16.9	19.4
Sample F	160.0	121.1	24.3	3.6	22.1	25.7
Sample G	160.0	123.3	22.9	3.4	20.8	24.2

Appendix E: Maceral composition.

Section F.1 expands on the microlithotype composition and contains figures for better comparison between the coal samples. The maceral composition is discussed in Section F.2 on a mineral matter free basis and excluding mineral matter.

Appendix E.1: Microlithotype composition

The microlithotype composition of the coal samples are displayed in Figure 52. This visual representation of the sample microlithotype compositions can be used to get a better understanding of the differences between. Some components are more dominant compared to others. Semifusite for example is the main component found in the microlithotype analysis.

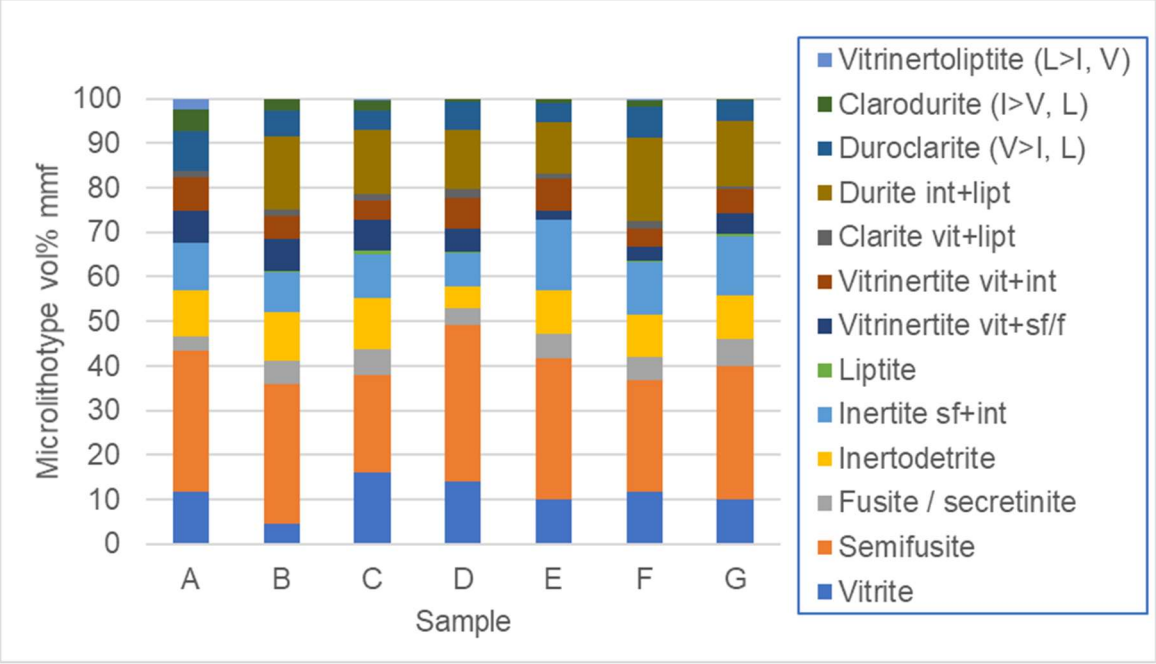

Figure 52: Microlithotype composition (mmf)

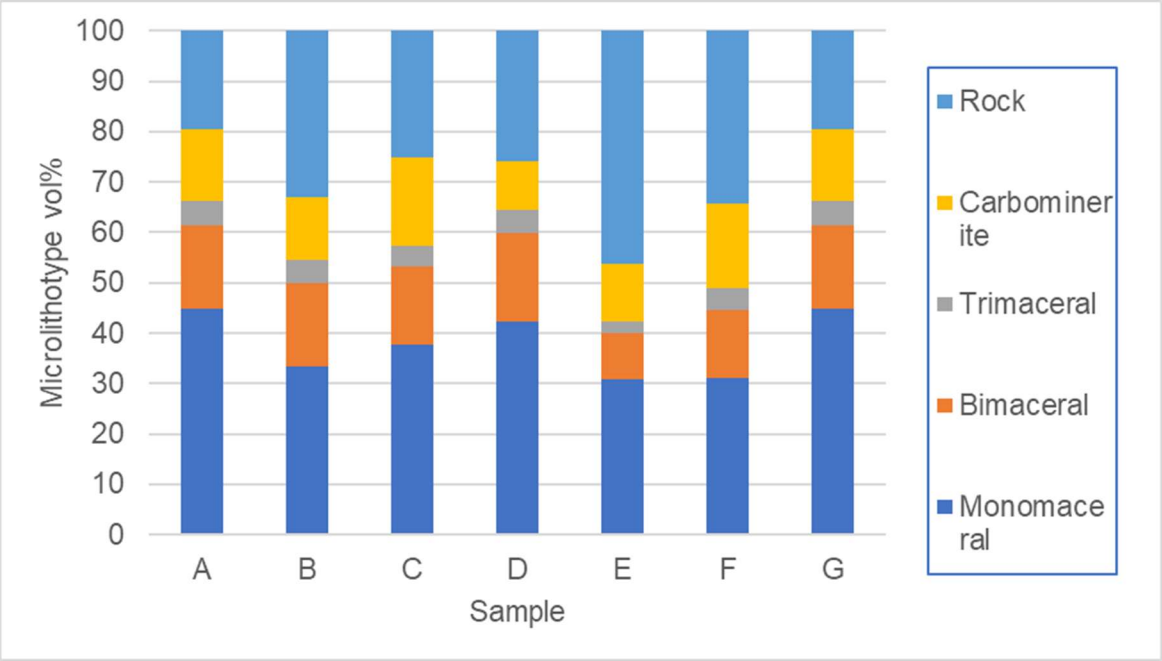

Figure 53: Microlithotype composition (including mineral matter)

Appendix E.2: Maceral composition

The maceral composition of the coal char samples including the mineral matter composition is depicted in Figure 54. From this figure it is easier to compare the maceral content, liptinite, inertinite and vitrinite compositions of the samples. These samples contain only small amounts of liptinite and vitrinite, consisting mainly of inertinite and mineral matter.

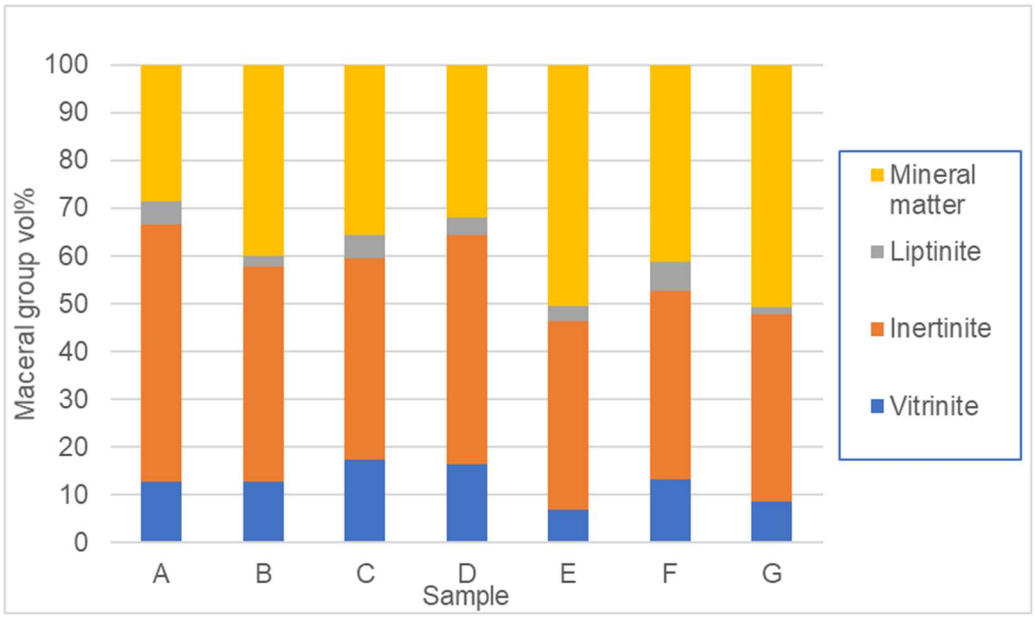

Figure 54: Maceral composition (including mineral matter)

Figure 55 summarizes the maceral composition of the coal samples excluding the mineral matter. This figure confirms the previously established conclusion, that these samples are inertinite rich with small amounts of liptinite and vitrinite.

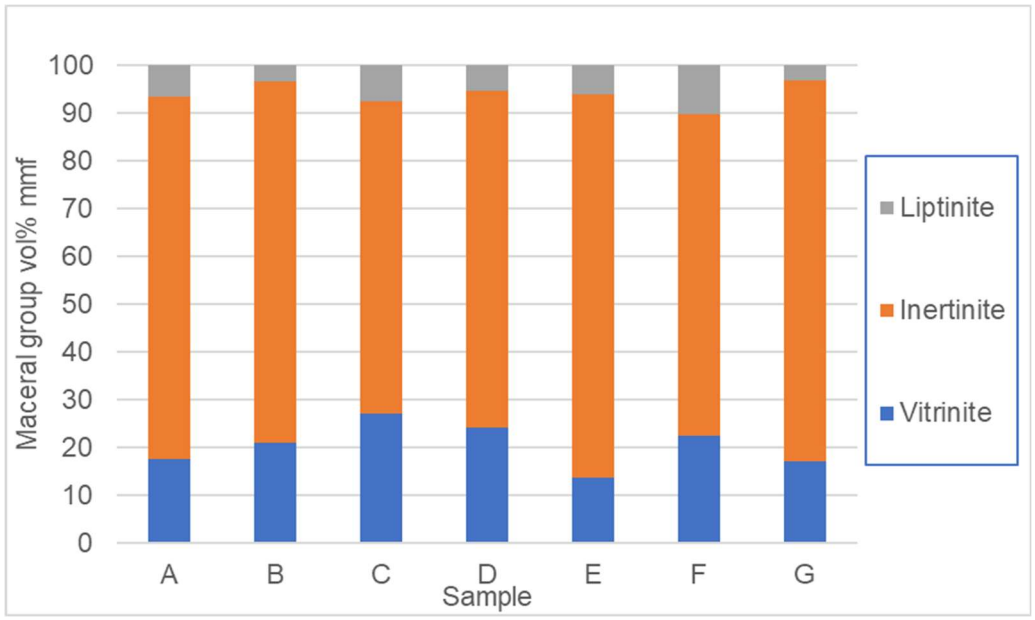

Figure 55: Maceral composition (mmf)

Appendix F: Coal/ char statistical modelling approach.

The methods used for the statistical modelling will be discussed in this section. Starting with the correlation of reactivity and temperature in Section 3.7.1. The reactivities estimated based on the coal and char properties were calculated using the method explained in Section 3.7.2.

Appendix F.1: Correlating reactivity with temperature.

The plot of the predicted reactivity as a function of temperature is depicted in Figure 56 for all the coal char samples used in this study. A statistical model was constructed for reactivity as a function of temperature and the different sources as qualitative variables. The purpose of the model is to quantify the difference in reactivity between the sources, as well as the effect of temperature on reactivity and the interaction between temperature and the different coal sources. Note a significant interaction indicates that the effect of temperature on the reactivity is different for different coal sources. The estimated regression coefficients are shown in Table 40. ISI is used as the reference source, and the values in the first column are the difference in the slope between the specific source and source ISI.

Table 40 was used to produce the predicted trends as shown in Figure 56.

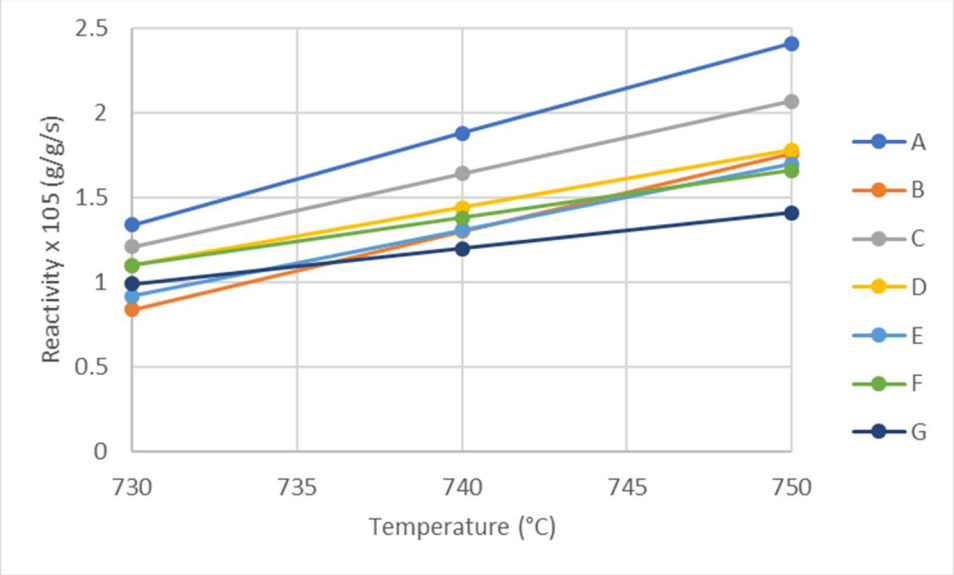

Figure 56: Experimental reactivity plot from 730 to 750 °C

A statistical model was constructed for reactivity as a function of temperature and the different sources as qualitative variables. The purpose of the model is to quantify the difference in reactivity between the sources, as well as the effect of temperature on reactivity and the interaction between temperature and the different coal sources. Note a significant interaction indicates that the effect of temperature on the reactivity is different for different coal sources. The estimated regression coefficients are shown in Table 40. ISI is used as the reference source, and the values in the first column are the difference in the slope between the specific source and source ISI.

Table 40: Estimated coefficients of the temperature and coal sources model.

	Temperature slope	Intercept
Average (Sample F)	0.028	-19.45
Sample G	-0.007	5.227
Sample C	0.014	-10.76
Sample E	0.011	-8.005
Sample B	0.018	-13.45
Sample D	0.005	-3.989
Sample A	0.026	-18.38

Equation (7) was used to determine the reactivities of the coal samples using the estimated coefficients in A statistical model was constructed for reactivity as a function of temperature and the different sources as qualitative variables. The purpose of the model is to quantify the difference in reactivity between the sources, as well as the effect of temperature on reactivity and the interaction between temperature and the different coal sources. Note a significant interaction indicates that the effect of temperature on the reactivity is different for different coal sources. The estimated regression coefficients are shown in Table 40. ISI is used as the reference source, and the values in the first column are the difference in the slope between the specific source and source ISI.

Table 40. The predicted values are obtained as

$$\hat{y} = b_0 + b_{temp}x + \sum_{j=2}^{r} b_j Z_j + \sum_{j=2}^{r} b_{j,temp} Z_j x \quad (7)$$

where b_0, b_{temp}, b_j and $b_{j,temp}$ are the least squares estimates given in A statistical model was constructed for reactivity as a function of temperature and the different sources as qualitative variables. The purpose of the model is to quantify the difference in reactivity between the sources, as well as the effect of temperature on reactivity and the interaction between temperature and the different coal sources. Note a significant interaction indicates that the effect of temperature on the reactivity is different for different coal sources. The estimated regression coefficients are shown in Table 40. ISI is used as the reference source, and the values in the first column are the difference in the slope between the specific source and source ISI.

Table 40. For example, for temperature equal to 730 °C, the reactivity of ISI is calculated as follows;

$$Reactivity_{ISI} = b_0 + b_{temp}x = -19.44 + 0.028x$$

$$= -19.44 + 0.028(730)$$

$$= 1.10 \text{ g/g/s}$$

This means that for every one unit increase in temperature the reactivity increases by 0.028 units. Note the Z_j indicator variables are all zero since ISI is the reference source. For MIM, the reactivity is calculated as follows;

$$Reactivity_{MIM} = -19.44 - 10.76 + 0.028x + 0.01x = -30.20 + 0.032x$$

From the MIM reactivity model, it can be observed that the intercept is adjusted downward by -10.764 reactivity units and the slope is higher by 0.014 reactivity units. Therefore, from the final model, for every one unit increase in temperature the reactivity increases by 0.032 units for MIM. The equations for the other sources can be specified in the same way. The difference in reactivity between the sources at average temperature must be assessed through the Tukey Honest Significant Difference (HSD) tests. The parity plot of the observed versus predicted reactivity is given in Figure 39 Section 5.3. These reactivities are relatively close to the calculated reactivities presented in Table 23. The R^2 values are also determined from the parity plots in Section 5.2. This value is an indication of how well the model predicts the variation in the reactivities.

Table 41 lists the mean differences in reactivity between the coal sources, together with the 95 % confidence intervals and p-values.

Table 41: Tukey Honest Significant differences results

	Difference	Lower	Upper	P Adjusted
G – F	-0.18	-0.53	0.17	0.59
C – F	0.26	-0.09	0.61	0.21
E – F	-0.07	-0.42	0.28	0.99
B – F	-0.08	-0.43	0.27	0.98
D – F	0.06	-0.29	0.41	1.00
A – F	0.49	0.14	0.84	0.00
C – A	0.44	0.09	0.79	0.01
E – G	0.11	-0.24	0.46	0.93
B – G	0.09	-0.26	0.44	0.96
D – G	0.24	-0.11	0.59	0.29
A – G	0.67	0.32	1.02	0.00
E – C	-0.33	-0.68	0.02	0.07
B – C	-0.35	-0.70	0.00	0.05
D – C	-0.20	-0.55	0.15	0.45
A – C	0.23	-0.12	0.58	0.32
B – E	-0.01	-0.36	0.34	1.00
D – E	0.13	-0.22	0.48	0.84
A – E	0.57	0.22	0.92	0.00
D – B	0.14	-0.21	0.49	0.79
A – B	0.58	0.23	0.93	0.00
A – D	0.44	0.09	0.79	0.01

Appendix F.2: Correlating reactivity with coal and char properties.

The reactivities estimated based on the coal and char properties were calculated using the method explained in this section as presented by Equation 7.

$$\hat{y} = b_{temp}x + \sum_{j=1}^{n} b_j P_j \quad (1)$$

where y is the reactivity, x is temperature and P_i is the proportion of the specific property of the coal. The coefficients of the model are estimated by least squares minimization and is displayed in Section 5.2. As an example, the model specified for the proximate analysis is as follows;

$$Reactivity_{Prox} = b_{temp}x + b_{Moist}P_{Moist} + b_{Ash}P_{Ash} + b_{Vol}P_{Vol} + b_{FC}P_{FC}$$

$$= 0.037x - 0.286P_{ash} - 0.180P_{Vol} - 0.544P_{Moist} - 0.254P_{FC}$$

The equations for the other properties can be specified in the same way.

Appendix G: Petrographic analysis.

Below is a summary of the coal and char minerals assessed.

Table 42: Digital photographs of coal and char minerals assessed

Main category	Coal/char type	Description	Image
Coal	Coal	Unaltered coal	Not observed in these samples; all particles clearly showed evidence of conversion
	Devol coal	Particles showing devolatilization change in shade of grey, devolatilization vacuoles	Not observed in these samples; all particles clearly showed evidence of char formation
Char	Cenosphere thin	Thin walled spherical char; highly porous	
	Cenosphere thick	Thick-walled spherical char; highly porous	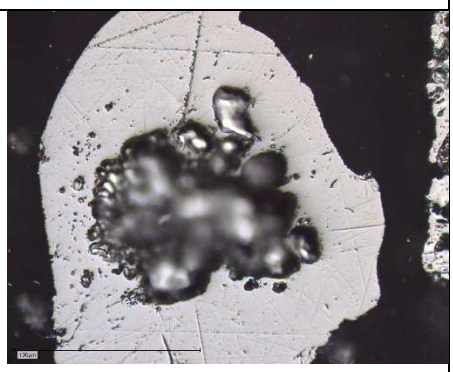
	Honeycomb thin	Thin-walled honeycomb structured char; significant porosity, sub-spherical	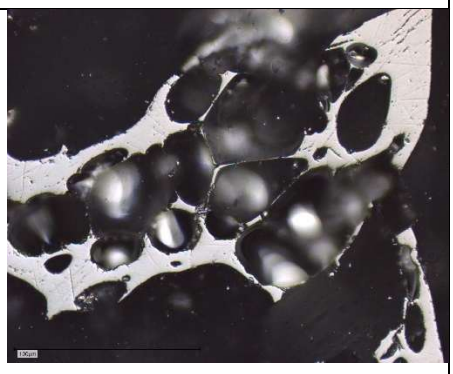
	Honeycomb thick	Thick-walled honeycomb structured char; significant porosity, sub-spherical	

	Mixed porous	Mixture of porous and non-porous sections; porosity must be well developed	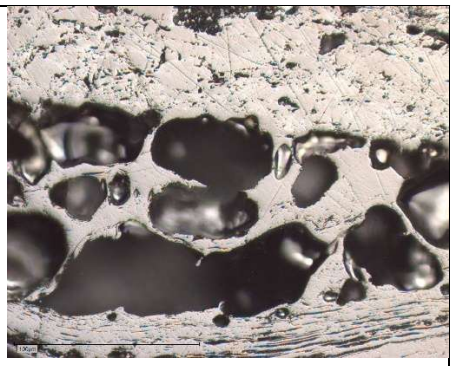
	Mixed dense	Mixture of slight porosity and non-porous sections in particle; must be some evidence of porosity, however minor.	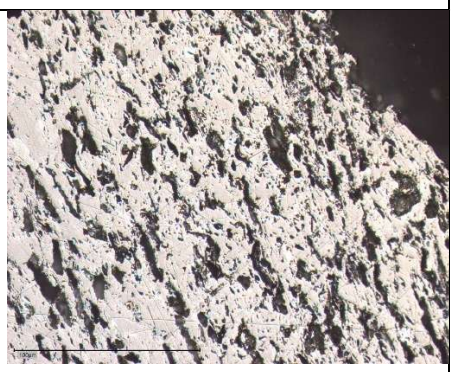
	Inertoid/dense	No evidence of porosity; particle texture represents original maceral; may be any maceral; evidence of conversion is observed in the altered shade	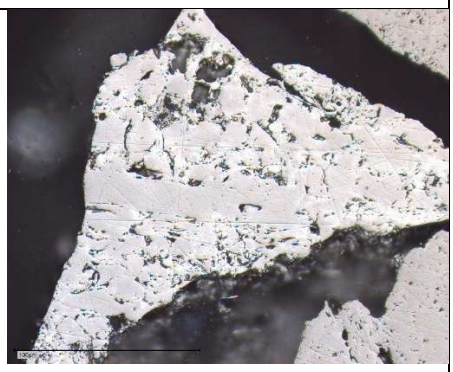
	Fusinoid	No evidence of porosity; particle represents original fusinite	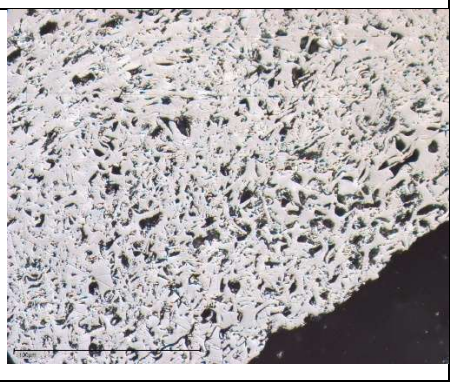

Other	Coked	Particle or area within field of view shows evidence of coke texture	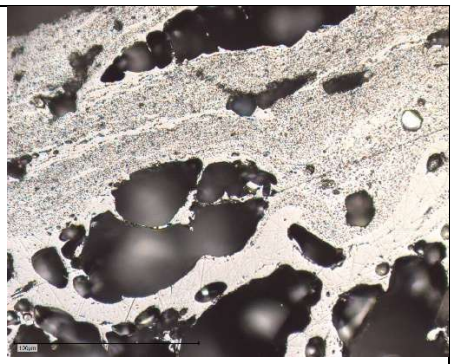
	Oxidized/cracked	Particle or area within shows cracking and or fissuring resulting from exposure to heat; does not include inherent cracks and fissures	
	Consumed	Remnant char walls are observable	Not observed in these samples; temperatures likely to have been too low
Mineral	Carbominerite 20-60	Particle or field of view contains between 20 - 60 vol% mineral matter in intimate association with organic matter	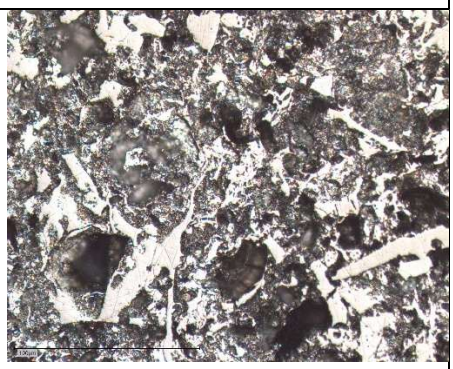
	Unreacted minerals	No signs of alteration in the minerals; mineral appears comparable to that of the feed coal	

	Partially reacted minerals >60%	Minerals showing evidence of reaction	
	Amorphous	Minerals showing no structure, typical of melted minerals	Not observed in these samples; temperatures likely to have been too low
	Neoformed	Newly formed mineral, does not occur in the feed coal	Not observed in these samples; temperatures likely to have been too low

Appendix H: Activation energy calculations

This section will discuss the results of the activation energies determined using the Arrhenius equation as discussed in Section 3.5.4.3. The natural logarithms of the specific reaction rates were plotted at the different temperatures (1/T) as shown in Figure 23. The gradients of the trendlines multiplied by the universal gas constant resulted in the estimated activation energies of the coal char samples. Table 43 shows a summary of the activation energies determined using the Arrhenius plots from Figure 23.

Table 43: Activation energy plot information

Sample	Estimated activation energy E_a (kJ/mol)
A	248
B	307
C	225
D	195
E	273
F	177
G	149

The experimental uncertainty of the activation energies was calculated by using the specific reaction rates together with the uncertainty error. This was done by calculating the activation energy from the lowest possible reaction rate of the sample (r x 10^5 – 0.05 g/g/s) at 730 °C and the highest possible reaction rate (r x 10^5 + 0.05 g/g/s) at 750 °C. A linear plot was then generated between these two data points using the same method as described in Section 3.5.4.3. The lowest possible activation energy was then determined from the highest possible reaction rate of the sample (r x 10^5 + 0.05 g/g/s) at 730 °C and the lowest possible reaction rate (r x 10^5 – 0.05 g/g/s) at 750 °C. Table 44 contains the activation energies calculated from the experimental data together with the high and low values. The difference between the experimental activation energy (E_a) and the low ($E_{a,min}$) and high ($E_{a,max}$) estimated reactivities, resulted in the experimental uncertainties.

Table 44: Activation energy error estimation

Temperature	$E_{a,min}$ (kJ/mol)	E_a (kJ/mol)	$E_{a,max}$ (kJ/mol)	Uncertainty (kJ/mol)
Sample A	223.79	248.05	272.69	± 24.45
Sample B	271.20	306.72	343.54	± 36.17
Sample C	197.48	224.51	252.11	± 27.32
Sample D	165.77	195.44	226.07	± 30.15
Sample E	235.23	272.64	310.16	± 37.47
Sample F	144.68	176.82	209.32	± 32.32
Sample G	112.45	148.55	185.21	± 36.38

Bibliography

[1] S. K. Lee, S., Speight, J.G. & Loyalka, *Handbook of Alternative Fuel Technologies*. CRC Press, 2014. doi: 10.1201/9781420014518.

[2] D. Harris, C. Heidrich, and J. Feuerborn, “Global aspects on coal combustion products.,” *World of Coal Ash (WOCA)*, no. 1, pp. 1–21, 2019.

[3] “World Energy Council,” *World Energy Resources*, 2016.

[4] British Petroleum Company, “67 th edition Contents is one of the most widely respected,” *Statistical Review of World Energy*, pp. 1–56, 2018.

[5] S. Zhao and A. Alexandroff, “Current and future struggles to eliminate coal,” *Energy Policy*, vol. 129, no. February, pp. 511–520, 2019, doi: 10.1016/j.enpol.2019.02.031.

[6] J. G. Speight, *Handbook of Coal Analysis*. John Wiley & Sons, 2005. doi: 10.1002/0471718513.

[7] S. D. Oladipupo, H. Rjoub, D. Kirikkaleli, and T. S. Adebayo, “Impact of Globalization and Renewable Energy Consumption on Environmental Degradation : A Lesson for South Africa,” vol. 11, no. 1, pp. 145–155, 2022, doi: 10.14710/ijred.2022.40452.

[8] O. SEN NAG, “The Top 10 Coal Producers Worldwide,” World Atlas. Accessed: Nov. 09, 2023. [Online]. Available: https://www.worldatlas.com/articles/the-top-10-coal-producers-worldwide.html

[9] M. Barrientos and C. Soria, “Coal Exports by Country,” IndexMundi. Accessed: Nov. 20, 2023. [Online]. Available: https://www.indexmundi.com/energy/?product=coal&graph=exports&display=rank

[10] N. Worship, “The challenges and opportunities of electricity generation on economic growth in South Africa : an ARDL approach The Challenges and Opportunities of Electricity Generation on Economic Growth in South Africa : An ARDL Approach,” 2022, doi: 10.32479/ijeep.12541.This.

[11] “Production volume of coal in South Africa from 1999 to 2022,” Statista. Accessed: Nov. 28, 2023. [Online]. Available: https://www.statista.com/statistics/265463/south-african-coal-production-in-oil-equivalent/#:~:text=South Africa’s coal production amounted,percent from the previous year.

[12] S. M. Gouws, H. W. J. P. Neomagus, D. G. Roberts, J. R. Bunt, and R. C. Everson, “The effect of carbon dioxide partial pressure on the gasification rate and pore development of Highveld coal chars at elevated pressures,” *Fuel Processing Technology*, vol. 179, no. June, pp. 1–9, 2018, doi: 10.1016/j.fuproc.2018.05.027.

[13] A. Kler, P. Zharkov, Y. Potanina, A. Marinchenko, and N. Epishkin, “Environmental and Climate Technologies,” *The Effect of the Carbon Tax Value on the Optimal Parameters and Characteristics of Coal Power Plants*, vol. 23, no. 3, pp. 104–111, 2020.

[14] A. Gravelsins, G. Bazbauers, A. Blumberga, and D. Blumberga, “Power Sector Flexibility through Power-to-Heat and Power-to-Gas Application-System Dynamics Approach,” *Environmental and Climate Technologies*, vol. 23, no. 3, pp. 319–332, 2019, doi: 10.2478/rtuect-2019-0098.

[15] M. Gräbner, “Handbook of Fuels Fischer-Tropsch Re fi ning Chemical Looping Systems for Fossil Energy Conversions Gasi fi cation Processes – Modeling and Simulation Ef fi cient Carbon Capture for Coal Power Plants The Handbook of Clean Coal Utilization 2V Set Energy fo,” 2015.

[16] R. Kurose, M. Ikeda, and H. Makino, “Combustion characteristics of high ash coal in a pulverized coal combustion,” *Fuel*, vol. 80, no. 10, pp. 1447–1455, 2001, doi: 10.1016/S0016-2361(01)00020-5.

[17] R. Iyengar, R. and Haque, “Fuel Processing Technology,” *Gasification of high-ash Indian coals for power generation*, vol. 27, no. 3, pp. 247–262., 1991.

[18] R. C. Everson, H. W. J. P. Neomagus, R. Kaitano, R. Falcon, C. van Alphen, and V. M. du Cann, “Properties of high ash char particles derived from inertinite-rich coal: 1. Chemical, structural and petrographic characteristics,” *Fuel*, vol. 87, no. 13–14, pp. 3082–3090, 2008, doi: 10.1016/j.fuel.2008.03.024.

[19] G. Liu, L. Zheng, L. Gao, H. Zhang, and Z. Peng, “The characterization of coal quality from the Jining coalfield,” *Energy*, vol. 30, no. 10, pp. 1903–1914, 2005, doi: 10.1016/j.energy.2004.09.003.

[20] M. MacDonald, M. Chadwick, and G. Aslanian, *The Environmental Management of Low-Grade Fuels*. 1996.

[21] B. Kavalov and S. Peteves, *The Future of Coal*, vol. 7, no. 5. 2007.

[22] S. Buchanan-Clarke, “Good Governance Africa.,” How committed is SA to reducing fossil fuel dependence? [Online]. Available: https://gga.org/reducing-south-africas-fossil-fuel-dependence/.

[23] H. Ritchie, P. Rosado, and M. Roser, “Energy,” Published online at OurWorldInData.org. Accessed: Apr. 02, 2023. [Online]. Available: https://ourworldindata.org/fossil-fuels

[24] P. McKendry, “Bioresource Technology,” *Energy prodution from biomass (part 1): overview of biomass*, vol. 83, no. 1, pp. 37–46, 2002.

[25] F. F. Adedoyin, A. A. Alola, and F. V. Bekun, “An assessment of environmental sustainability corridor: The role of economic expansion and research and development in EU countries,” *Science of the Total Environment*, vol. 713, p. 136726, 2020, doi: 10.1016/j.scitotenv.2020.136726.

[26] M. Van de Velden, J. Baeyens, A. Brems, B. Janssens, and R. Dewil, “Fundamentals, kinetics and endothermicity of the biomass pyrolysis reaction,” *Renew Energy*, vol. 35, no. 1, pp. 232–242, 2010, doi: 10.1016/j.renene.2009.04.019.

[27] Department of Energy, *The South African Energy Sector Report 2019*. 2019.

[28] Eskom, “Coal power.” [Online]. Available: http://www.eskom.co.za/AboutElectricity/ElectricityTechnologies/Pages/Coal_Power.aspx [Accessed 21 August 2017].

[29] H. H. Lee, J. C. Lee, Y. J. Joo, M. Oh, and C. H. Lee, “Dynamic modeling of Shell entrained flow gasifier in an integrated gasification combined cycle process,” *Appl Energy*, vol. 131, pp. 425–440, 2014, doi: 10.1016/j.apenergy.2014.06.044.

[30] J. R. Bunt and F. B. Waanders, “Identification of the reaction zones occurring in a commercial-scale Sasol-Lurgi FBDB gasifier,” *Fuel*, vol. 87, no. 10–11, pp. 1814–1823, 2008, doi: 10.1016/j.fuel.2007.11.012.

[31] J. Mularski, H. Pawlak-Kruczek, and N. Modlinski, “A review of recent studies of the CFD modelling of coal gasification in entrained flow gasifiers, covering devolatilization, gas-phase reactions, surface reactions, models and kinetics,” *Fuel*, vol. 271, no. March, p. 117620, 2020, doi: 10.1016/j.fuel.2020.117620.

[32] J. Oakey, *Fuel Flexible Energy Generation: Solid, Liquid and Gaseous Fuels*. 2015. doi: 10.1016/C2014-0-01769-8.

[33] D. A. Bell, B. F. Towler, and M. Fan, *Front Matter*. 2011. doi: 10.1016/b978-0-8155-2049-8.10015-4.

[34] J. C. van Dyk, M. J. Keyser, and M. Coertzen, “Syngas production from South African coal sources using Sasol-Lurgi gasifiers,” *Int J Coal Geol*, vol. 65, no. 3–4, pp. 243–253, 2006, doi: 10.1016/j.coal.2005.05.007.

[35] K. Ratshomo, *The South African energy sector report 2021*, vol. 0. 2021.

[36] L. Zhou, G. Zhang, M. Schurz, K. Steffen, and B. Meyer, “Kinetic study on CO2 gasification of brown coal and biomass chars: Reaction order,” *Fuel*, vol. 173, pp. 311–319, 2016, doi: 10.1016/j.fuel.2016.01.042.

[37] G. Liu *et al.*, “Porous structure of bituminous coal chars and its influence on combustion and gasification under chemically controlled conditions,” *Fuel*, vol. 79, no. 6, pp. 617–626, 2000, doi: 10.1016/S0016-2361(99)00185-4.

[38] K. Jayaraman and I. Gokalp, “Effect of char generation method on steam, CO2 and blended mixture gasification of high ash Turkish coals,” *Fuel*, vol. 153, pp. 320–327, 2015, doi: 10.1016/j.fuel.2015.01.065.

[39] S. Kajitani, H. L. Tay, S. Zhang, and C. Z. Li, “Mechanisms and kinetic modelling of steam gasification of brown coal in the presence of volatile-char interactions,” *Fuel*, vol. 103, pp. 7–13, 2013, doi: 10.1016/j.fuel.2011.09.059.

[40] D. G. Roberts and D. J. Harris, “Char gasification with O2, CO2, and H2O: Effects of pressure on intrinsic reaction kinetics,” *Energy and Fuels*, vol. 14, no. 2, pp. 483–489, 2000, doi: 10.1021/ef9901894.

[41] S. Li, X. Chen, A. Liu, L. Wang, and G. Yu, “Co-pyrolysis characteristic of biomass and bituminous coal,” *Bioresour Technol*, vol. 179, pp. 414–420, 2015, doi: 10.1016/j.biortech.2014.12.025.

[42] D. G. Roberts and D. J. Harris, “High-pressure char gasification kinetics: CO inhibition of the C-CO 2 reaction,” *Energy and Fuels*, vol. 26, no. 1, pp. 176–184, 2012, doi: 10.1021/ef201174k.

[43] L. C. Mgano, H. W. J. P. Neomagus, R. C. Everson, and J. R. Bunt, “Evaluation of coal char gasification kinetics and pore development in high pressure steam and carbon dioxide,” no. October, 2020.

[44] S. Kajitani, N. Suzuki, M. Ashizawa, and S. Hara, “CO2 gasification rate analysis of coal char in entrained flow coal gasifier,” *Fuel*, vol. 85, no. 2, pp. 163–169, 2006, doi: 10.1016/j.fuel.2005.07.024.

[45] T. Xu, Y. Wu, and S. Bhattacharya, “Gasification kinetic modelling of Victorian brown coal chars and validity for entrained flow gasification in CO2,” *Int J Min Sci Technol*, vol. 31, no. 3, pp. 473–481, 2021, doi: 10.1016/j.ijmst.2021.03.001.

[46] M. Shahabuddin, M. A. Kibria, and S. Bhattacharya, “Evaluation of high-temperature pyrolysis and CO2 gasification performance of bituminous coal in an entrained flow gasifier,” *Journal of the Energy Institute*, vol. 94, pp. 294–309, 2021, doi: 10.1016/j.joei.2020.09.013.

[47] E. Veca and A. Adrover, “Isothermal kinetics of char-coal gasification with pure CO2,” *Fuel*, vol. 123, pp. 151–157, 2014, doi: 10.1016/j.fuel.2014.01.066.

[48] G. L. D. du Toit, H. W. J. P. Neomagus, R. C. Everson, J. R. Bunt, and L. Koen, “The influence of CO2 on the steam gasification rate of typical South African coal,” *School of Chemical and Minerals Engineering*, vol. Magister S, no. September, p. 129, 2013.

[49] A. D. Engelbrecht, R. C. Everson, and H. W. P. J. Neomagus, “Characterisation and fluidised bed gasification of selected high-ash South African coals,” *School of Chemical and Minerals Engineering*, vol. Master of, no. September, p. 101, 2008.

[50] S. M. Gouws, M. Carrier, J. R. Bunt, and H. W. J. P. Neomagus, “Co-pyrolysis of coal and raw/torrefied biomass: A review on chemistry, kinetics and implementation,” *Renewable and Sustainable Energy Reviews*, vol. 135, no. July 2020, p. 110189, 2021, doi: 10.1016/j.rser.2020.110189.

[51] A. Tremel, T. Haselsteiner, C. Kunze, and H. Spliethoff, “Experimental investigation of high temperature and high pressure coal gasification,” *Appl Energy*, vol. 92, pp. 279–285, 2012, doi: 10.1016/j.apenergy.2011.11.009.

[52] D. G. Roberts and D. J. Harris, “A kinetic analysis of coal char gasification reactions at high pressures,” *Energy and Fuels*, vol. 20, no. 6, pp. 2314–2320, 2006, doi: 10.1021/ef060270o.

[53] H. Chen, H. Yang, F. Ju, J. Wang, and S. Zhang, “The influence of pressure and temperature on coal pyrolysis/gasification,” *Technology (Singap World Sci)*, vol. 7, no. 17, pp. 743–753, 2009, doi: 10.1002/apj.

[54] J. Yan *et al.*, “Kinetic analysis and modeling of coal pyrolysis with model-free methods,” *Fuel*, vol. 241, no. November 2018, pp. 382–391, 2019, doi: 10.1016/j.fuel.2018.12.079.

[55] L. B. Mendez, A. G. Borrego, M. R. Martinez-Tarazona, and R. Mendez, “Influence of petrographic and mineral matter composition of coal particles on their combustion reactivity q,” vol. 82, pp. 1875–1882, 2003, doi: 10.1016/S0016-2361(03)00190-X.

[56] H. Meng, S. Wang, L. Chen, Z. Wu, and J. Zhao, “Thermal behavior and the evolution of char structure during co-pyrolysis of platanus wood blends with different rank coals from northern China,” *Fuel*, vol. 158, pp. 602–611, 2015, doi: 10.1016/j.fuel.2015.06.023.

[57] J. H. Zou *et al.*, “Modeling reaction kinetics of petroleum coke gasification with CO2,” *Chemical Engineering and Processing: Process Intensification*, vol. 46, no. 7, pp. 630–636, 2007, doi: 10.1016/j.cep.2006.08.008.

[58] J. Fermoso, B. Arias, C. Pevida, M. G. Plaza, F. Rubiera, and J. J. Pis, “Kinetic models comparison for steam gasification of different nature fuel chars,” *J Therm Anal Calorim*, vol. 91, no. 3, pp. 779–786, 2008, doi: 10.1007/s10973-007-8623-5.

[59] J. Tanner and S. Bhattacharya, “Kinetics of CO2 and steam gasification of Victorian brown coal chars,” *Chemical Engineering Journal*, vol. 285, pp. 331–340, 2016, doi: 10.1016/j.cej.2015.09.106.

[60] K. B. Kabir, A. Tahmasebi, S. Bhattacharya, and J. Yu, “Intrinsic kinetics of CO2 gasification of a Victorian coal char,” *J Therm Anal Calorim*, vol. 123, no. 2, pp. 1685–1694, 2016, doi: 10.1007/s10973-015-5060-8.

[61] V. Krishnamoorthy, N. Krishnamurthy, and S. V. Pisupati, “Intrinsic gasification kinetics of coal chars generated in a high-pressure, high-temperature flow reactor,” *Chemical Engineering Journal*, vol. 375, no. June, p. 122028, 2019, doi: 10.1016/j.cej.2019.122028.

[62] A. Radenovic, “Pyrolysis of coal,” *Kemija u industriji/Journal of Chemists and Chemical Engineers*, vol. 55, no. 7–8, pp. 311–319, 2006.

[63] S. Porada, G. Czerski, P. Grzywacz, D. Makowska, and T. Dziok, “Comparison of the gasification of coals and their chars with CO2 based on the formation kinetics of gaseous products,” *Thermochim Acta*, vol. 653, no. November 2016, pp. 97–105, 2017, doi: 10.1016/j.tca.2017.04.007.

[64] J. Chen, W. Chen, Y. Jiao, and X. Wang, “Gasification kinetics of bituminous coal char in the mixture of CO 2 , H 2 O, CO, and H 2,” *Energies (Basel)*, vol. 12, no. 3, 2019, doi: 10.3390/en12030496.

[65] D. K. Park, S. D. Kim, S. H. Lee, and J. G. Lee, “Co-pyrolysis characteristics of sawdust and coal blend in TGA and a fixed bed reactor,” *Bioresour Technol*, vol. 101, no. 15, pp. 6151–6156, 2010, doi: 10.1016/j.biortech.2010.02.087.

[66] T. G. Bridgeman and J. M. Jones, “Torrefaction of reed canary grass , wheat straw and willow to enhance solid fuel qualities and combustion properties,” vol. 87, no. 1, pp. 844–856, 2008, doi: 10.1016/j.fuel.2007.05.041.

[67] Y. Song, S. Liu, Q. Wang, L. Xu, and Y. Zhai, “Coke burning behavior of a catalyst of ZSM-5/ZSM-11 co-crystallized zeolite in the alkylation of benzene with FCC off-gas to ethylbenzene,” *Fuel Processing Technology*, vol. 87, no. 4, pp. 297–302, 2006, doi: 10.1016/j.fuproc.2005.05.003.

[68] N. Ellis, M. S. Masnadi, D. G. Roberts, M. A. Kochanek, and A. Y. Ilyushechkin, “Mineral matter interactions during co-pyrolysis of coal and biomass and their impact on intrinsic char co-gasification reactivity,” *Chemical Engineering Journal*, vol. 279, pp. 402–408, 2015, doi: 10.1016/j.cej.2015.05.057.

[69] H. You, W. Long, and Y. Pan, “The mechanism and kinetics for the alkylation of benzene with ethylene,” *Pet Sci Technol*, vol. 24, no. 9, pp. 1079–1088, 2006, doi: 10.1081/LFT-200053893.

[70] Y. Shi, E. Xing, W. Xie, F. Zhang, X. Mu, and X. Shu, “Size-controlled synthesis of MCM-49 zeolites and their application in liquid-phase alkylation of benzene with ethylene,” *RSC Adv*, vol. 5, no. 18, pp. 13420–13429, 2015, doi: 10.1039/c4ra15470c.

[71] P. P. Sripada, T. Xu, M. A. Kibria, and S. Bhattacharya, “Comparison of entrained flow gasification behaviour of Victorian brown coal and biomass,” *Fuel*, vol. 203, pp. 942–953, 2017, doi: 10.1016/j.fuel.2017.04.058.

[72] D. Zeng and T. H. Fletcher, “Effects of pressure on coal pyrolysis and char morphology,” *Energy and Fuels*, vol. 19, no. 5, pp. 1828–1838, 2005, doi: 10.1021/ef0500078.

[73] A. Anca-Couce, “Reaction mechanisms and multi-scale modelling of lignocellulosic biomass pyrolysis,” *Prog Energy Combust Sci*, vol. 53, no. 2016, pp. 41–79, 2016, doi: 10.1016/j.pecs.2015.10.002.

[74] M. An *et al.*, “Study on pyrolysis characteristics of lump coal in the context of underground coal gasification,” *Energy*, vol. 237, p. 121626, 2021, doi: 10.1016/j.energy.2021.121626.

[75] T. H. Christensen, R. Cossu, and R. Stegmann, “Gas Production,” *Landfilling of Waste: Biogas*, pp. 235–315, 2020, doi: 10.1201/9781003062097-4.

[76] J. R. Bunt, “a New Dissection Methodology and Investigation Into Coal Property Transformational Behaviour Impacting on a Commercial-Scale Sasol-Lurgi Mk Iv Fixed-Bed Gasifier,” no. May, 2006.

[77] T. Kabe, A. Ishihara, E. W. Qian, I. P. Sutrisna, and Y. Kabe, *Coal and coal-related compounds: Structures, reactivity and catalytic reactions*, vol. 150, no. October. 2004.

[78] L. D. Smoot and P. J. Smith, “Coal combustion and gasification,” 1985, *Springer Science & Business Media*.

[79] W. F. Hüttinger, K.J. & Merdes, “The carbon-steam reaction at elevated pressure: Formations of product gases and hydrogen inhibitions,” *Carbon N Y*, vol. 30, no. 6, pp. 883–894, 1992.

[80] F. Blackwood, J. & McGrory, “The carbon-steam reaction at high pressure,” *Aust J Chem*, vol. 11, no. 1, pp. 16–33, 1958.

[81] A. Molina and F. Mondragón, “Reactivity of coal gasification with steam and CO 2,” *Fuel*, vol. 77, no. 15, pp. 1831–1839, 1998, doi: 10.1016/S0016-2361(98)00123-9.

[82] G. Alonso, M.J.G., Alvarez, D., Borrego, A.G., Menéndez, R., Marbán, “Systematic effects of coal rank and type on the kinetics of coal pyrolysis,” *Energy and Fuels*, vol. 15, pp. 413–428, 2001.

[83] G. Liu, Q., Hu, H., Zhou, Q., Zhu, S., Chen, “Effect of inorganic matter on reactivity and kinetics of coal pyrolysis,” *Clean Coal Technol*, vol. 83, pp. 713–718, 2004.

[84] C. Zhang, S., Zhu, F., Bai, C., Wen, L., Zou, “hermal behavior and kinetics of thepyrolysis of the coal used in the COREX process,” *J. Anal. Appl. Pyrolysis*, vol. 104, pp. 660–666, 2013.

[85] W. Zhang, L., Hower, J.C., Liu, “Devolatilization and kinetics of maceral con- centrates of bituminous coals,” *Fuel Process Technolegy*, vol. 154, pp. 147–155, 2016.

[86] C. Di Blasi, “Combustion and gasification rates of lignocellulosic chars,” *Prog Energy Combust Sci*, vol. 35, no. 2, pp. 121–140, 2009, doi: 10.1016/j.pecs.2008.08.001.

[87] D. P. Ye, J. B. Agnew, and D. K. Zhang, “Gasification of a South Australian low-rank coal with carbon dioxide and steam: Kinetics and reactivity studies,” *Fuel*, vol. 77, no. 11, pp. 1209–1219, 1998, doi: 10.1016/S0016-2361(98)00014-3.

[88] M. Shadle, L.J., Berry, D.A. & Syamlal, “Coal conversion processes, gasification,” *Kirk-Othmer Encyclopedia of Chemical Technology*, 2002.

[89] Z. Ma *et al.*, “Mineral transformation in char and its effect on coal char gasification reactivity at high temperatures, part 2: Char gasification,” *Energy and Fuels*, vol. 28, no. 3, pp. 1846–1853, 2014, doi: 10.1021/ef402382m.

[90] Q. Sun, W. Li, H. Chen, and B. Li, “The CO2-gasification and kinetics of Shenmu maceral chars with and without catalyst,” *Fuel*, vol. 83, no. 13, pp. 1787–1793, 2004, doi: 10.1016/j.fuel.2004.02.020.

[91] A. F. Koekemoer, “The influence of minerals content and petrographic composition on the gasification of intertiniterich high coal,” *School of Chemical and Minerals Engineering*, vol. Magister i, p. 174, 2009.

[92] B. HATTINGH, *The Determination of the Reaction Mechanisms Involved in the CO2 Gasification of Inertinite-rich, High Ash Coal*. 2010.

[93] L. Zhang, S. Xu, W. Zhao, and S. Liu, “Co-pyrolysis of biomass and coal in a free fall reactor,” *Fuel*, vol. 86, no. 3, pp. 353–359, 2007, doi: 10.1016/j.fuel.2006.07.004.

[94] Y. SAKAWA, M., SAKURAI, Y. & HARA, “Influence of coal characteristics on CO2 gasification,” *Fuel*, vol. 36, pp. 443–452, 1982.

[95] R. C. Everson, H. W. J. P. Neomagus, R. Kaitano, R. Falcon, and V. M. du Cann, “Properties of high ash coal-char particles derived from inertinite-rich coal: II. Gasification kinetics with carbon dioxide,” *Fuel*, vol. 87, no. 15–16, pp. 3403–3408, 2008, doi: 10.1016/j.fuel.2008.05.019.

[96] A. Tremel and H. Spliethoff, “Gasification kinetics during entrained flow gasification - Part II: Intrinsic char reaction rate and surface area development,” *Fuel*, vol. 107, pp. 653–661, 2013, doi: 10.1016/j.fuel.2012.10.053.

[97] Q. Sun, W. Li, H. Chen, and B. Li, “The variation of structural characteristics of macerals during pyrolysis,” *Fuel*, vol. 82, no. 6, pp. 669–676, 2003, doi: 10.1016/S0016-2361(02)00356-3.

[98] M. J. Roberts, R. C. Everson, H. W. J. P. Neomagus, G. N. Okolo, D. Van Niekerk, and J. P. Mathews, “The characterisation of slow-heated inertinite- and vitrinite-rich coals from the South African coalfields,” *Fuel*, vol. 158, pp. 591–601, 2015, doi: 10.1016/j.fuel.2015.06.006.

[99] Y. Zhao, H. Hu, L. Jin, X. He, and B. Wu, “Pyrolysis behavior of vitrinite and inertinite from Chinese Pingshuo coal by TG-MS and in a fixed bed reactor,” *Fuel Processing Technology*, vol. 92, no. 4, pp. 780–786, 2011, doi: 10.1016/j.fuproc.2010.09.005.

[100] Y. Xu *et al.*, “Effects of Vitrinite in Low-Rank Coal on the Structure and Combustion Reactivity of Pyrolysis Chars,” *ACS Omega*, vol. 5, no. 28, pp. 17314–17323, 2020, doi: 10.1021/acsomega.0c01542.

[101] N. J. Wagner, *Geology of Coal*, 2nd ed. Elsevier Inc., 2020. doi: 10.1016/b978-0-12-409548-9.12534-5.

[102] J. B. Milligan, K. M. Thomas, and J. C. Crelling, “Temperature programmedcombustion studies of coal and maceral group concentrates,” vol. 76, no. 13, pp. 1249–1255, 1997.

[103] M. Cloke and E. Lester, “Characterization of coals for combustion using petrographic analysis : a review,” vol. 73, no. 3, pp. 315–320, 1994.

[104] Y. Huang, H. Yamashita, and A. Tomita, “Gasification reactivities of coal macerals,” vol. 29, pp. 75–84, 1991.

[105] C. Avila, T. Wu, and E. Lester, “Petrographic characterization of coals as a tool to detect spontaneous combustion potential,” *FUEL*, vol. 125, pp. 173–182, 2014, doi: 10.1016/j.fuel.2014.01.042.

[106] M. Sakawa, S. Yoshisha, and H. Yukiaki, “Influence of coal characteristics gasif ication on CO2,” pp. 717–720, 1982.

[107] Y. Mao, Y. Jin, K. Li, J. Bi, J. Li, and F. Xin, “Sintering Characteristic in Catalytic Gasification of China Inner Mongolia Bituminous Coal Ash,” *Energy and Fuels*, vol. 30, no. 5, pp. 3975–3985, 2016, doi: 10.1021/acs.energyfuels.6b00514.

[108] S. V. Vassilev, K. Kitano, S. Takeda, and T. Tsurue, “Influence of mineral and chemical composition of coal ashes on their fusibility,” *Fuel Processing Technology*, vol. 45, no. 1, pp. 27–51, 1995, doi: 10.1016/0378-3820(95)00032-3.

[109] S. Wang, X. M. Jiang, X. X. Han, and H. Wang, “Fusion characteristic study on seaweed biomass ash,” *Energy and Fuels*, vol. 22, no. 4, pp. 2229–2235, 2008, doi: 10.1021/ef800128k.

[110] T. Yan, J. Bai, L. Kong, Z. Bai, W. Li, and J. Xu, “Effect of SiO2/Al2O3on fusion behavior of coal ash at high temperature,” *Fuel*, vol. 193, pp. 275–283, 2017, doi: 10.1016/j.fuel.2016.12.073.

[111] B. Wei, X. Wang, H. Tan, L. Zhang, Y. Wang, and Z. Wang, “Effect of silicon–aluminum additives on ash fusion and ash mineral conversion of Xinjiang high-sodium coal,” *Fuel*, vol. 181, pp. 1224–1229, 2016, doi: 10.1016/j.fuel.2016.02.072.

[112] H. Wang, L. Cheng, J. Pu, and J. Zhao, “Melting Characteristics of Coal Ash and Properties of Fly Ash to Understand the Slag Formation in the Shell Gasifier,” *ACS Omega*, vol. 6, no. 24, pp. 16066–16075, 2021, doi: 10.1021/acsomega.1c01949.

[113] B. Liu, Q. He, Z. Jiang, R. Xu, and B. Hu, “Relationship between coal ash composition and ash fusion temperatures,” *Fuel*, vol. 105, pp. 293–300, 2013, doi: 10.1016/j.fuel.2012.06.046.

[114] S. Chakravarty *et al.*, “Composition, mineral matter characteristics and ash fusion behavior of some Indian coals,” *Fuel*, vol. 150, pp. 96–101, 2015, doi: 10.1016/j.fuel.2015.02.015.

[115] J. Li, M. Zhu, Z. Zhang, K. Zhang, G. Shen, and D. Zhang, “Effect of coal blending and ashing temperature on ash sintering and fusion characteristics during combustion of Zhundong lignite,” *Fuel*, vol. 195, pp. 131–142, 2017, doi: 10.1016/j.fuel.2017.01.064.

[116] S. Kajitani, S. Hara, and H. Matsuda, “Gasification rate analysis of coal char with a pressurized drop tube furnace,” *Fuel*, vol. 81, no. 5, pp. 539–546, 2002, doi: 10.1016/S0016-2361(01)00149-1.

[117] P. L. W. Jr, F. R. Jr, and L. G. Austin, “Gas reactions of carbon,” *Advances in Catalysts*, vol. 11, pp. 133–221, 1959.

[118] H. S. Fogler, *Elements of Chemical Reactor Engineering 3rd Edition*, 4 th. Pearson Education Limited, 1999.

[119] J. A. Figueiredo, J.L. & Moulijn, “Carbon and coal gasification: science and technology,” *Springer Science & Business Media*, vol. 105, 2012.

[120] A. D. Engelbrecht, R. C. Everson, and H. W. P. J. Neomagus, “Characterisation and fluidised bed gasification of selected high-ash South African coals,” *School of Chemical and Minerals Engineering*, vol. Master of, no. September, p. 101, 2008.

[121] R. G. Kim, C. W. Hwang, and C. H. Jeon, “Kinetics of coal char gasification with CO2: Impact of internal/external diffusion at high temperature and elevated pressure,” *Appl Energy*, vol. 129, pp. 299–307, 2014, doi: 10.1016/j.apenergy.2014.05.011.

[122] H. Y. PARK and D. H. AHN, “Gasification kinetics of five coal chars with CO2 at elevated pressure,” *Korean Journal of Chemical Engineering*, vol. 24, pp. 24–30, 2007.

[123] D. H. Ahn, B. M. Gibbs, K. H. Ko, and J. J. Kim, “Gasification kinetics of an Indonesian sub-bituminous coal-char with CO2 at elevated pressure,” *Fuel*, vol. 80, no. 11, pp. 1651–1658, 2001, doi: 10.1016/S0016-2361(01)00024-2.

[124] A. Megaritis, Y. Zhuo, R. Messenböck, D. R. Dugwell, and R. Kandiyoti, “Pyrolysis and gasification in a bench-scale high-pressure fluidized-bed reactor,” *Energy and Fuels*, vol. 12, no. 1, pp. 144–151, 1998, doi: 10.1021/ef970115x.

[125] T. F. Wall *et al.*, “The effects of pressure on coal reactions during pulverised coal combustion and gasification,” *Prog Energy Combust Sci*, vol. 28, no. 5, pp. 405–433, 2002, doi: 10.1016/S0360-1285(02)00007-2.

[126] A. Moilanen and H. J. Mühlen, “Characterization of gasification reactivity of peat char in pressurized conditions: Effect of product gas inhibition and inorganic material,” *Fuel*, vol. 75, no. 11, pp. 1279–1285, 1996, doi: 10.1016/0016-2361(96)00105-6.

[127] Y. Wang and D. A. Bell, “Competition between H2O and CO2 during the gasification of Powder River Basin coal,” *Fuel*, vol. 187, pp. 94–102, 2017, doi: 10.1016/j.fuel.2016.08.109.

[128] C. W. Lee, R. G. Jenkins, and H. H. Schobert, “Structure and Reactivity of Char from Elevated Pressure Pyrolysis of Illinois No. 6 Bituminous Coal,” *Energy and Fuels*, vol. 6, no. 1, pp. 40–47, 1992, doi: 10.1021/ef00031a007.

[129] H. Fatehi and X. S. Bai, “Structural evolution of biomass char and its effect on the gasification rate,” *Appl Energy*, vol. 185, pp. 998–1006, 2017, doi: 10.1016/j.apenergy.2015.12.093.

[130] E. Komarova, S. Guhl, and B. Meyer, “Brown coal char CO2-gasification kinetics with respect to the char structure. Part I: Char structure development,” *Fuel*, vol. 152, pp. 38–47, 2015, doi: 10.1016/j.fuel.2015.01.107.

[131] Y. Bai *et al.*, “Gasification of coal char in H2O/CO2 atmospheres: Evolution of surface morphology and pore structure,” *Fuel*, vol. 218, no. November 2017, pp. 236–246, 2018, doi: 10.1016/j.fuel.2017.11.105.

[132] G. Chang, J. Xie, Y. Huang, H. Liu, X. Yin, and C. Wu, “Gasification Reactivity and Pore Structure Development: Effect of Intermittent Addition of Steam on Increasing Reactivity of PKS Biochar with CO2,” *Energy and Fuels*, vol. 31, no. 3, pp. 2887–2895, 2017, doi: 10.1021/acs.energyfuels.6b02859.

[133] J. H. Zou *et al.*, “Modeling reaction kinetics of petroleum coke gasification with CO2,” *Chemical Engineering and Processing: Process Intensification*, vol. 46, no. 7, pp. 630–636, 2007, doi: 10.1016/j.cep.2006.08.008.

[134] S. K. Bhatia and D. Perlmutter, “A random pore model for fluid-solid reactions: I. Isothermal, kinetic control.,” *AIChE Journal*, vol. 26, no. 3, pp. 379–386, 1980.

[135] G. Papole *et al.*, “Dynamic modeling of Shell entrained flow gasifier in an integrated gasification combined cycle process,” *Int J Coal Geol*, vol. 131, no. 2, pp. 1–34, 2007, doi: 10.1016/j.apenergy.2014.06.044.

[136] A. Tremel and H. Spliethoff, “Gasification kinetics during entrained flow gasification - Part II: Intrinsic char reaction rate and surface area development,” *Fuel*, vol. 107, pp. 653–661, 2013, doi: 10.1016/j.fuel.2012.10.053.

[137] A. Tremel, T. Haselsteiner, C. Kunze, and H. Spliethoff, “Experimental investigation of high temperature and high pressure coal gasification,” *Appl Energy*, vol. 92, pp. 279–285, 2012, doi: 10.1016/j.apenergy.2011.11.009.

[138] D. G. Roberts and D. J. Harris, “Char gasification with O2, CO2, and H2O: Effects of pressure on intrinsic reaction kinetics,” *Energy and Fuels*, vol. 14, no. 2, pp. 483–489, 2000, doi: 10.1021/ef9901894.

[139] S. M. Gouws, H. W. J. P. Neomagus, D. G. Roberts, J. R. Bunt, and R. C. Everson, “The effect of carbon dioxide partial pressure on the gasification rate and pore development of Highveld coal chars at elevated pressures,” *Fuel Processing Technology*, vol. 179, no. June, pp. 1–9, 2018, doi: 10.1016/j.fuproc.2018.05.027.

[140] L. C. Mgano, H. W. J. P. Neomagus, R. C. Everson, and J. R. Bunt, “Evaluation of coal char gasification kinetics and pore development in high pressure steam and carbon dioxide,” no. October, 2020.

[141] M. Shadle, L.J., Berry, D.A. & Syamlal, “Coal conversion processes, gasification,” *Kirk-Othmer Encyclopedia of Chemical Technology*, 2002.

[142] L. D. Smoot and P. J. Smith, “Coal combustion and gasification,” 1985, *Springer Science & Business Media*.

[143] T. Adschiri and T. Furusawa, “Relation between CO2-reactivity of coal char and BET surface area,” *Fuel*, vol. 65, no. 7, pp. 927–931, 1986, doi: 10.1016/0016-2361(86)90200-0.

[144] C. R. Ward, “Analysis and significance of mineral matter in coal seams,” *Int J Coal Geol*, vol. 50, no. 1–4, pp. 135–168, 2002, doi: 10.1016/S0166-5162(02)00117-9.

[145] K. Miura, K. Hashimoto, and P. L. Silveston, “Factors affecting the reactivity of coal chars during gasification, and indices representing reactivity,” *Fuel*, vol. 68, no. 11, pp. 1461–1475, 1989, doi: 10.1016/0016-2361(89)90046-X.

[146] T. L. Weissgerber, O. Garcia-Valencia, V. D. Garovic, N. M. Milic, and S. J. Winham, “Why we need to report more than ‘Data were Analyzed by t-tests or ANOVA,’” vol. 7, 2018, doi: 10.7554/eLife.36163.

[147] M. Liu *et al.*, “Char reactivity and kinetics based on the dynamic char structure during gasification by CO2,” *Fuel Processing Technology*, vol. 211, no. June 2020, p. 106583, 2021, doi: 10.1016/j.fuproc.2020.106583.

[148] J. L. Devore and N. R. Farnum, *Probability & Statistics for Engineering and the Siences*, 8th ed. California Polytechnic State Univercity, 2005.

[149] R. L. J. Coetzer, T. S. Joubert, C. L. Viljoen, R. J. J. Nel, and C. A. Strydom, “Response surface models for synthetic jet fuel properties,” *Appl Petrochem Res*, vol. 8, no. 1, pp. 39–53, 2018, doi: 10.1007/s13203-018-0196-7.

[150] A. Nanda, Dr. B. B. Mohapatra, A. P. K. Mahapatra, A. P. K. Mahapatra, and A. P. K. Mahapatra, “Multiple comparison test by Tukey’s honestly significant difference (HSD): Do the confident level control type I error,” *International Journal of Statistics and Applied Mathematics*, vol. 6, no. 1, pp. 59–65, 2021, doi: 10.22271/maths.2021.v6.i1a.636.

[151] H. Braun, “JOHN W . TUKEY ’ S CONTRIBUTIONS TO MULTIPLE COMPARISONS Tel Aviv University and Educational Testing Service 1 . Introduction . The problem of multiplicity or simultaneous inference is concerned with making multiple inferences from a single set of data as,” vol. 30, no. 6, pp. 1576–1594, 2015.

[152] G. G. Koch and S. A. Gansky, “Statistical Considerations for Multiplicity in Confirmatory Protocols,” *Ther Innov Regul Sci*, vol. 30, no. 2, pp. 523–534, 1996, doi: 10.1177/009286159603000228.

[153] A. J. Sankoh, M. F. Huque, and S. D. Dubey, “Some comments on frequently used multiple endpoint adjustment methods in clinical trials,” *Stat Med*, vol. 16, no. 22, pp. 2529–2542, 1997, doi: 10.1002/(SICI)1097-0258(19971130)16:22<2529::AID-SIM692>3.0.CO;2-J.

[154] R. L. J. Coetzer, R. F. Rossouw, and D. K. J. Lin, “Dual response surface optimization with hard-to-control variables for sustainable gasifier performance,” *J R Stat Soc Ser C Appl Stat*, vol. 57, no. 5, pp. 567–587, 2008, doi: 10.1111/j.1467-9876.2008.00631.x.

[155] B. Acharya, I. Sule, and A. Dutta, “A review on advances of torrefaction technologies for biomass processing,” *Biomass Convers Biorefin*, vol. 2, no. 4, pp. 349–369, 2012, doi: 10.1007/s13399-012-0058-y.

[156] G. Lu *et al.*, “Changes in active sites and reactivity induced by interactions among Ca, Si and Al during coal char gasification,” *Fuel*, vol. 310, no. PB, p. 122322, 2022, doi: 10.1016/j.fuel.2021.122322.

[157] A. Henning, H. W. J. P. Neomagus, J. R. Bunt, and R. C. Everson, “Evaluation of the gasification reactivity of Highveld coals for application in the coal to liquids process,” 2016.

[158] Q. P. Campbell, M. D. Barnardo, and J. R. Bunt, “Moisture adsorption and desorption characteristics of some South African coals,” *J South Afr Inst Min Metall*, vol. 113, no. 11, pp. 803–807, 2013.

[159] R. Mobley, “Plant Engineer’s Handbook.pdf,” 2001.

[160] L. D. Mafu, H. W. J. P. Neomagus, R. C. Everson, G. N. Okolo, C. A. Strydom, and J. R. Bunt, “The carbon dioxide gasification characteristics of biomass char samples and their effect on coal gasification reactivity during co-gasification,” *Bioresour Technol*, vol. 258, pp. 70–78, 2018, doi: 10.1016/j.biortech.2017.12.053.

[161] L. SHENGYU, “The Fate of Organic Oxygen During Coal Pyrolysis,” *Energy Sources*, vol. 25, no. 5, pp. 479–488, 2003, doi: 10.1080/00908310390142479.

[162] J. Ochoa, M. C. Cassanello, P. R. Bonelli, and A. L. Cukierman, “CO2 gasification of Argentinean coal chars: A kinetic characterization,” *Fuel Processing Technology*, vol. 74, no. 3, pp. 161–176, 2001, doi: 10.1016/S0378-3820(01)00235-1.

[163] L. Zhang, J. Huang, Y. Fang, and Y. Wang, “Gasification reactivity and kinetics of typical Chinese anthracite chars with steam and CO2,” *Energy and Fuels*, vol. 20, no. 3, pp. 1201–1210, 2006, doi: 10.1021/ef050343o.

[164] C. Liu, Y. Bai, L. Yan, Y. Zuo, Y. Wang, and F. Li, “Impact of alkaline oxide on coal ash fusion temperature,” *International Journal of Oil, Gas and Coal Technology*, vol. 8, no. 1, pp. 79–92, 2014, doi: 10.1504/IJOGCT.2014.064427.

[165] J. C. van Dyk, M. J. Keyser, and M. Coertzen, “Syngas production from South African coal sources using Sasol-Lurgi gasifiers,” *Int J Coal Geol*, vol. 65, no. 3–4, pp. 243–253, 2006, doi: 10.1016/j.coal.2005.05.007.

[166] H. Wang, L. Cheng, J. Pu, and J. Zhao, “Melting Characteristics of Coal Ash and Properties of Fly Ash to Understand the Slag Formation in the Shell Gasifier,” *ACS Omega*, vol. 6, no. 24, pp. 16066–16075, 2021, doi: 10.1021/acsomega.1c01949.

[167] R. H. Matjie, Z. Li, C. R. Ward, J. R. Bunt, and C. A. Strydom, “Determination of mineral matter and elemental composition of individual macerals in coals from Highveld mines,” *J South Afr Inst Min Metall*, vol. 116, no. 2, pp. 169–180, 2016, doi: 10.17159/2411-9717/2016/v116n2a8.

[168] C. R. Ward, “Analysis and significance of mineral matter in coal seams,” *Int J Coal Geol*, vol. 50, no. 1–4, pp. 135–168, 2002, doi: 10.1016/S0166-5162(02)00117-9.

[169] S. K. Falcone, H. H. Schobert, D. K. Rindt, and S. Braun, “Fuel Chemistry,” *Mineral transformations during ashing and slagging of selected low-rank coals.*, vol. 29, pp. 41–46, 1984.

[170] F. Yang, Y. Lai, and Y. Song, “Determination of the influence of pyrite on coal spontaneous combustion by thermodynamics analysis,” *Process Safety and Environmental Protection*, vol. 129, pp. 163–167, 2019, doi: 10.1016/j.psep.2019.06.023.

[171] W. Sujanti and D. K. Zhang, “Laboratory study of spontaneous combustion of coal: the influence of inorganic matter and reactor size,” *Fuel*, vol. 78, no. 5, pp. 549–556, 1999, doi: 10.1016/S0016-2361(98)00188-4.

[172] R. E. Mitchell and A. E. J. Akanetuk, “MECHANISMS OF PYRITE OXIDATION TO NON-Submitted by Mechanical Engineering Department Stanford University,” no. September, pp. 1–35, 2002.

[173] R. A. Creelman, C. R. Ward, G. Schumacher, and L. Juniper, “Relation between coal mineral matter and deposit mineralogy in pulverized fuel furnaces,” *Energy and Fuels*, vol. 27, no. 10, pp. 5714–5724, 2013, doi: 10.1021/ef400636q.

[174] X. Qi, G. Song, W. Song, and S. Yang, “Effect of bed materials on slagging and fouling during Zhundong coal gasification,” *Energy Exploration and Exploitation*, vol. 35, no. 5, pp. 558–578, Sep. 2017, doi: 10.1177/0144598717700082.

[175] R. Everson *et al.*, “Detailed characterization of South African high mineral matter inertinite-rich coals and density fractions and effect on reaction rates with carbon dioxide : Macerals , microlithotypes , carbominerites and minerals .,” *S Afr J Chem Eng*, vol. 18, no. 1, pp. 1–16, 2005.

[176] M. Cloke and E. Lester, “Characterization of coals for combustion using petrographic analysis : a review,” vol. 73, no. 3, pp. 315–320, 1994.

[177] A. G. Borrego, D. Alvarez, and R. Menéndez, “Effects of Inertinite Content in Coal on Char Structure and Combustion,” 1997.

[178] G. L. D. du Toit, H. W. J. P. Neomagus, R. C. Everson, J. R. Bunt, and L. Koen, “The influence of CO2 on the steam gasification rate of typical South African coal,” *School of Chemical and Minerals Engineering*, vol. Magister S, no. September, p. 129, 2013.

[179] R. Everson *et al.*, “Detailed characterization of South African high mineral matter inertinite-rich coals and density fractions and effect on reaction rates with carbon dioxide : Macerals , microlithotypes , carbominerites and minerals .,” *S Afr J Chem Eng*, vol. 18, no. 1, pp. 1–16, 2005.

[180] S. V. Vassilev, R. Menendez, M. Diaz-Somoano, and M. R. Martinez-Tarazona, “Phase-mineral and chemical composition of coal fly ashes as a basis for their multicomponent utilization. 2. Characterization of ceramic cenosphere and salt concentrates,” *Fuel*, vol. 83, no. 4–5, pp. 585–603, 2004, doi: 10.1016/j.fuel.2003.10.003.

[181] S. V. Vassilev, R. Menendez, M. Diaz-Somoano, and M. R. Martinez-Tarazona, “Phase-mineral and chemical composition of coal fly ashes as a basis for their multicomponent utilization. 2. Characterization of ceramic cenosphere and salt concentrates,” *Fuel*, vol. 83, no. 4–5, pp. 585–603, 2004, doi: 10.1016/j.fuel.2003.10.003.

[182] P. S. Marathe, R. J. M. Westerhof, and S. R. A. Kersten, “Fast pyrolysis of lignins with different molecular weight: Experiments and modelling,” *Appl Energy*, vol. 236, no. September 2018, pp. 1125–1137, 2019, doi: 10.1016/j.apenergy.2018.12.058.

[183] S. H. Ng, D. P. C. Fung, and S. D. Kim, “Some physical properties of Canadian coals and their effects on coal reactivity,” *Fuel*, vol. 63, no. 11, pp. 1564–1569, 1984, doi: 10.1016/0016-2361(84)90228-X.

[184] R. Zhang, Q. H. Wang, Z. Y. Luo, M. X. Fang, and K. F. Cen, “Energy & Fuels,” *Coal char gasification in the mixture of H2O, CO2, H2, and CO under pressured conditions*, vol. 28, pp. 832–839, 2014.

[185] A. Megaritis, Y. Zhuo, R. Messenbock, D. R. Dugwell, and R. Kandiyoti, “Pyrolysis and gasification in a bench-scale high-pressure fluidized-bed reactor,” *Energy and Fuels*, vol. 12, no. 1, pp. 40–48, 2008, doi: 10.1021/ef970115x.

[186] Y. T. Kim, D. K. Seo, and J. Hwang, “Study of the effect of coal type and particle size on char-CO2 gasification via gas analysis,” *Energy and Fuels*, vol. 25, no. 11, pp. 5044–5054, 2011, doi: 10.1021/ef200745x.

[187] M. D. Casal, M. F. Vega, E. Diaz-Faes, and C. Barriocanal, “The influence of chemical structure on the kinetics of coal pyrolysis,” *Int J Coal Geol*, vol. 195, no. June, pp. 415–422, 2018, doi: 10.1016/j.coal.2018.06.014.

[188] R. C. Messenböck, N. P. Paterson, D. R. Dugwell, and R. Kandiyoti, “Factors governing reactivity in low temperature coal gasification. Part 1. An attempt to correlate results from a suite of coals with experiments on maceral concentrates,” *Fuel*, vol. 79, no. 2, pp. 109–121, 2000, doi: 10.1016/S0016-2361(99)00145-3.

[189] J. Li, M. Zhu, Z. Zhang, and D. Zhang, “A new criterion for determination of coal ash sintering temperature using the pressure-drop technique and the effect of ash mineralogy and geochemistry,” *Fuel*, vol. 179, pp. 71–78, 2016, doi: 10.1016/j.fuel.2016.03.078.

[190] L. Shirazi, E. Jamshidi, and M. R. Ghasemi, “The effect of Si/Al ratio of ZSM-5 zeolite on its morphology, acidity and crystal size,” *Crystal Research and Technology*, vol. 43, no. 12, pp. 1300–1306, 2008, doi: 10.1002/crat.200800149.

[191] S. Y. Renze He, Hui Liu, Qiuxiang Lu, Yanwei Zhao, Xianyang Wang, Xiaoguang Xie, Xiaoling Deng, “Fuel,” *Effects of Si and Al elements in coal on Fe-catalyzed brown coal pyrolysis*, vol. 315, 2022.

[192] C. Dupont *et al.*, “How inorganic elements of biomass influence char steam gasification kinetics,” *Energy*, vol. 109, pp. 430–435, 2016, doi: 10.1016/j.energy.2016.04.094.

[193] G. Skodras and G. P. Sakellaropoulos, “Mineral matter effects in lignite gasification,” vol. 77–78, pp. 151–158, 2002.

[194] E. Hippo and P. L. W. Jr, “Reactivity of heat-treated coals in carbon dioxide at 900 °C,” vol. 54, no. 4, pp. 245–248, 1975.